Structure and Properties of Moiré Interfaces in Two Dimensional Materials

HARVARD UNIVERSITY
Graduate School of Arts and Sciences

DISSERTATION ACCEPTANCE CERTIFICATE

The undersigned, appointed by the

Department of Physics

have examined a dissertation entitled

Structure and Properties of Moiré Interfaces in Two Dimensional Materials

presented by Rebecca Elise Engelke

candidate for the degree of Doctor of Philosophy and hereby certify that it is worthy of acceptance.

Signature Philip Kim

Typed name: Professor Philip Kim, Chair

Signature Julia Mundy

Typed name: Professor Julia Mundy

Signature Ashvin Vishwanath

Typed name: Professor Ashvin Vishwanath

Date: April 25, 2022

Structure and Properties of Moiré Interfaces in Two Dimensional Materials

A DISSERTATION PRESENTED
BY
REBECCA ELISE ENGELKE
TO
THE DEPARTMENT OF PHYSICS

IN PARTIAL FULFILLMENT OF THE REQUIREMENTS
FOR THE DEGREE OF
DOCTOR OF PHILOSOPHY
IN THE SUBJECT OF
PHYSICS

HARVARD UNIVERSITY
CAMBRIDGE, MASSACHUSETTS
APRIL 2022

Thesis advisor: Professor Philip Kim Rebecca Elise Engelke

Structure and Properties of Moiré Interfaces in Two Dimensional Materials

Abstract

The ability to rationally design materials with specific properties is a major motivator in materials science and condensed matter physics. Heterostructures of two dimensional (2D) materials, weakly bonded out of plane via van der Waals forces, offer a versatile platform for creating materials by stacking old materials in new ways. In this thesis, we focus on a facet of that endeavor that has been growing considerably over the past decade: the effect of moiré patterns that form when two lattices are nearly, but not quite, aligned. The van der Waals forces are weak enough that materials are free to sit on each other with incommensurate alignment, due to twist, lattice constant mismatch, or strain. However, the van der Waals forces do serve to create local commensuration, leading to the formation of domains and dislocations at the interface. We use dark field transmission electron microscopy (TEM) to study the resulting structures, and connect to their unique electronic properties.

We investigate the atomic and electronic structure of twisted bilayer graphene near the small and large angle limits of 0° and 30°. We then move beyond twist (seeing how strain produces moiré patterns of its own), beyond graphene (to sublattice-asymmetric materials that can host ferroelectric domains), and finally, beyond bilayer (to twisted trilayer and quadrilayer), getting a view of how extensive the space of moiré-based materials is.

Contents

Author List and Previous Publications

Results presented in Chapter 2 were published in:

> "Atomic and electronic reconstruction at the van der Waals interface in twisted bilayer graphene." Hyobin Yoo, Rebecca Engelke, Stephen Carr, Shiang Fang, Kuan Zhang, Paul Cazeaux, Suk Hyun Sung, Robert Hovden, Adam W. Tsen, Takashi Taniguchi, Kenji Watanabe, Gyu-Chul Yi, Miyoung Kim, Mitchell Luskin, Ellad B. Tadmor, Efthimios Kaxiras and Philip Kim. Nature Materials, 18, 448–453. (2019).

The following authors contributed to Chapter 3:

> Yue Luo, Marios Mattheakis, Michele Tamagnone, Stephen Carr, Hyobin Yoo, Ke Wang, Sai Sunku, Dorri Halbertal, Kenji Watanabe, Takashi Taniguchi, Dmitri Basov, Efthimios Kaxiras, Philip Kim and William L. Wilson.

Results presented in Chapter 4 were published in:

> "30°-Twisted Bilayer Graphene Quasicrystals from Chemical Vapor Deposition." Sergio Pezzini, Vaidotas Mišeikis, Giulia Piccinini, Stiven Forti, Simona Pace, Rebecca Engelke, Francesco Rossella, Kenji Watanabe, Takashi Taniguchi, Philip Kim, and Camilla Coletti. Nano Letters. 20, 5, 3313–3319 (2020).
>
> William Weiter also contributed to Chapter 4.

The following authors contributed to Chapter 5:

> Hyobin Yoo, Stephen Carr, Kevin Xu, Paul Cazeaux, Richard Allen, Andres Mier Valdivia, Takashi Taniguchi, Kenji Watanabe, Mitchell Luskin, Efthimios Kaxiras, Minhyong Kim, Jung Hoon Han, Philip Kim

The following authors contributed to Chapter 6:

> Ayoung Yuk, Kahyun Ko, Stephen Carr, Junhyung Kim, Hosuk Heo, Takashi Taniguchi, Kenji Watanabe, Hongkun Park, Efthimios Kaxiras, Philip Kim, Hyobin Yoo

The following authors contributed to Chapter 7:

> Konstantin Davydov, Xi Zhang, Matthew Green, Isabelle Phinney, Ke Wang, Philip Kim

To the Drs. Charles Engelke

Acknowledgments

The best part about these last several years working on my PhD was the people I met in the process. Much of the work presented in this thesis was done highly collaboratively, and I must credit the people whose experiments, analyses, and insights find their way into this thesis. First I must thank my advisor, Philip. Philip has an amazing sense of what makes for good science, both technically and interpersonally, and at every turn is gently guiding us toward success. Thanks for supporting me in taking my work in weird mathy directions.

Secondly I must thank Hyobin, who taught me so much about TEM, and has been a great example of what it looks like to push projects to the point of being something. And also fun to talk to. Much of my work is inextricably linked with Hyobin's work, mixing and matching fabrication, data collection, or analysis of a single experiment. Another person who's work is interwoven in mine is Stephen Carr, who has done so many calculations for us, provided me with bits of code to get me started on computational projects, and contributed invaluably to interpretation and analysis.

There are many other people to acknowledge. Leroy, for the NSOM imaging, brainstorming sessions, and being one of my few in-person collaborators during the isolation of the pandemic. Jules, sorry I nearly only come to your office with bad news. The undergraduates I've worked with: Kevin, Richard, Sabina, Will, who each contributed to the work in this thesis and were a pleasure to work with. Hannah and Crystal, who deal with the confusing stuff we can't figure out. David Niedzwiecki, who first taught me TEM. The members of the Kim Lab, from whom I've learned many lab techniques and enjoyed excellent camaraderie, including Andy, Mehdi, Andres, Isabelle, Zeyu, Zhongying, Andrew, Jonah, Tamar, Ke, Frank, Jing, Katie, Austin, Xiaomeng. My desk neighbor, Artem, for all the discussions, from nontrivial trivialities to scientific insights. Laurel, for chats about science, books, or life, and going on hikes.

Noah, thanks for having lunch with me. Annie, Maya, and Ann for creating home. Sachi–I think our child selves would be intrigued to know that someday we would be defending our PhDs in the same month in the same (ish) city. Max, and my family, for encouraging me when I'm discouraged.

1

Introduction

Two dimensional materials are distinctly different from conventional, three dimensional materials.

For one thing, when electrons are confined to two dimensions, properties scale differently and electron-electron correlations are more significant. [1]

For another, 2D materials are all surface. Techniques that only probe the surface or a cross-

section of 3D materials can fully describe 2D materials, such as diffraction, ARPES, STM, field-effect gating, and more.

And when you stack them, it becomes all interface.

1.1 Lattice and sublattice

Graphene, a structure of pure carbon equivalent to a single atomically-thin layer of graphite, is in many ways the simplest 2D material, yet the particular symmetries of the graphene lattice give rise to rich and unique structural and electronic properties. Graphene and many 2D materials consist of a honeycomb lattice, which has a trigonal Bravais lattice with two basis atoms per unit cell. We can call these basis sites the A and B sites. We can also think of the empty spot in the middle of each hexagonal plaquette as the C site (See Figure 1.1a). The presence of the A and B sublattices of graphene, that are inequivalent but related by various rotational and mirror symmetry operations, produces an analogous pair of symmetric but distinct points in reciprocal space: the K and K′ points.[2] The K and K′ points are the sites of graphene's Dirac cones[3] and are an additional, degenerate degree of freedom in the system, known as valley.

The fact that graphene's low energy band structure consists of Dirac cones can be found using a tight binding Hamiltonian with two components representing the A and B orbitals, and a nearest neighbor hopping energy γ_0:

$$H_m = \begin{pmatrix} 0 & -\gamma_0 f(k) \\ -\gamma_0 f^*(k) & 0 \end{pmatrix} \tag{1.1}$$

where $f(k) = e^{ik_y a/\sqrt{3}} + 2e^{-ik_y a/2\sqrt{3}} \cos(k_x a/2)$ comes from summing over the three nearest-neighbor sites. Bands near the K point are shown in Figure 1.2a.

The A and B sublattices also affect the possible configurations of a bilayer or multilayer stack

of graphene. When placing a second layer on top, we can imagine placing the C site of the second layer over an A site in the first layer, or over a B site. These are two degenerate ground state stacking orders for bilayer graphene, and they are known as AB stacking and BA stacking, (or sometimes AB and AC stacking) referring to which site sits on top of which other, and shown in Figure 1.1(b-c).

Natural bilayer graphene will be found in AB or BA stacking, collectively known as Bernal stacking. The Hamiltonian, with four components representing A and B sites on each of layers 1 and 2, can be written using two copies of the single-layer Hamiltonian and adding interlayer hopping terms, the most significant of which, γ_1, describes hopping between A and B sites that are right on top of each other.[2,4] Including only interlayer term γ_1, the Hamiltonian becomes:

$$H_{bi} = \begin{pmatrix} -U/2 & -\gamma_0 f(k) & 0 & 0 \\ -\gamma_0 f^*(k) & -U/2 & \gamma_1 & 0 \\ 0 & \gamma_1 & U/2 & -\gamma_0 f(k) \\ 0 & 0 & -\gamma_0 f^*(k) & U/2 \end{pmatrix}. \tag{1.2}$$

U represents the energy difference between layers 1 and 2, which can be created by applying a voltage bias to metal gates above and below the graphene. The resulting band structure is parabolic and gapless (when U=0, Fig. 1.2b), but importantly a nonzero U (due to interlayer electric field) opens a gap (Fig. 1.2c). For $U << \gamma_1 = 0.39$eV, the gap is approximately equal to U.

1.2 Lattice and superlattice

Because van der Waals materials are only weakly bonded out-of-plane, they are not constrained by epitaxy, and are free to sit on top of one another with a twist angle, lattice constant mismatch, or strain at the interface. With the ability to tear a single monolayer material in two pieces and rotate one a desired amount before stacking them,[5,6] twist became a particularly powerful degree of free-

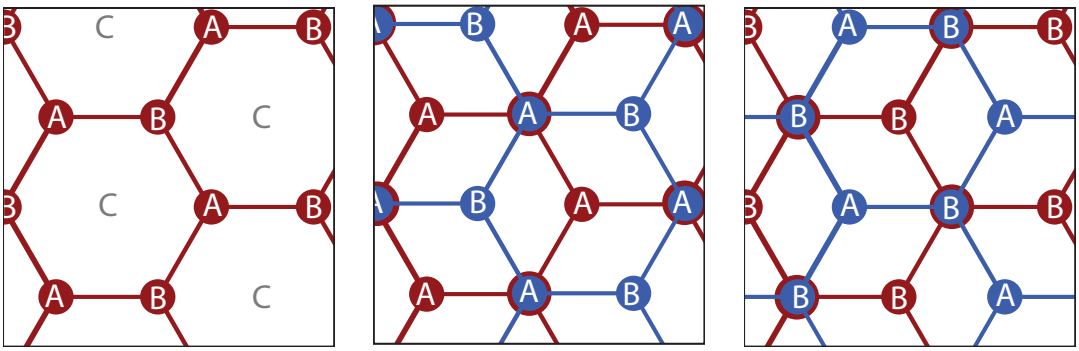

(a) Sublattices of graphene.

(b) AB stacked bilayer

(c) BA stacked bilayer

Figure 1.1: The sublattices of graphene monolayer and bilayer.

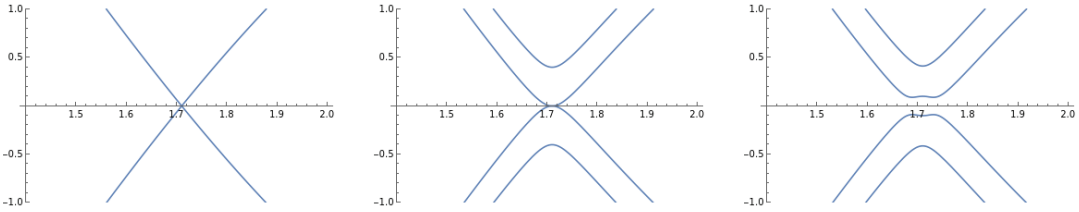

(a) Monolayer band structure near the K point, computed from Equation 1.1

(b) Bilayer band structure near K point, computed from Equation 1.2 with U=0.

(c) Bilayer band structure near K point, computed from Equation 1.2 with U=0.2eV.

Figure 1.2: Low energy band structures of monolayer and bilayer graphene.

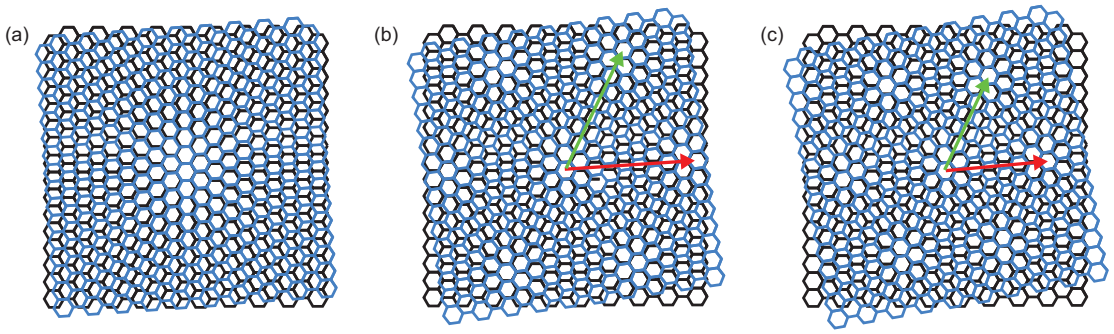

Figure 1.3: As twist angle increases, moiré length decreases. Red and green vector are moiré vectors, $\vec{M}_1$ and $\vec{M}_2$. (a) 4°, (b) 8°, (c) 10°.

dom in designing mesoscopic devices out of 2D materials.

As shown in Figure 1.3, twist angle creates a type of moiré pattern: a 2D periodic beating pattern as the lattices alternate in and out of alignment. The moiré pattern is a clean and tunable way to introduce a nanoscale superlattice into the system. This new periodicity can be used to examine phenomena that require a period hundreds of times larger than an atomic lattice (as in the case of Hoffstadter's butterfly[7,8]), or to modify the band structure of the material by folding into the new mini Brillouin Zone.[9,10,11,12]

The moiré pattern immediately throws a wrench into the normal procedures of solid state physics because the moiré length, in general, is not commensurate with the underlying lattice, making the material no longer periodic, while standard calculations of band structure and other material properties require a periodic unit cell. For any given twist angle, it is always possible to find a twist angle arbitrarily close that has a commensurate unit cell, but the cell might be thousands of atoms long.[13] A computational approach that avoids this problem was developed based on converting the infinite, nonperiodic real space computation into a finite computation over configuration space.[14,15] The configuration space of moiré systems will be discussed more in Chapter 5.

In 2018, widespread interest was attracted to the field of moiré materials when Cao et al demonstrated experimentally that the "magic angle" at which a flat band occurs, was host to correlated elec-

tronic states and superconductivity.[16,17] This proved twist angle control to be capable of producing impactful, exotic behavior out of simple graphene.

1.3 Crystallography

Before we can predict a material's properties, we need to know its structure. Crystal lattices are by nature periodic. Every atom finds itself in a potential well created by all its neighbors, encouraging it to be part of the ordered structure. Putting together two incommensurate lattices creates a competition between them, and the atoms at the interface will deviate from perfect crystallinity. The Frenkel Kontorova model shows how one dimensional crystals react to these competing forces, by locking into commensurate segments, with irregular strained soliton defects in between.[18]

A similar process happens in two dimensions. A twist boundary in a material can reconstruct by relaxing into a network of screw dislocations, with commensurate domains in between.[19] Such interfacial reconstruction has been reported in the moiré interfaces of van der Waals materials as well.[20,21] Characterizing these dislocations is important to understanding the structure of moiré materials.

1.3.1 Dislocations

Dislocations are a type of topological line defect, characterized by a quantity called the Burgers vector. The Burgers vector is defined as the additional vector needed to close a loop around the dislocation that would have been a closed loop in a defectless lattice[22]. An example is shown in Figure 1.4. When a dislocation line is parallel to its Burgers vector, it is called a screw dislocation, and when perpendicular to its Burgers vector, an edge dislocation. However, the dislocation can be oriented in any arbitrary direction neither perpendicular nor parallel to the Burgers vector (known as a mixed dislocation), and can even meander around, attaining different directions along its length. The

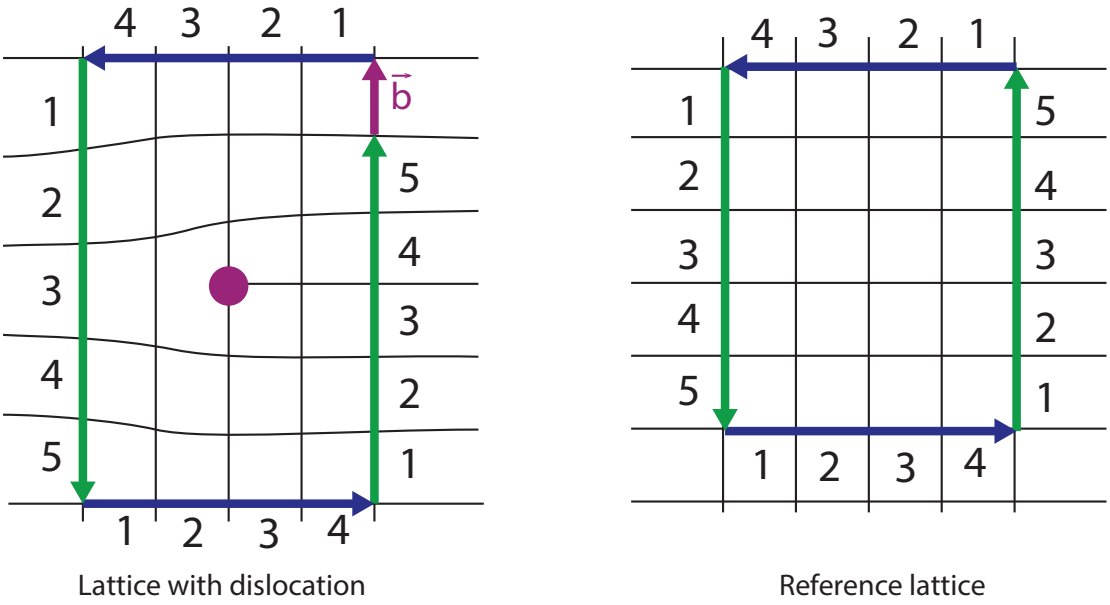

Figure 1.4: A lattice with a dislocation (left) is characterized by a vector offset when traveling the same number of unit cells in each direction that would form a closed loop in a perfect lattice (right). The purple vector $\vec{b}$ that closes the circuit is the Burgers vector. The purple dot is the location of the dislocation (it sticks in/out of the page).

Burgers vector, however, is constant for a single dislocation; thus as the dislocation changes direction, its screw, edge, or mixed nature changes.

Another definition: a dislocation is known as "perfect" if its Burgers vector is a complete lattice vector. In such a case, the crystal structure is the same on both sides of the dislocation. If the Burgers vector is not a lattice vector, it is known as a partial dislocation. In this case, the atomic registry is different on ether side of the dislocation: a stacking fault. In the case of graphene, partial dislocations are significant because the low energy stackings, AB and BA, have different atomic registry and thus a transition between the two consists of a partial dislocation.

1.4 Microscopy

Transmission electron microscopy (TEM) is a powerful tool for characterizing crystal lattices and their defects. A dark field imaging technique based on filtering the diffraction plane can create image contrast between the two types of Bernal stacking or the dislocations between them, thus forming the foundations of our structural studies of moiré materials.

TEM consists of sending a coherent wave of electrons through a lens system made of magnetic fields, and through a sample (the sample must be thin enough to be electron-transparent, in the range of tens of nanometers), to produce a high resolution image (see Figure 1.5). As in any optical system, there exists a back focal plane, in which the Fourier transform (i.e. diffraction pattern) of the image exists, as well as an image plane. The TEM can be used in either mode, with the image or the diffraction pattern projected onto the detector. For a honeycomb lattice, the diffraction pattern looks like a triangular array of spots, as in Figure 1.6.

Each diffracted beam in the TEM can be thought of as arising from a particular set of lattice planes in the crystal. In the honeycomb lattice, the innermost ring of diffraction peaks (Miller indices $\{10\bar{1}0\}$), which we will call first order, are the reciprocal of the zigzag edges (red in Figure 1.6), which have spacing $a\sqrt{3}/2 = 0.21$ nm in graphene (lattice constant, $a = 0.246$ nm). The second ring of peaks ($\{11\bar{2}0\}$), or second order, are reciprocal of the armchair edges (blue in Figure 1.6), of spacing $a/2 = 0.12$ nm in graphene. Dark field imaging consists of putting a physical aperture in the diffraction plane (see Fig. 1.5) which lets through only a certain diffraction spot, and then projecting the real space image onto the detector, filtered by that diffraction spot. Dark field imaging based on the different diffraction spots give us different information about the structure. [20,23,24]

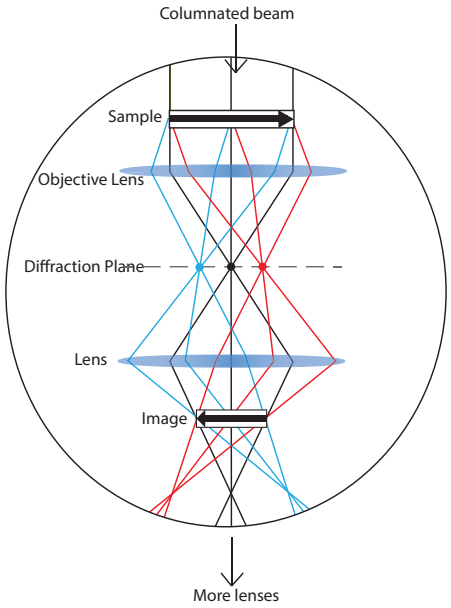

Figure 1.5: Ray diagram of TEM column, with diffraction plane and image plane visible. Each point in the diffraction plane comes from all parts of the real space image, but from the set of beams that are scattered in a particular direction.

1.4.1 Seeing dislocations

Second order dark field can highlight the dislocations that separate AB and BA stacking. Dark field images of the same region from three different second order diffraction spots are shown in Figure 1.7(d-e), with colored outlines indicating the corresponding circled diffraction spot in Fig. 1.7a. Dislocations are regions of strain, hence the lattice spacing is distorted in their vicinity, and dislocations show up in the dark field image as a line of reduced intensity. Intuitively, we can think of it as a region that is contributing less to the selected diffraction peak because it doesn't have the exact periodicity that generated that peak. Lattice planes that are parallel to the Burgers vector are unchanged in their spacing, as there is no distortion occurring in that direction. Hence, every dislocation has a diffraction direction for which it is invisible in dark field; there is no change in that periodicity. This is why in Fig. 1.7(d-e), each image includes outlines of only two out of three sides of the triangles visible in Fig. 1.7b. A composite image that includes all the dislocations can be formed, shown in

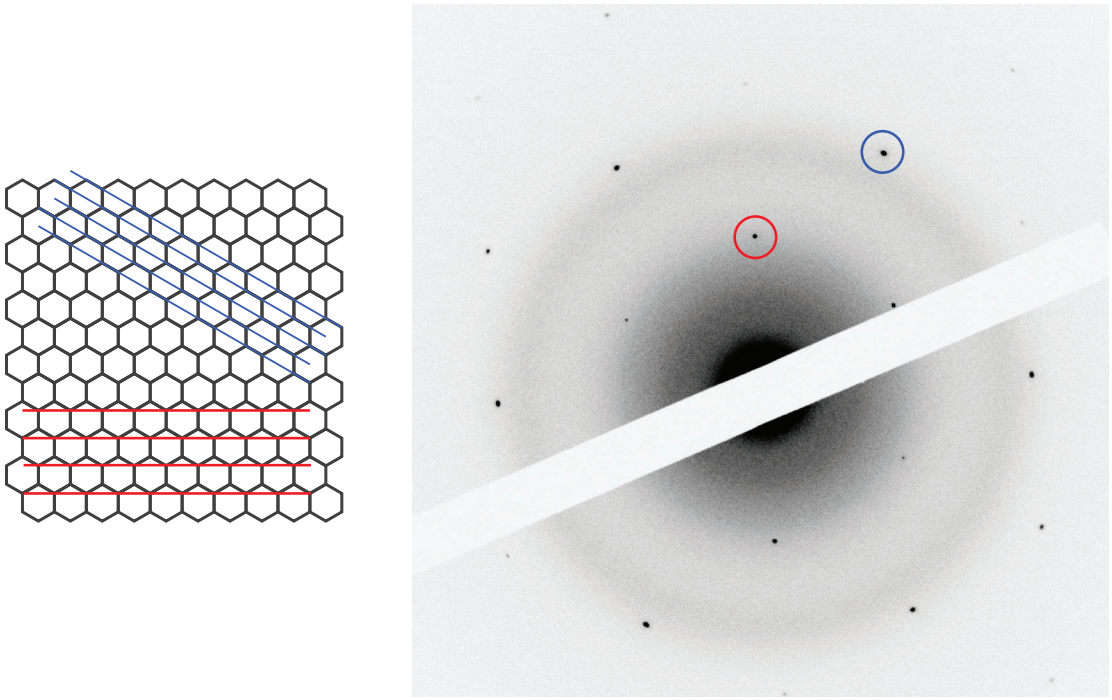

Figure 1.6: Electron diffraction pattern of graphene. Bragg spots corresponding to zigzag (red) and armchair (blue) lattice planes are circled.

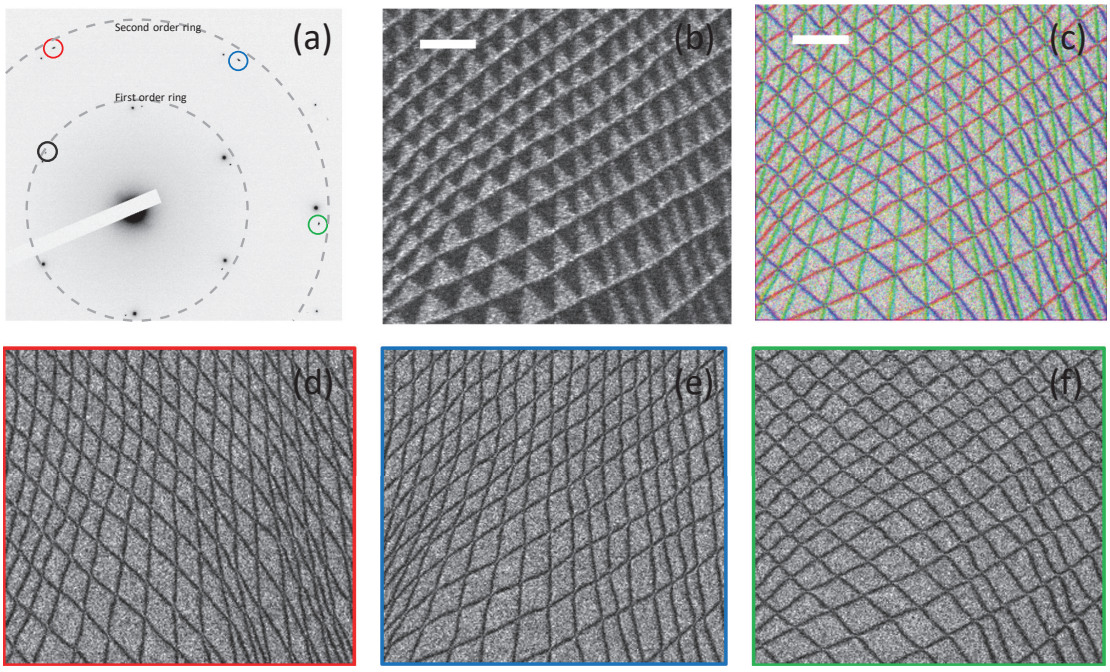

Figure 1.7: Dark field imaging of twisted bilayer graphene. (a) Diffraction pattern, with first and second order rings of diffraction peaks labeled, and diffraction spots used for dark field imaging circled. (b) Dark field image formed using the diffraction spot circled in black in (a), and tilting the sample, shows contrast between AB and BA domains. Scale bar is 100 nm. (c) Composite image from three second order spots shows dislocations that form domain walls. (d) Dark field image formed using red-circled spot in (a). (e) Dark field image formed using blue-circled spot in (a). (f) Dark field image formed using green-circled spot in (a).

Fig. 1.7c, where the color of each line indicates the dark field condition in which those lines were invisible. Knowing the diffraction spot $\vec{g}$ for which a dislocation is invisible in dark field reveals its Burgers vector $\vec{b}$ as the vector that obeys $\vec{b} \cdot \vec{g} = 0$.

For AB - BA transitions, there are three possible orientations of Burgers vectors. They are less than full lattice vectors ($\vec{a_i}$), and consist of $(\vec{a_1} + \vec{a_2})/3$ and its rotations. They are parallel to arm-chair edges, so the Burgers vectors of AB-BA transitions are identified by looking at second order dark field.

1.4.2 Seeing domain contrast

First order dark field can tell us about the stacking order of the layers, for instance whether it is AB or BA. For a flat sample, the image intensity of AB and BA regions are the same. However if the sample is tilted, the symmetry can be broken and image contrast emerge between AB and BA, resulting in an image such as Fig. 1.7b. This can be understood in terms of structure factor. The structure factor is a quantity that tells how the intensity of a diffraction peak varies, when the overall periodicity stays the same but basis atoms are added or moved in the unit cell. For a system with N basis atoms in positions $\vec{d}_j$ relative to the unit cell origin, the structure factor is

$$S(\vec{k}) = \sum_{j=1}^{N} e^{-i\vec{k}\cdot\vec{d}_j}. \tag{1.3}$$

For the bilayer (or multilayer) graphene system, as we tilt the sample, the projected position of the upper layer basis atoms changes with respect to the unit cell, thus changing the structure factor. With a given tilt, AB and BA regions phase shift in opposite ways, and thus contribute different intensities to the dark field image.[25,24]

Dark field imaging is inherently limited in resolution (we throw out a lot of k-space information), but provides important detail about the lattice stacking. Further details about the methods used are included in Appendix A.

Van der Waals moiré materials take the interplay between commensuration and incommensuration, the relationship between lattice symmetries and superlattice symmetries, and some interlayer electronic coupling and combine them to get a rich parameter space of materials with various emergent properties. We will explore this space using TEM to study the structures and connect them to some material properties using electronic transport.

2

Electron diffraction as a probe of supermodulation strength

In the moiré lattice, the competing effects of commensuration (interlayer potential favoring Bernal-type registry) and incommensuration (intralayer strain favoring the material's intrinsic bond lengths and angles) reach a compromise somewhere in between the limits of infinitely sharp dislo-

cations, and pure rigid lattices. To model the properties of twisted bilayer graphene, or to choose a regime in which to do experiments, it is crucial to know the structure of the atomic lattice. In other words, how strong is the reconstruction at any given twist angle.

How do you measure a picometer-scale distortion that varies over tens or hundreds of nanometers? Atomic resolution TEM is not easily applied to either of these scales (although a recent ptychographic technique has been used to image moiré stacking order[26]). We approach this question using electron diffraction, getting a measurement that is sensitive predominantly to the first Fourier component of the lattice distortion.

2.1 Superlattice in diffraction

Under kinematic conditions in TEM, a diffraction pattern is the Fourier transform of the lattice. Hence, we consider the Fourier transform of a relaxed twisted bilayer graphene lattice. Ignoring relaxation, the Fourier transform of a twisted bilayer is simply the superposition of the Fourier transform of two monolayer lattices, with a slight relative rotation (Fig. 2.1). The small vector between equivalent Bragg positions in the two layers is the wavevector of the moiré length. But, if relaxation occurs, how does the diffraction pattern change? We are interested in a feature of the diffraction pattern that can quantify the extent of the structural change.

The effect of relaxation on each layer of the bilayer is a periodic lattice distortion (PLD)[27,28] that is periodic in the moiré length and has three-fold symmetry. It is useful to write the set of atomic positions $\vec{r}$ as their unrelaxed positions $\vec{R}$ plus a modulation that has been decomposed into a Fourier series in the three moiré wavevectors, $\vec{q_1}$, $\vec{q_2}$, and $\vec{q_3}$, that point in 120° angles to each other.

Following Conrad et al,[29] we can write

$$\vec{r} = \vec{R} + \sum_{j=1}^{d} \vec{\eta_j} \sin(\vec{q_j} \cdot \vec{R} + \varphi_j), \tag{2.1}$$

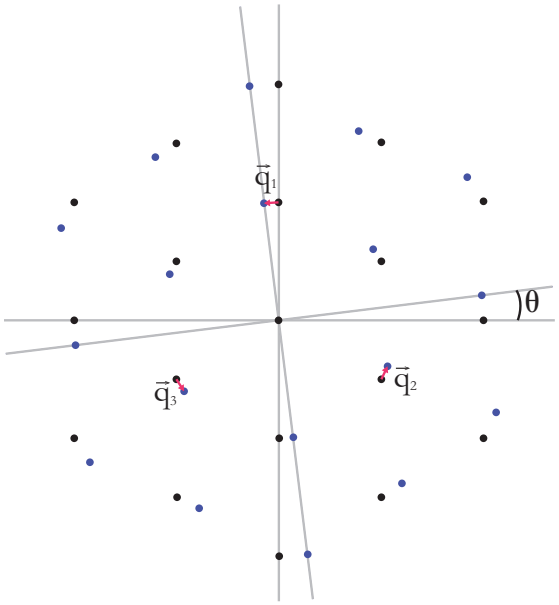

Figure 2.1: Schematic of the diffraction pattern of twisted bilayer graphene with twist angle θ and no lattice relaxation. The vectors $\vec{q_1}, \vec{q_2}, \vec{q_3}$ between Bragg positions are the moiré wavevectors.

where $\vec{\eta_j}$ is a vector corresponding to the amplitude of the $\vec{q_j}$ component, and φ is a possible phase. In the graphene system, $\vec{q_j}$ is going to consist of $\vec{q_1}, \vec{q_2}, \vec{q_3}$ and any combination of sums or differences of those. Hence d could be arbitrarily large as we include higher order components in the expansion. I will assume $\varphi = 0$ but the coefficients produced by nonzero φ can be tracked in the Conrad et al discussion.

Taking the Fourier transform $F[r] = \sum_r e^{i\vec{K}\cdot\vec{r}}$ gives

$$F(\vec{K}) = \sum_R \sum_{p_j=-\infty}^{\infty} e^{i(\vec{K}+\sum_j p_j\vec{q_j})\cdot\vec{R}} \prod_{j=1}^{d} J_{p_j}(\vec{K}\cdot\vec{\eta_j}) \tag{2.2}$$

where J_p is a Bessel function of the first kind. The major conclusion that should be taken from this equation is that, due to the infinite sum over p_j, this quantity turns to zero for every value of $\vec{K}$ except those for which $(\vec{K}+\sum_j p_j\vec{q_j})\cdot\vec{R} = 0$, in other words $\vec{K}+\sum_j p_j\vec{q_j} = \vec{G}$, where $\vec{G}$ is a reciprocal

vector of the original lattice, R. This means that the points in k-space with nonzero intensity are offset from Bragg peaks by sums of the $\vec{q}_j$ vectors. We now have a qualitative picture of what happens in k-space when we allow for relaxation: the Bragg peaks cannot move, but additional ("satellite") peaks offset from the Bragg peaks by the superlattice wavevector can appear.

Suppose we choose to only include $\vec{q}_1$, $\vec{q}_2$, and $\vec{q}_3$ in our decomposition, so $d = 3$. Then, the intensity is related to the product of three Bessel functions, whose indices p_j are the coefficients of the three $\vec{q}_j$. The argument $\vec{K}\cdot\vec{\eta}_j$ of the Bessel functions is going to be less than 1, since the amplitude of the PLD will be less than a lattice constant. So, the larger the index n of the Bessel function, the smaller its value. Sets of p of the form $p = (1, 0, 0)$ will be the largest contributor to the intensity of reciprocal space points of the form $\vec{K} = \vec{G} + \vec{q}_j$, where $j = 1, 2$, or 3, i.e. points that are one moiré wavevector away from the Bragg peak.

If we include higher harmonics in the PLD function, i.e. $\vec{q}$'s with magnitude n times the moiré wavevector, these will contribute primarily to the intensity of points beyond one moiré wavevector away from the Bragg peak. Thus we conclude that by measuring the intensity of the first ring of satellite peaks around each Bragg peak, we are most sensitive to the first Fourier component of the PLD.

2.1.1 Experimental diffraction patterns

We obtained selected area electron diffraction (SAED) patterns for twisted bilayer graphene (TBG) for a range of twist angles from 0.1° to 4°. Figure 2.2 compiles a zoomed-in view on each of the diffraction peaks for each of the first three rings. We refer to the rings as the first order (with hexagonal Miller indices $\{10\bar{1}0\}$), second order ($\{11\bar{2}0\}$), and third order ($\{20\bar{2}0\}$) diffraction, respectively. At each position, we see two Bragg peaks (the brightest two peaks) separated by the twist angle of the material. The Bragg peaks are surrounded by dimmer, satellite peaks that are offset from the Bragg peaks by the three symmetric moiré wavevectors, $\vec{q}_1$, $\vec{q}_2$ and $\vec{q}_3$, as predicted. In Fig. 2.3,

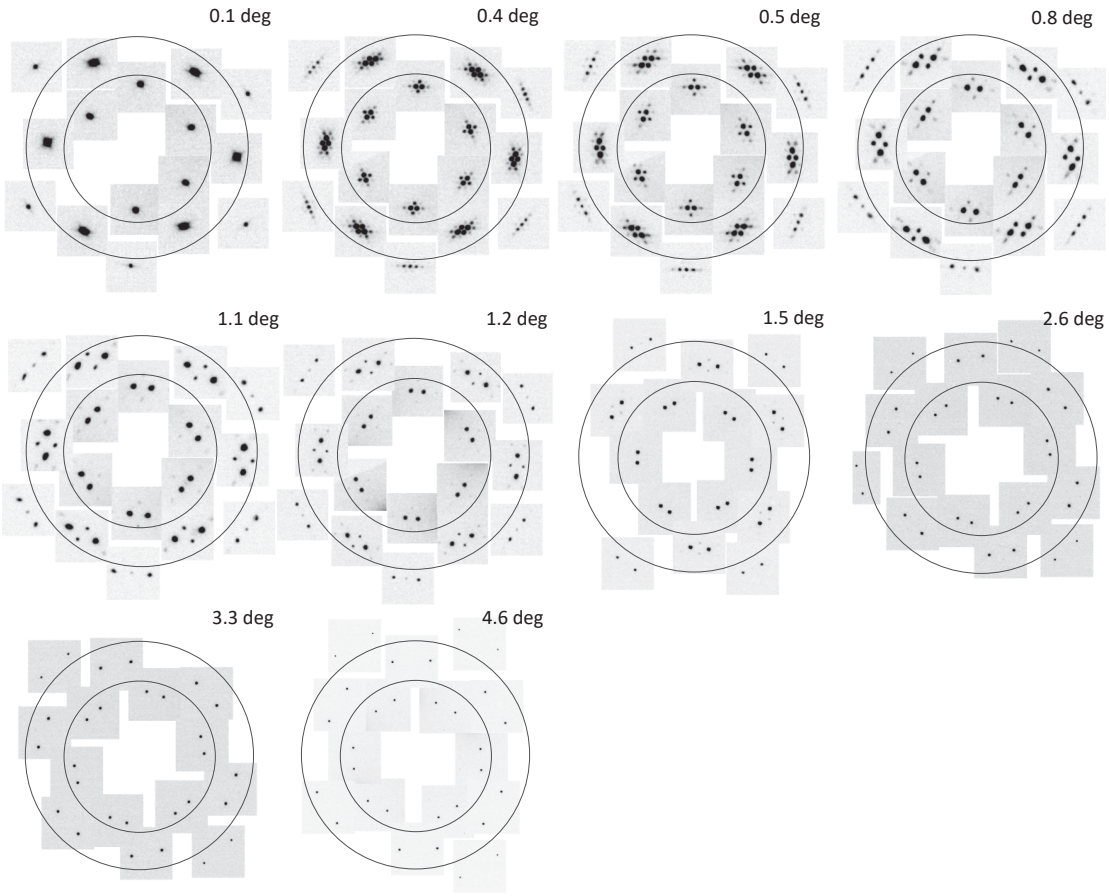

Figure 2.2: Mosaic of SEAD patterns of various twist angles, showing satellite peaks. The region around each Bragg position is scaled to equal size. [Images with angle less than 2° taken by Hyobin Yoo.]

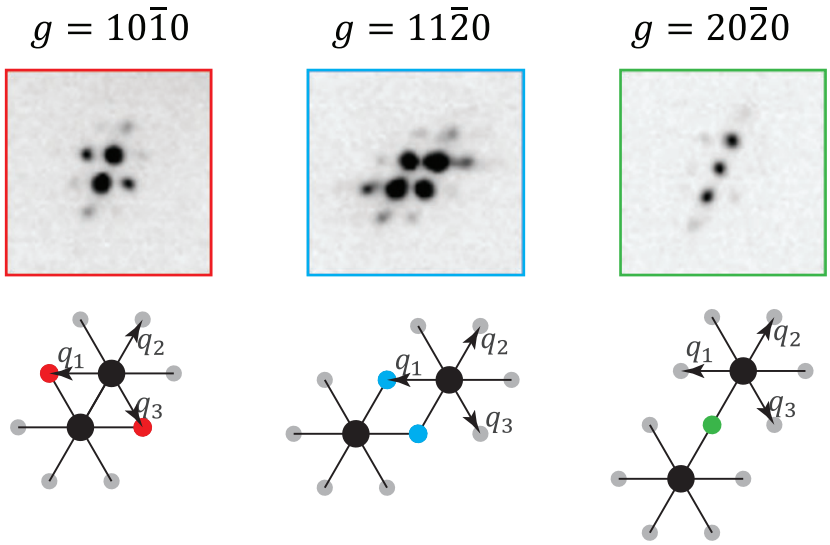

Figure 2.3: Example and schematic of the satellite peak arrangements and vectors between Bragg and satellite peaks, for first, second, and third order.

a representative example and a schematic is shown from each diffraction order, with Bragg peaks in black, satellite peak locations in gray, and the brightest type of satellite peak in color.

2.1.2 Ruling out double scattering

It is important to note that the satellite peaks due to the moiré-induced PLD are at the same $\vec{K}$ positions as multiply-scattered peaks would appear. The assumption that the beam only scatters once, known as kinematic scattering, leads to the result that diffraction peaks can only appear at the sites of the Fourier transform of the lattice. Due to strong interactions with matter, electrons are more likely to undergo multiple scattering than other diffraction probes such as x-rays. Multiple scattering, or dynamic scattering, can be thought of as allowing the beam that has already been scattered off a Bragg plane to scatter again off a different Bragg plane.[30] Thus, new diffraction spots can appear at the sums and differences of kinematical diffraction spots, in other words, offset by the $\vec{q}$ vectors. Multislice modeling was performed to confirm that the intensity of multiply-scattered peaks

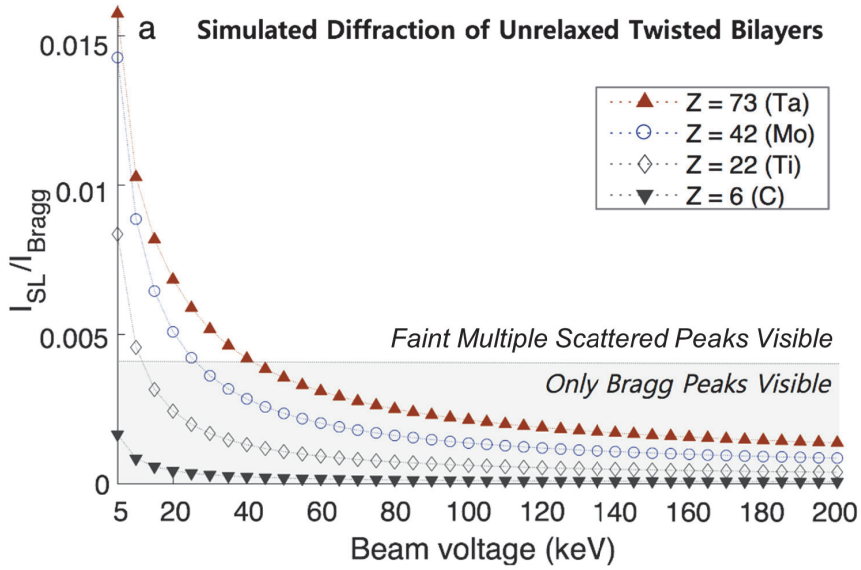

Figure 2.4: Multislice simulation of intensity of multiple-scattered peaks in an unrelaxed twisted bilayer, and dependence on atomic number. [Simulation by Suk Hyun Sung.]

is negligibly small in the graphene bilayer system due to small atomic cross section, shown in Figure 2.4. This confirms that the kinematic approximation is valid in the twisted bilayer graphene system, as would be expected due to the thin system. We conclude it is valid to consider the intensities of the satellite peaks as coming from the PLD and not from multiple scattering.

2.2 Experimental measurement of intensity

We wish to use intensity of satellite peaks to check the consistency between experiment and computed structural models of the relaxed moiré system. Quantitative intensity measurements in diffraction are not always straightforward. There are many factors that cause intensity in an electron diffraction pattern to vary spatially from the intensities of the Fourier transform. The curvature of the Ewald sphere as well as the tilt of the sample cause the detector plane to intersect reciprocal

lattice rods at different points, leading to intensity variation.[30] Thermal fluctuations of atoms cause the diffraction intensity to be attenuated by the Debye-Waller Factor.[31] Rather than account for all influences on intensity, we take the ratio of intensity of each satellite peak (I_{sat}) to its nearest Bragg peak (I_B). This way, we practically remove the effect of intensity changes across K-space, since satellite peaks and their neighboring Bragg peaks are in the same local environment. We also can compare measurements to computations without having to model accurate form factors, and can easily compare intensities across images with different exposure times and doses. Since we assume the measured image intensity to be proportional to the beam intensity, it is also necessary that the dynamic range and linearity of the detector used to collect the image are sufficient.

The diffraction spot as captured in an image is like a 2D Gaussian distribution on top of an approximately constant background. The intensity of a given spot should be the integrated intensity of the distribution above the background, since we essentially want to include all the pixels in the detector that captured signal coming from a given diffracted beam. We can measure this by summing pixel values in a square surrounding the feature, and subtracting a background. The background is computed by the average pixel value of a nearby featureless region of the image, scaled by the number of pixels used. An uncertainty on the background value, due to noise in the image, is computed as the standard deviation of pixel sums from several same-sized background regions.

2.2.1 Measuring angles

To measure the angle between layers, we draw lines on the diffraction image in Digital Micrograph connecting opposite diffraction peaks, and measure the angle between different lines. First, we must accurately locate the endpoints of the line on the diffraction spot. This can be done by eye, or by a script that locates the center of mass of a selection of pixels (based on a script by Dave Mitchell[32]). The second nuance is averaging the angles for the three pairs of opposite peaks. Reciprocal space of a triangle lattice would have three pairs of opposite peaks spaced 60° apart. To find an average

orientation of one layer, we take the angle of the three radial lines from the same layer, modulo 60°, and average the results. (The variance of the single layer values mod 60 can give a sense of the error due to image distortions, typically $\leq 0.3°$.) Then, the orientations of two layers can be subtracted.

2.3 Structure interpretations

Figure 2.5 shows experimentally measured I_{sat}/I_B for the first-, second- and third-order Bragg peaks measured in 11 different samples in the range of $0° < \theta \leq 3.4°$. For $\theta > 3.4°$, I_{sat} is under the experimental detection limit, indicating that no appreciable reconstruction occurs in this large-θ limit. (See Section B.1 for similar data from more satellite peaks.) We find that I_{sat}/I_B decreases rapidly as θ increases, following an empirical relation, $I_{sat}/I_B \sim e^{-\alpha\theta}$ with the constant $\alpha \approx 2.75 \pm 0.3$ (in the unit of inverse degree) obtained from the linear slope presented in Fig. 2.5. We note that α describes how fast the reconstruction strength decreases as θ increases and thus is related to the measure of interlayer interaction of the system, which plays a key role to determine both structural reconstruction and electronic band structure modification. In other twisted materials, such as transition metal dichalcogenides, this relationship will differ.

We study the diffraction peak intensity further to obtain insight into the atomic-scale registry and reconstruction as a function of θ. Although the diffraction peak intensity contains quantitative details of atomic reconstruction (as described in Section 2.1), achieving complete structural information directly from the diffraction pattern is not trivial due to the lost phase information in the SAED. We compare a finite-element method (FEM) model of the structural reconstruction [33] with the experimental observation. Using the atomic coordinates of the reconstructed TBG obtained from the FEM model, the SAED pattern can be computed where I_{sat}/I_B shows a close match with the experimental data exhibiting similar exponential decaying behaviour (open circles in Fig. 2.5). We note that the FEM model exhibits a crossover in structural reconstruction across the character-

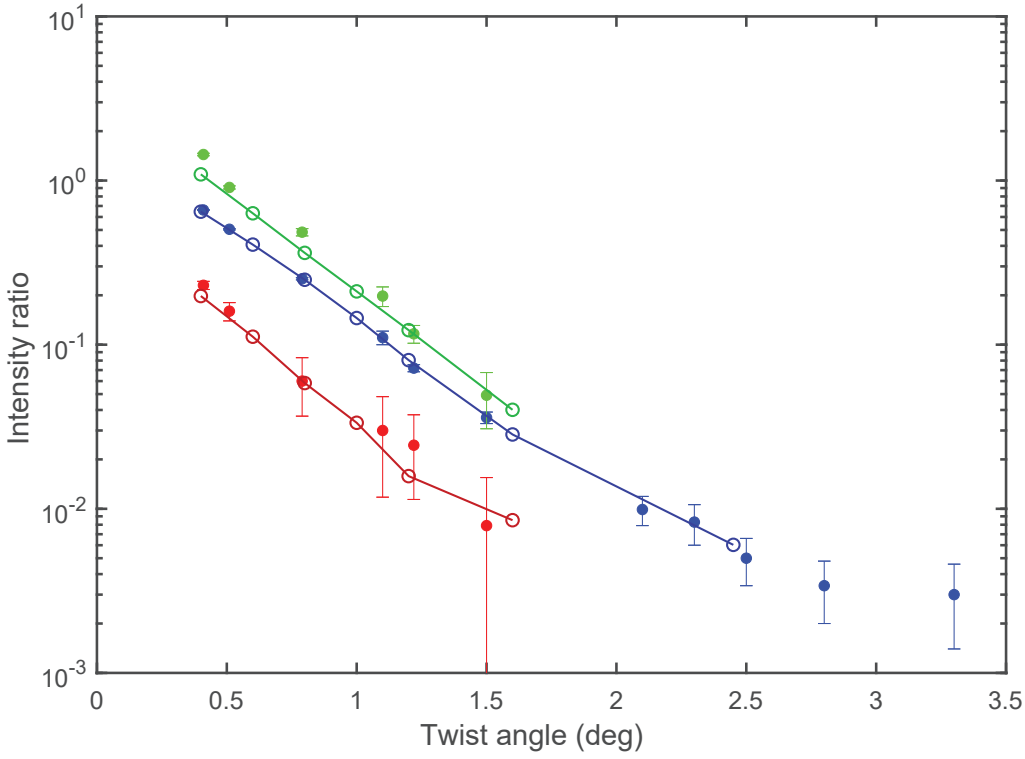

Figure 2.5: Diffraction intensities I_{sat}/I_B vs moiré length, for red, blue, and green satellite peaks as color-coded in Fig. 2.3. Closed circles are experimental measurements, open circles are computed from FEM model in [33].

istic angle, $\theta_c \approx 1°$.[33] For $\theta < \theta_c$, nearly commensurate domains are formed, characterized by an atomic registry close to Bernal stacking and separated by sharp boundaries. The width of the domain boundaries is constant at approximately 10 nm, regardless of the twist angle, in this regime, $\theta < \theta_c$, associated with the formation of solitonic features. For $\theta > \theta_c \approx 1°$, the atomic registry away from the center of the domains starts deviating from Bernal stacking, making the transition from one domain to the other rather gradual. The crossover θ_c occurs when the moiré length scale becomes comparable to the domain boundary width. Above θ_c, the balance between the interlayer energy and the intralayer elastic energy forms domains with reduced commensurability, suppressing the formation of solitons.

2.3.1 Implications for magic angles

We consider how the relaxed structure effects the magic angles. We present the single-particle band structure (Fig. 2.6b) and corresponding density of states (DOS) (Fig. 2.6a, middle and bottom panels) for both unreconstructed and reconstructed configurations in TBG with $\theta = 1.1°$. We note that the reconstructed TBG exhibits sizable gaps of 32 meV and 26 meV for electrons and holes, respectively, which exhibit better agreement with experimentally observed gaps than those from the unreconstructed TBG where no or much smaller gap are shown (Fig. 2.6b). We also note that the overall DOS is reduced in the reconstructed band compared to unreconstructed ones as the bands themselves have larger dispersion. Structural reconstruction occurring at the twist regime above or close to the crossover angle ($\theta \geq \theta_c$) seems to change the details of the band structure such as the single-particle gap size and band dispersion. Nevertheless, the essential physics related to the magic angle (that is, the singular development of the DOS peaks due to the flat band condition) remains qualitatively intact.

At the twist angle regime below the crossover angle ($\theta < \theta_c$), however, the electronic band structure of reconstructed TBG differs significantly from that of unreconstructed TBG. To study the

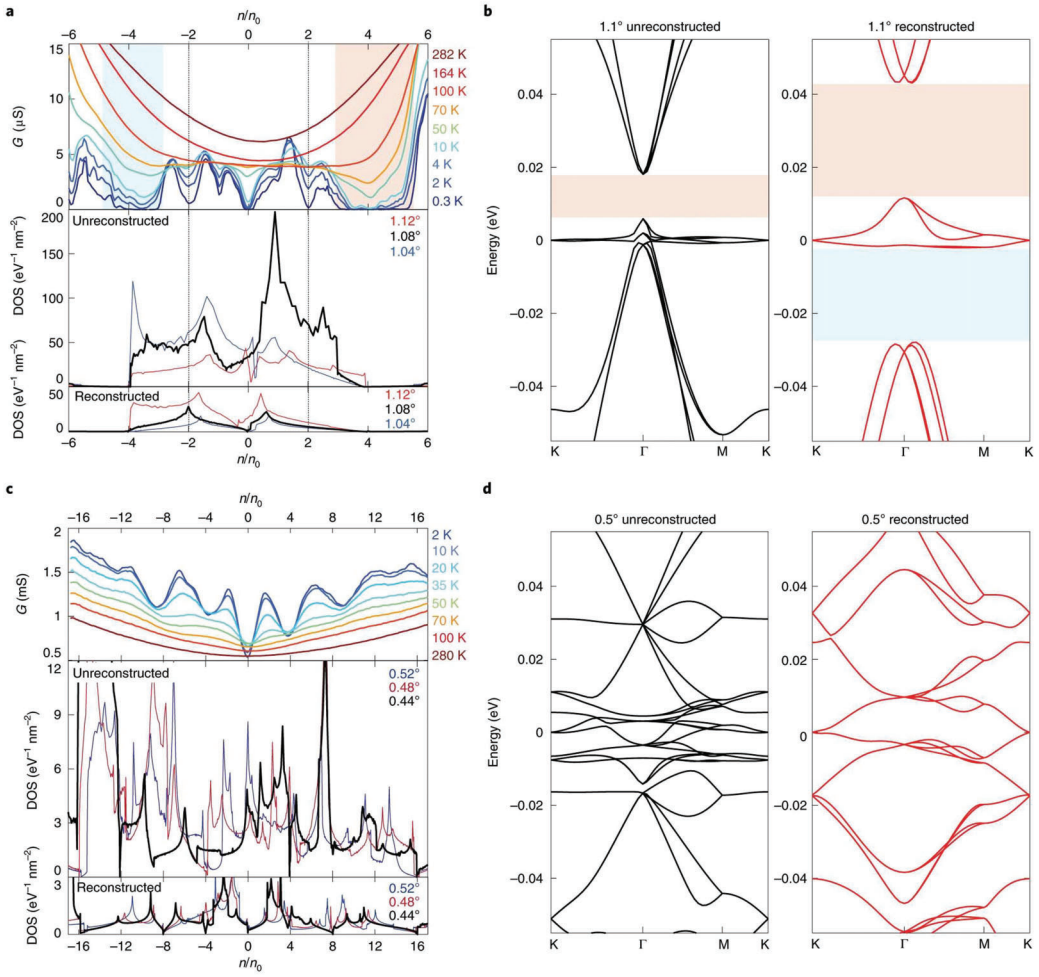

Figure 2.6: (a) Temperature-dependent conductance G measured from a TBG device with θ=1.1° from 0.3K to 282K (top). Calculated DOS without (middle) and with (bottom) reconstruction for three angles near 1.1° in units of density normalized by 1 electron per moiré supercell (n_0). (b) Band structures for the TBG (θ=1.1°) without (left) and with (right) reconstruction. Reconstruction changes the details of the band structure such as single-particle gap size, bandwidth and overall DOS. However, the essential physics of the correlated behaviour stays the same. (c) Temperature-dependent conductance G measured from a TBG device with θ=0.47°from 2K to 280K (top). Calculated DOS without (middle) and with (bottom) reconstruction for three angles near 0.5°. (d) Band structures for TBG (θ=0.5°) without (left) and with (right) reconstruction. Here reconstruction changes the band structures significantly and explains the single-particle features of gate-dependent conductance. [Reprinted from Yoo et al.[34]]

reconstruction effect below the crossover angle regime, we choose a representative twist angle close to the theoretically predicted second magic angle, $\theta \approx 0.5°$. The DOS for the unreconstructued system near 0.5° has many sharp features (Fig. 2.6c, middle) due to the erratic nature of the unreconstructed band structure (Fig. 2.6d, left). Those sharp features are not stable under small changes in twist angle, implying that any experimental measurement of the low-energy transport would be extremely sensitive to the small change in the twist angle. In contrast, the DOS for the reconstructed TBG near 0.5° exhibits sharp features at $n/n_0 = 0, \pm 4$ and ± 8 with their minima close to zero, where n is the electron density and n_0 is the electron density of 1 electron per moiré cell. This behavior corresponds to the Dirac-like band crossing shown in the reconstructed band structure (Fig. 2.6d, right). We note that this observation is generally reproducible with small changes in θ (Fig. 2.6c, bottom) near 0.5°. Experimental observation agrees well with the reconstructed band structure at $\theta \cong 0.5°$. It is clear that the conductance $G(n)$ measured for TBG with $\theta = 0.47°$ shows minima at $n/n_0 = 0, \pm 4$ and ± 8 without gap opening, suggesting the appearance of the secondary Dirac spectrum. It is also noted that the DOS features at $n/n_0 = \pm 4$ are lifted from zero and become less sharp for certain angles. We associate these features with the non-degenerate dispersion near the higher-order Dirac point that is sensitive to the details of how the reconstructed lattice is described in the computation. Moreover, the reconstructed TBG bands exhibit larger dispersion than unreconstructed ones. The more than an order of magnitude suppression in the DOS peaks in this small-θ limit compared to those in the first magic angle near 1.1° suggests that no significant correlated electronic behaviours occur in this regime.

2.3.2 Conclusion

We have used quantitative electron diffraction to experimentally validate models of the relaxed domain structure. We find an angle regime $\theta < 3.4°$, for which reconstruction is observed at all, and a regime $\theta < 1°$ for which domain formation is complete. We determine that relaxation does not

substantially affect the electronic structure at the first magic angle, 1.1°, though it affects details such as the size of the gaps. However, reconstruction is particularly relevant to determining the atomic and electronic structure at the subsequent magic angles, 0.5° and below, and we do not expect to see multiparticle gaps opening in the subsequent magic angles.

3

Towards designer electron transport geometries in the 1D network

In the limit of small angle, a well-formed network of dislocation lines separates AB and BA domains in twisted bilayer graphene. This is an interesting regime because the opposite-sign gap that opens in AB and BA domains under perpendicular electric field leads to topologically protected

modes along the domain boundaries.[35] Topological conduction is a fascinating and pragmatic concept in condensed matter physics, that occurs when a topological invariant, such as Chern number, of an electronic band differs across a boundary, leading to protected edge states along the boundary, that are insensitive to local perturbations.

In the case of bilayer graphene, the Chern number in each valley has opposite sign, so the net Chern number of the band is zero (topologically trivial). However, if intervalley scattering is minimal, electrons can be considered to occupy only one valley, and the valley Chern number differs by 2 across the AB-BA boundary, leading to two modes in each valley along the domain wall (4 total modes). The intervalley scattering length is typically hundreds of nanometers, and is primarily due to disorder at the sample edges.[36] This means it is feasible to observe conduction along the 1D domain walls when the bulk of the graphene is gapped by electric field.

3.1 Bilayers in electric field

We seek evidence of the presence of protected 1D conduction states under application of interlayer electric field. We draw a comparison among three types of bilayer systems: (i) Bernal-stacked bilayer graphene (BLG) ($\theta = 0$), (ii) a large-angle twisted bilayer graphene (TBG) ($\theta \cong 2.8^\circ > \theta_c$) and (iii) small-angle TBG ($\theta = 0.47^\circ < \theta_c$). Figure 3.1 shows $R(D)$, the resistance R_{xx} as a function of displacement field while remaining at charge neutrality, normalized by the resistance R_0 at the global neutrality point ($D = 0$). For $\theta = 0$ (that is, a Bernal-stacked BLG), R/R_0 increases rapidly as $|D|$ increases due to the gap opening. For large-angle TBG ($\theta \cong 2.8^\circ$), however, R/R_0 decreases as $|D|$ increases. The electronic band of this large-angle TBG can be described by two Dirac cones displaced in reciprocal space with negligibly small interlayer coupling.[9,37] Thus, the weakly coupled layers are doped with an equal amount but opposite sign of carriers as $|D|$ increases, making both layers less resistive. In contrast, the electron transport behaviours observed in the small-angle TBG

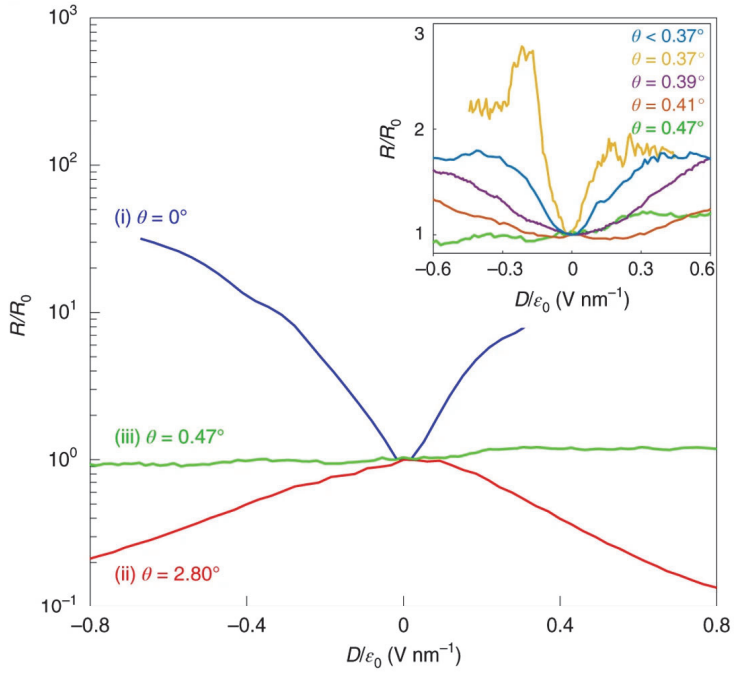

Figure 3.1: Normalized Dirac peak resistances as a function of transverse displacement field obtained from the three devices. The inset shows a linear-scale plot of normalized Dirac peak resistances as a function of the electric displacement field, D, for small-angle TBG devices. [Adapted from [34].]

($\theta = 0.47°$) (iii) are distinctly different from the Bernal-stacked BLG (i) and large-angle TBG (ii) discussed above. In this regime, we expect the displacement field to open a gap in the domains while the domain walls remain conductive. The 1D network can be thought of as a network of simple resistors that each carries quantum resistance $R_q = h/4e^2$. Experimentally, $R(D)$ measured from the small-angle TBG devices ($\theta < \theta_c$) increases and saturates as one applies higher |D| (inset of Fig. 3.1). This observation is consistent with the picture where the current is directed to the 1D network of conducting channels as the AB/BA domains are gapped at higher $|D|$.[38] The saturation values of $R(D)$ are of similar order of magnitude to R_q, as expected from a simple network of R_q assuming incoherent mixing of currents at vertices. These data indicate that in the small angle condition, we can achieve conduction through the 1D network.

3.2 Blind search for network transport

The saturation of Dirac peak resistance implies network transport, but the goal remains to observe unique features of the network, such as the presence of Aharanov-Bohm interference from looping around domains.[39,40] One issue is that in a mesoscopic device, there is angle variation that causes the domains to be different sizes across the device. Perhaps a smaller device is more likely to have uniform domains.

To this end, we consider a device that has two thin strips of twisted bilayer graphene (500 nm and 300 nm wide) crossing multiple thin backgate strips (widths from a few hundred nm to 1 μm). The device is shown in Figure 3.2. By testing out one active gate at a time and fixing the rest at a doped condition ($\sim 2 \times 10^{12}$ cm^{-2} electrons), we can try out different device regions and seek one that seems to have a uniform domain network.

Figure 3.3 shows the Dirac peak resistance vs. displacement field. A saturation behavior is visible at negative displacement field. Dirac peaks coming from the other, fixed backgate regions of the

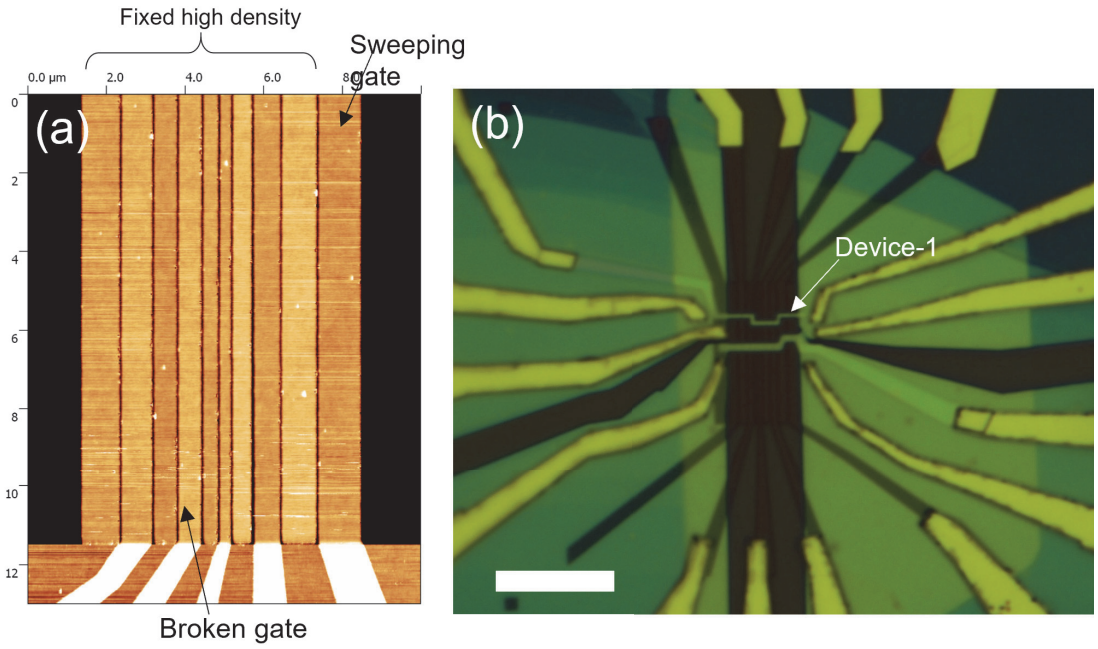

Figure 3.2: Narrow strip twisted bilayer graphene device. (a) Atomic force microscopy image of backgates. (b) Optical image of device. Scale bars are 10 μm. [Fabrication by Ke Wang and Hyobin Yoo.]

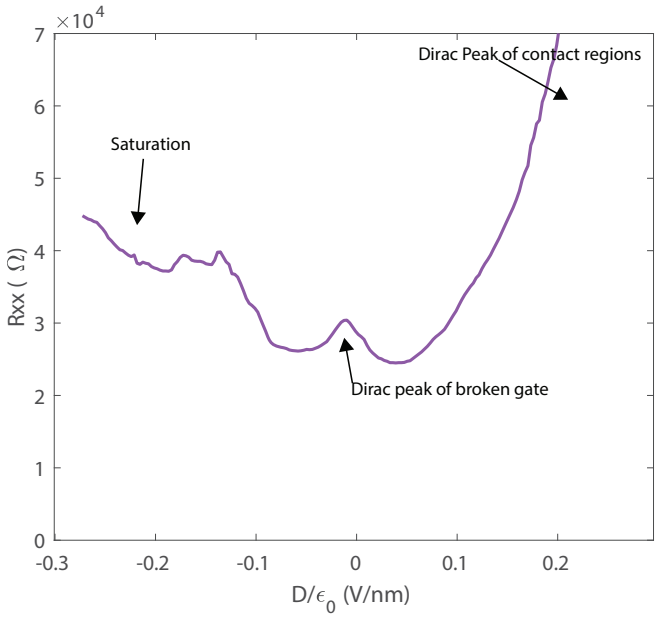

Figure 3.3: Dirac peak resistance as a function of displacement field in device-1. Saturation appears in the negative D-field regime. A large peak coming from the Dirac peak of the fixed gates appears on the posative D-field regime, washing out other possible features. A small peak at D=0 is the Dirac peak of an ungated strip of the device, due to one broken backgate.

device, also appear in the sweep. However, no oscillations were observed, except for those coming from the quantum Hall effect in the fixed backgate regions of the device. Although the ability to choose the device area with the various gates seems promising, in practice the fixed-gate regions of the device provide enough background features (their Dirac peaks and quantum Hall features) to make it difficult to see other features in the data. A better solution would be to be able to image the network structure before device fabrication, and intentionally fabricate on a chosen region.

3.3 Seeing the network

In the devices in Sections 3.1 and 3.2, fabrication and measurement are blind to the particular structure of the network and can only probe average mesoscopic behavior. The ability to image the dis-

location network in a prospective device opens the door to a variety of interesting experiments that can be designed around knowing the specific network pattern. In particular, we can imagine designing devices that specifically inject current along particular domain walls. Then, for instance, we can measure the transmission into each of the six paths emanating from a node. The chirality of the valley states should favor transmission in certain directions. A similar experiment was done by Li et al[41] using rectangular, gate-defined regions of opposite electric field to create the topological modes. It would be interesting to measure it in the natural dislocations in the twisted bilayer.

Though TEM is great for visualizing and characterizing the domain walls, it is not ideal for integrating with a device. There is the concern of beam-induced damage, as well as differences in substrate requirements (see Section A.2.2). An imaging technique that works on silicon substrates yet can still probe through top boron nitride (BN) would be desirable.

Near-field scanning optical microscopy (NSOM) can do so. This technique excites, and images the standing waves of, surface plasmon polaritons in the material. In doped graphene, NSOM can image the domain walls of a twisted bilayer through 4 nm of too BN.[42] To make a useful device, however, it is necessary to have top and bottom gates to apply the electric field that can open a gap in the Bernal bilayer regions. A metal topgate is not transparent to the light. A graphite topgate would wash out the signal from the graphene, as it is active in the same wavelengths.

One option is to use a topgate material that is transparent in the infrared range at which the imaging occurs, such as MoS_2. We fabricate a twisted graphene stack with 2 nm top BN and bilayer (for better contacts) MoS_2 topgate, contacted by aluminum . Because MoS_2 is a semiconductor, the contacts to the topgate only work well in the combination of positive backgate voltage and negative topgate voltage, but in this regime we apply displacement field of up to $0.75\varepsilon_0$ V/nm.[43]

However, we can get much more robust imaging through thicker BN layers by using NSOM to excite the hybrid phonon-plasmon-polariton in the graphene-BN system.[44] Because the BN phonon mode is contributing to the signal, thicker BN is possible without washing out the sig-

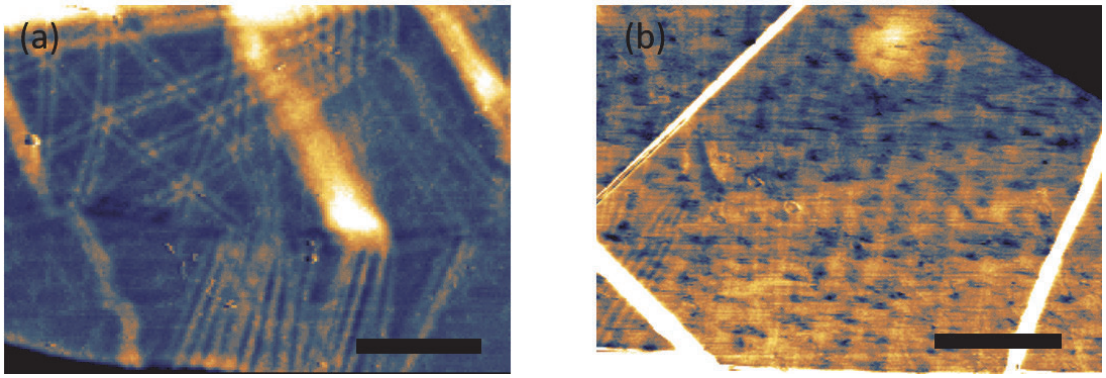

Figure 3.4: NSOM images of twisted graphene stacks (a) with 15 nm top BN, and (b) with 10 nm top BN and trilayer graphene topgate. Scale bars are 1 μm. [images collected by Yue Luo]

nal. Good image contrast was found with up to 15 nm of top BN. Adding a graphite topgate adds a background signal to the image that reduces contrast, but is still good enough to determine domain wall locations with 10 nm top BN and a trilayer graphene topgate. Example images are shown in Figure 3.4. For best imaging conditions, total BN thickness (top plus bottom) should be about $30 - 40$ nm, with top BN kept below 15 nm without a topgate, and below 10 nm with a 3-4 layer topgate. Dielectrics and gates of these thicknesses are still thinner than those used in most devices but are much more in line with the thicknesses needed for good device quality than those required by the purely plasmon-based imaging.

3.4 Fabrication of devices

With imaging ability in hand, we turn to integrating it with device fabrication. It is known from magic angle and other twisted devices that the angle in the final device does not always remain the same as the target during stacking, and seems to sometimes globally rotate toward zero during fabrication.

Figure 3.5 shows how the domain wall structure changes during fabrication. During the deposition of gold marks to use for alignment, the structure changed slightly, in the direction of larger

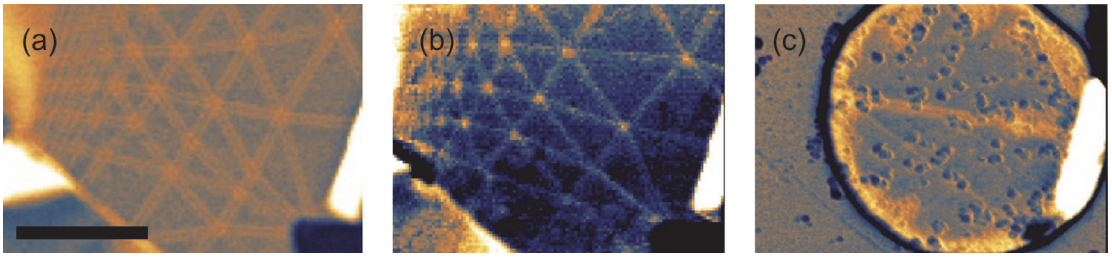

Figure 3.5: NSOM images of the same twisted graphene stack (a) before fabrication, (b) after deposition of alignment marks, and (c) after etching a small device area. Scale bar is 1 μm. [images collected by Yue Luo]

domains, likely due to heat from the thermally-evaporated metal. After etching away most of the stack, leaving a 2 μm diameter circle, the twist was almost entirely gone, leaving one domain wall. This is likely due to the creation of a small sample, which is easier to globally rotate.[45]

To pin the structure in place during fabrication, we try etching 300-400 nm-wide holes where the ends of the contacts will be, as the first fabrication step. Figure 3.6 shows that after some fabrication steps, the structure near the device area appears to have negligible change. However, it is also the case that the structure within the device area is not resolvable, perhaps because of residue from PMMA. This makes it hard to be sure that the domain walls are present in the device when fabrication is complete. Completed devices are shown in Figure 3.7.

3.5 Electronic transport measurement

Electric displacement field must be applied in order to access the topological edge modes at AB-BA boundaries, by gapping out the AB and BA regions. In Chapter 2, we saw that the extent to which distinct AB and BA regions form depends on angle. According to a calculation that does not include relaxation, the energy bias needed between the layers to separate the 1D states from the bulk gap needs to be at least about 90 meV for a twist angle of 0.2°, or 45 meV for 0.1°.[38] Other calculations imply that the nature of the gap size is larger for a relaxed structure than unrelaxed.[46,47] Still, it is hard to say from theory what the necessary experimental conditions are.

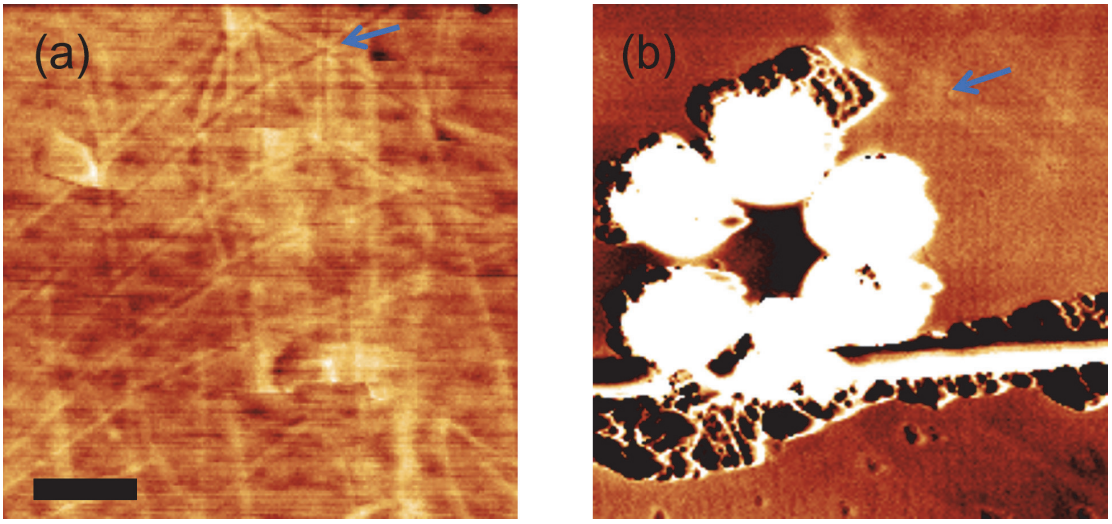

Figure 3.6: NSOM images of the same twisted graphene stack (a) before fabrication, (b) after etching pinholes and filling them with gold. Blue arrows point to what appears to be the same node. Scale bar is 1 μm. [images collected by Yue Luo]

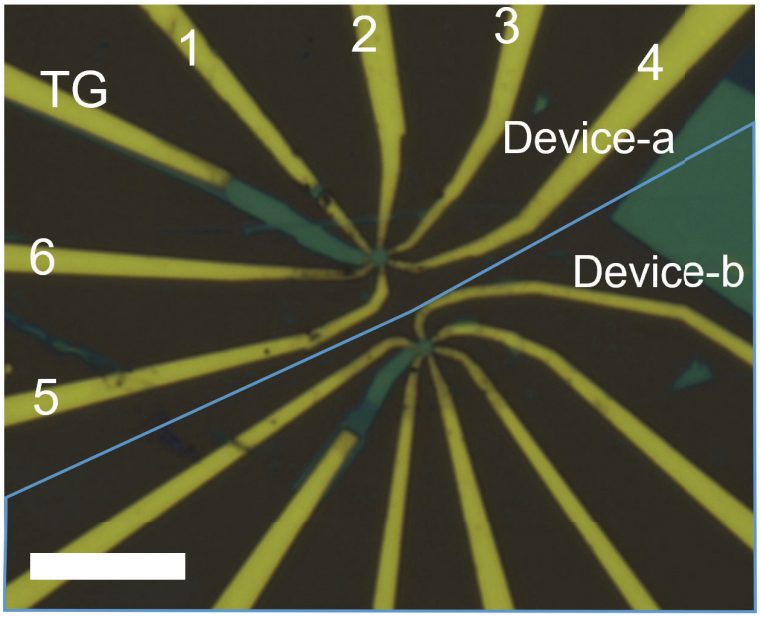

Figure 3.7: Optical image of a completed pair of single-node devices. Device-a is the one discussed in this text. Scale bar is 10 μm.

3.5.1 Dual gating

Dual (top and bottom) gates are necessary to vary the carrier density (n) and displacement field (D) separately.

Given V_B and V_T, the voltage applied on back- and top-gates respectively, and C_B and C_T, the capacitance per unit area of the gates, we have

$$n = \frac{C_B}{e} V_B + \frac{C_T}{e} V_T \tag{3.1}$$

and

$$D = (C_B V_B - C_T V_T)/2. \tag{3.2}$$

How the applied displacement field relates to the gap size is not perfectly clear, due to screening, charged impurities, and in-gap states, which can reduce the experimental gap from the theoretical prediction for a given displacement field.[4] If we ignore these effects and model the bilayer graphene as a dielectric with dielectric constant ε_b between the layers, then an applied displacement field D would produce an energy difference between the layers of

$$U = etD/\varepsilon_b \tag{3.3}$$

where t is the separation between the layers, 0.34 nm and $\varepsilon_b \approx 3$.[48] Experimental gaps in transport (usually in the range $|D| \lesssim 1$ V/nm) have been measured to be about 10 meV per 0.1 V/nm of displacement field.[49,50,51] In our experiments above (Sections 3.1,3.2), the saturation of and comparatively low resistance at charge neutrality, which we saw as evidence of the topological 1D states, began around $D/\varepsilon_0 = 0.2$ or 0.3 V/nm. A similar threshold is observed in a single gate-defined domain wall.[51] Aharanov-Bohm oscillations due to current circulating around the moiré cells have been observed at $D/\varepsilon_0 = 0.5$ V/nm.[52]

All together, this suggests that although the experimental gap may not be exactly predicted by theory, it is likely that the 1D network states can be accessed with displacement fields by around 0.5 V/nm, which is easily achievable with BN gate dielectric.

3.5.2 Measurement

Measuring device-a at a temperature of 2K, we demonstrate that we have achieved dual gating of the imaged graphene device. Figure 3.8 shows the two-terminal resistance across the device while varying top and bottom gate. In this gate range, we have applied displacement field approximately $|D/\varepsilon_0| = 0.15$ V/nm at the corners. We are interested in the behavior of the Dirac peak resistance versus D. An increase in resistance with $|D|$ would imply the formation of the bilayer gap, and a saturation would be consistent with the presence of topologically protected states.

In this case, the Dirac peak resistance decreases with $|D|$, behavior characteristic of uncoupled monolayers. However, it is difficult to conclude whether this is indicative of the coupling of the graphene layers, since the device has significant leakage current to the gates, in the range of tens of μA. We conclude that detailed experiments on this device are not feasible (see discussion in Appendix B).

3.6 Outlook

We have demonstrated the ability to integrate a domain wall imaging technique with a dual-gated device, without compromising on the quality of the topgate or the presence of $\geq$ 10 nm BN capping layer. This paves the way for future experiments based on incorporating specific domain wall structures into the device.

Future devices of this type should be made with graphite backgate, for better quality and control. When the graphite backgate is present, the silicon (global) backgate can be used to tune the regions

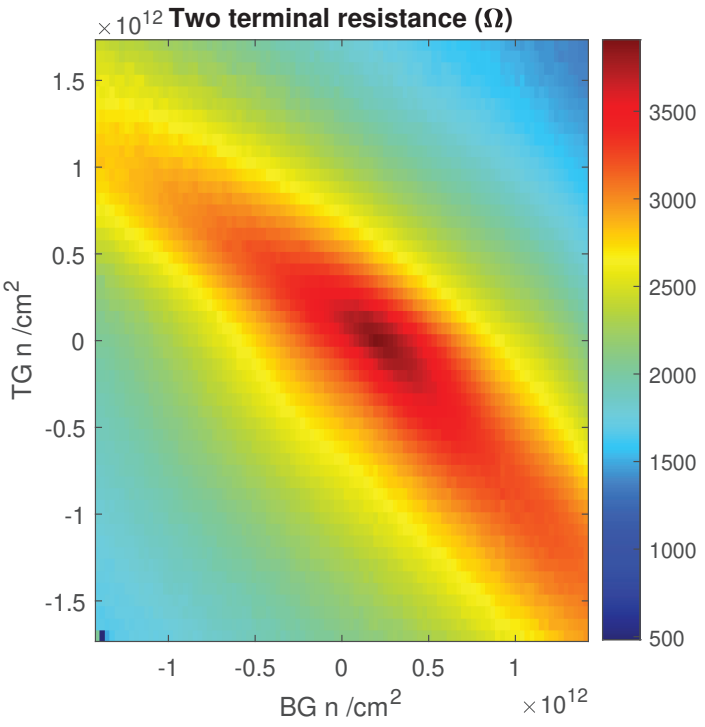

Figure 3.8: Dual gating of the imaged device. x- and y-axes are density of carriers induced by top and bottom gates.

near the contacts that are not covered by the topgate, preventing resonances at the contacts.

Experimental measurements of the scattering in each direction at the nodes of the moiré pattern will be useful to interface with theoretical calculations based on the scattering matrix at the nodes.[53] Experiments based on single nodes, as explored here, may prove to suffer from issues such as increased intervalley scattering due to the close proximity of sample edges, or too much contact resistance.

Aside from single-node experiments, there are many options for transport combined with imaging. Imaging could be used to align contacts to inject current along a certain domain wall direction, in a mesoscopic or multi-domain region. This way, scattering into different directions of the moiré lattice could still be observed, and guaranteeing the domain walls are still present after fabrication would be easier with a larger device region. With multiple domains present, pseudo-Landau levels could be observed.[54] We hope that future experiments will be inspired to use imaging to design devices around known network geometries.

4

Quasicrystal graphene

In Chapter 2 we saw that twisted bilayer graphene has interesting interlayer interactions at angles near 0°, that modify the electronic properties. One could wonder if 30°, the upper limit on twist angle and a rotationally symmetric structure, is also a regime of coupling between the layers.

At 30° (Figure 4.1), graphene lattices are non-periodic, and because of the twelve-fold rotational symmetry (if you consider the two lattices as projected into the same plane), are in fact quasiperi-

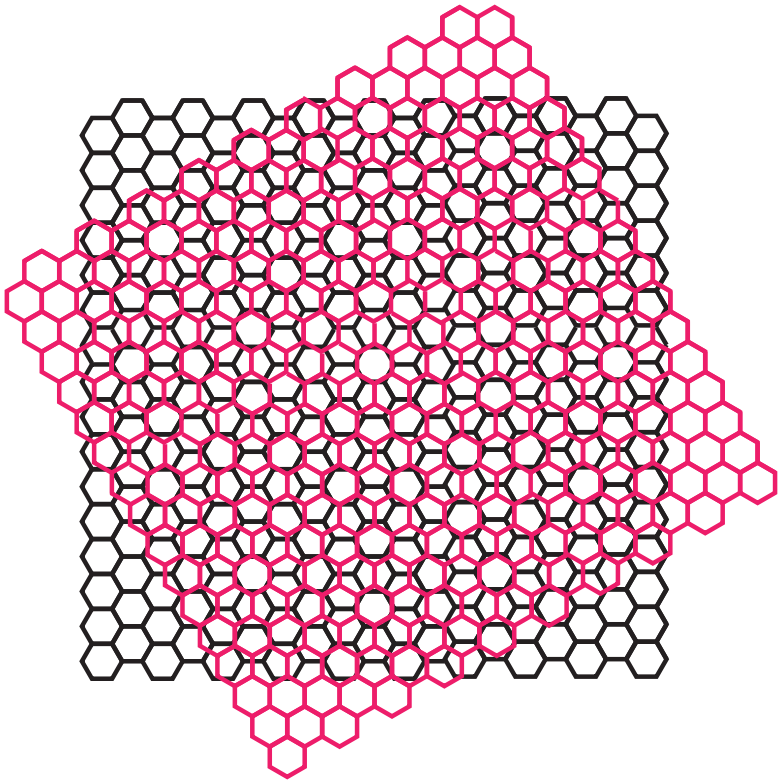

Figure 4.1: Two honeycomb lattices with 30°twist. The resulting pattern is quasiperiodic.

odic. The structure is no longer characterized by a superlattice, as the moiré length has decreased to the same scale as the atomic lattice.

Quasicrystals are interesting because they are neither periodic nor nonperiodic systems. Though there isn't translational periodicity, Conway's theorem states that any feature of size d can be found again within a distance $2d$. Electronic properties scale differently from both crystals and disordered systems.[55] Quasicrystals, including 30° graphene, have very low friction because no translation of the top layer is any better or worse in terms of registry with the atoms below it.[56]

Angle-resolved photoemission spectroscopy (ARPES) work by Ahn et al[57] implied that the 30° condition in graphene might have interesting coupling, wherein replicated Dirac cones via Umklapp scattering could be found in the first Brillouin Zone with lower-than-normal attenuation with

distance. Their data suggest that the interlayer coupling at 30° is stronger than at other large angles. Later theoretical work[58,59] indicates that the coupling at 30° may be similar to that of other large angles, with no interesting features in the density of states until 1.5eV, which is beyond the range easily probed by transport. It is possible the strong reflections in the ARPES data may be from substrate effects, rather than a stronger coupling that emerges at 30°.

We probed a 30° system via transport and observed behavior typical of decoupled layers.

4.1 Quasicrystals with 30° twist angle

An important question when investigating this system is how close to 30° one needs to get to make claims about the quasicrystal. Any quasicrystal structure can be approximated by arbitrarily close periodic structures, known as approximants.[60] Ahn et al consider the approximant to the graphene quasicrystal consisting of a twist of 29.9576°, and find that the expected positions of the reflected Dirac cones would be noticeably different from the twelve-fold symmetric pattern observed in their data. However, unless there is a discontinuity at 30°, at such a close angle the strength of the reflections would likely be similar to the exact 30° condition. Hence, we aim to create samples as close to 30° as possible, but pragmatically there is going to be some angle error. We took two approaches, experimentally, to get close to 30: tear-and-stack mechanically exfoliated graphene,[5,6,34] and CVD graphene grown with 30° bilayers. For both approaches, we use TEM to confirm angle accuracy.

4.1.1 Mechanical approach

We mechanically stacked graphene at 30° by tearing a monolayer and rotating the substrate with a 360° manual rotary stage with a micrometer drive. The stack was placed on a 50 nm SiN membrane and annealed at 350°C. TEM electron diffraction showed an average angle of $30.22 \pm 0.09°$. For methods on measuring angles from diffraction, see Section 2.2.1.

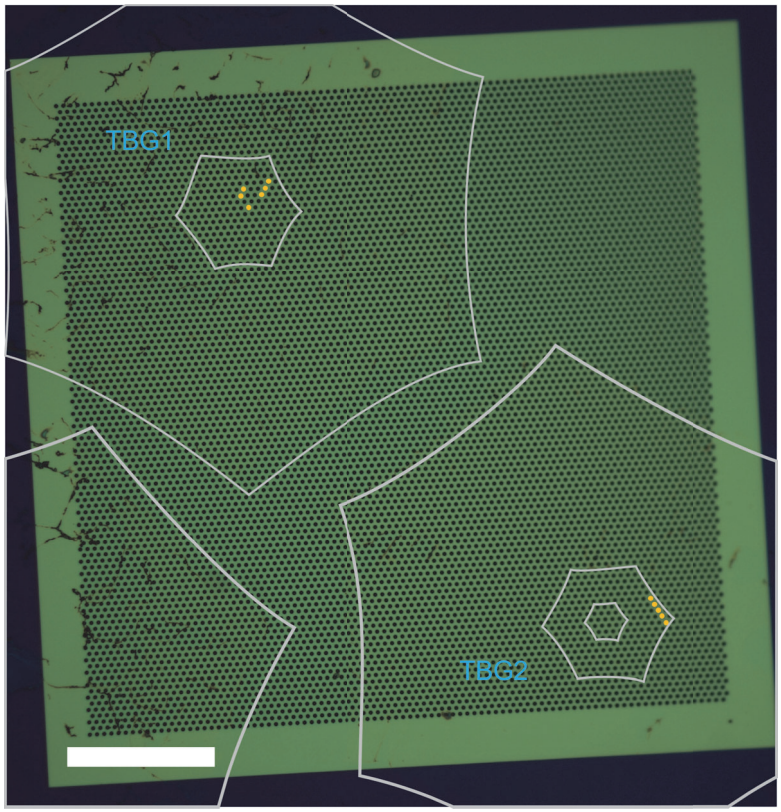

Figure 4.2: Optical image of a holey SiN TEM membrane with CVD graphene crystals (outlined by the grey lines), two of them showing large 30° regions. Scale bar is 100 μm. The yellow dots indicate the holes over which we measured SAED and determined the values of twist angle listed in Table 4.1.

This stack was transferred from the SiN membrane to an ordinary silicon chip (see Section A.2.2 for details) to be fabricated into a device. This became device A.

4.1.2 Growth approach

When it comes to targeting a specific, high symmetry angle, growth may be more controlled than mechanical stacking. We used graphene grown by a Chemical Vapor Deposition (CVD) technique that is selective for 30° bilayers.[61] To confirm the angle, TEM studies were done on representative 30° bilayers, transferred by wet transfer onto SiN membranes with holes (Fig. 4.2).

TBG1	29.79°	29.88°	29.91°	30.09°	29.82°	29.97°
TBG2	29.95°	29.93°	29.99°	30.00°	29.95°	

Table 4.1: Measured angle values from SAED at 5 or 6 positions on two different CVD graphene crystals.

The twist angle was measured from SAED images by subtracting the average angular orientation of one layer's Bragg peaks from those of the other layer (See Section 2.2.1). An upper bound on uncertainty of 0.3° is estimated from a single layer Bragg peaks' standard deviation from 60°. Measured values for each crystal are listed in Table 4.1. A diffraction pattern from TBG2 is shown in Figure 4.3. Finally, combining the twist angle values obtained over the individual holes, we obtained a spatially-averaged twisting of $29.91° \pm 0.11°$ for TBG1 and $29.96° \pm 0.03°$ for TBG2. We conclude that the growth produces twist angles of 30° within the precision of our measurement.

A different flake of CVD graphene was removed from the copper substrate by a dry transfer process, made possible by oxidizing the copper,[62] and fabricated into device B.

Both devices, A and B, were coated with aluminum oxide as a gate dielectric, and topped with a gold topgate.

4.2 Magnetotransport in quasicrystal samples

Our goal in transport is to see if there is evidence of electronic coupling between the two layers at 30°. For twist angles above about 2°, twisted bilayer graphene behaves like two electronically-decoupled monolayers, as shown for instance in device (ii) in Section 3.1. To investigate the 30° devices, we make use of the two gates to vary carrier density (n) and displacement field (D) separately. As a function of topgate and backgate voltage, n and D are given by Equations 3.1 and 3.2.

Device A is measured at a temperature of 1.7K, where it has carrier mobility of $40,000$ cm^2/V·s. Sweeping magnetic field versus a combination of gates such that $D = 0$, quantum hall plateaus are seen at filling factors $\pm 4, 12, 20\ldots$: double the monolayer sequence. (Figure 4.4b). At finite

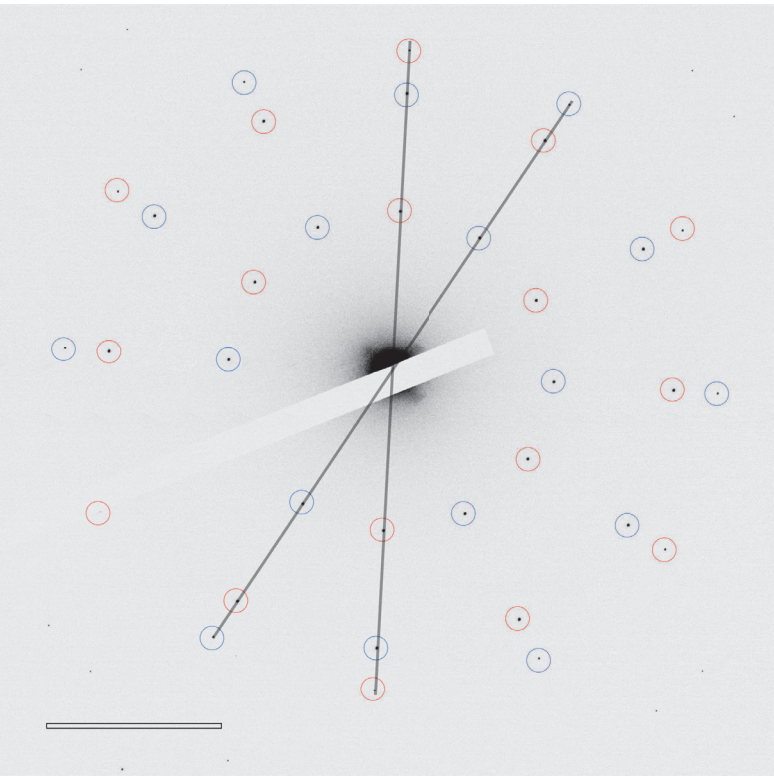

Figure 4.3: Diffraction pattern of nearly exactly 30° CVD graphene. Red and blue circles highlight the diffraction peaks of the different layers. Traced lines indicate the 12-fold rotational symmetry. Scale bar is 5 nm^{-1}.

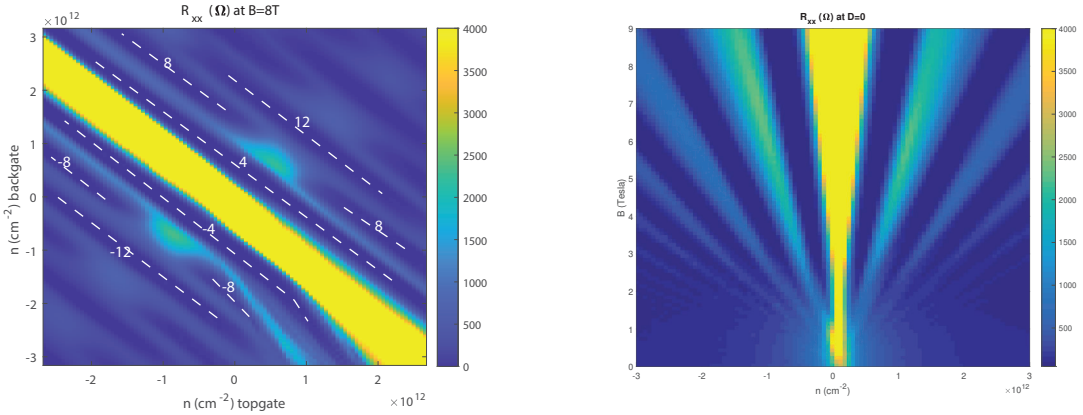

(a) R_{xx} at 8T, with filling factors of plateaus labeled

(b) Fan at D=0. Plateaus are at $\nu = \pm 4, 12, 20$ etc.

Figure 4.4: Quantum Hall data from 30° Device A

field, application of both gates causes the degeneracy to split and recombine as a function of D field (Figure 4.4a shows this at $B = 8$T). This is consistent with the behavior of decoupled monolayers. At $D = 0$, we would expect to see the monolayer band structure doubled, resulting in an additional two-fold degeneracy in all quantum hall states. As shown in Sanchez-Yamagishi et al,[37] application of nonzero D shifts the two layers opposite directions in energy so that they alternately lose and regain this degeneracy as levels cross.

Calculations of the hall conductivity, σ_{xy} done at 8T, illustrate the degeneracy more clearly (Figure 4.5). Hall conductivity σ_{xy} is calculated from the measured longitudinal and transverse resistivities ρ_{xx} and ρ_{xy} by:

$$\sigma_{xy} = \frac{-\rho_{xy}}{\rho_{xx}^2 + \rho_{xy}^2}. \tag{4.1}$$

For a linecut of the dual gate sweep such that $D = 0$, plateaus are present at integers with degeneracy of 8 (and offset from zero due to the π Berry phase in the graphene Dirac points[63]). A linecut from slightly higher $D/\varepsilon_0 \approx 0.15$ V/nm shows that the degeneracy has split into units of 4, indicating that layer degeneracy has been lifted by the D field. There is a slight plateau forming at $\nu = \pm 1$, which is likely due to spin or valley degeneracies being lifted by the magnetic field.[64] High magnetic

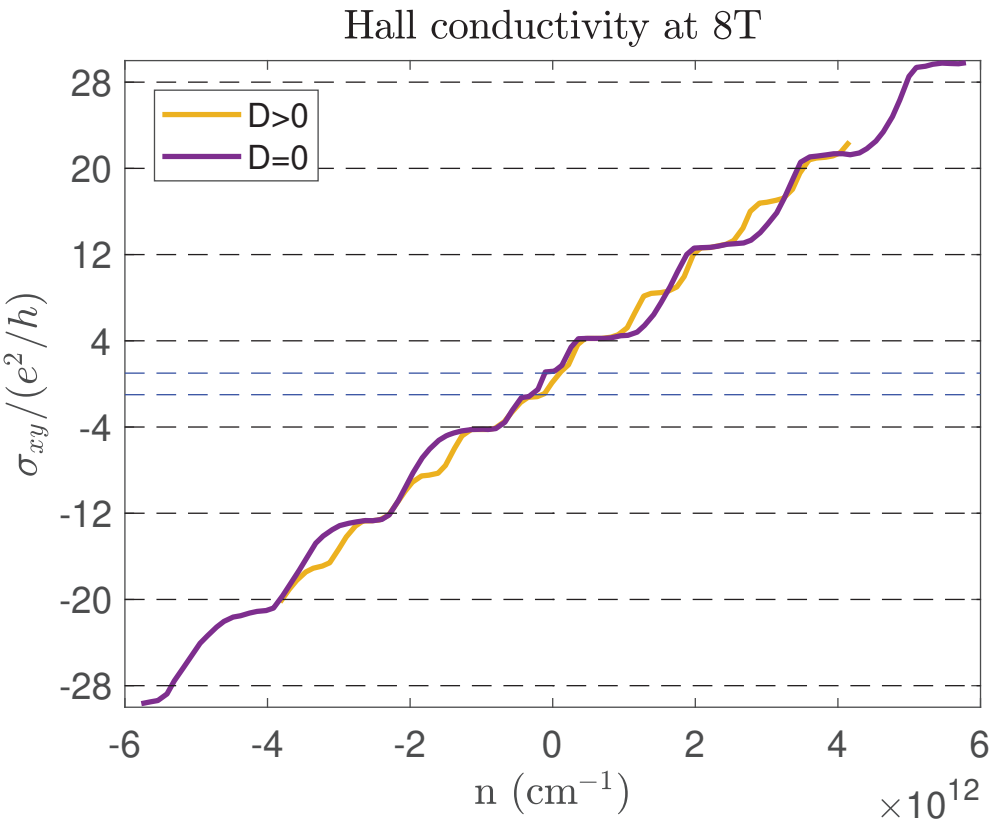

Figure 4.5: Line cuts of σ_{xy} at 8T, at D=0 and at D/ε_0=0.15V/nm. Dashed black lines are at $\pm 4, 12, 20$. Dashed blue lines are at ± 1.

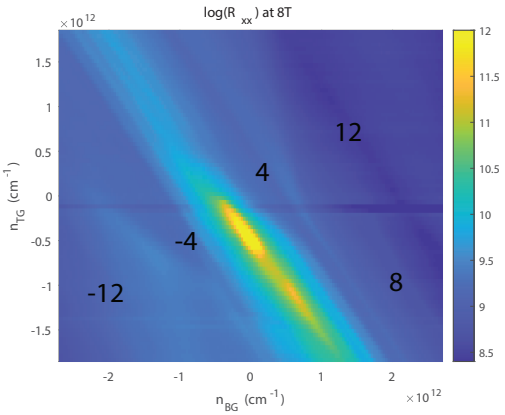

(a) Log of R_{xx} at 8T. Filling factors of faint features are superimposed.

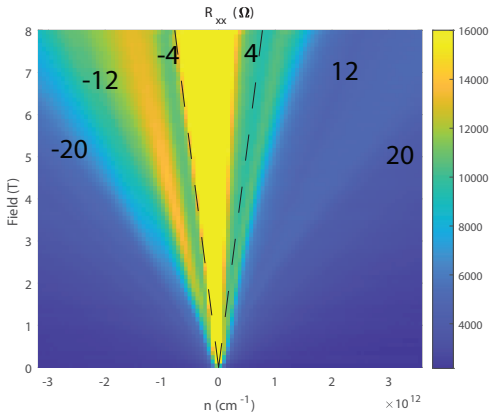

(b) Fan at D=0. Oscillations are visible at $\nu = \pm 4$ (dashed lines) and faintly visible at $\nu = \pm 12, 20$.

Figure 4.6: Quantum Hall data from 30°device B.

field data shows more degeneracies lifting but is still consistent with the decoupled monolayers picture (Appendix B).

It is possible that CVD growth can achieve more precise angle condition than mechanical stacking. Hence we investigate Device B. Device B is lower quality, with mobility $2,000$ cm^2/V·s. This likely indicates the oxidation process used to release the CVD grown graphene from the copper growth substrate was not implemented in a clean way. The method has been shown to attain mobilities of $350,000$ cm^2/V·s,[62] so the oxidation method may not intrinsically degrade the graphene.

The quantum hall data from device B is of lower quality, but dips in longitudinal resistance R_{xx} are visible indicating a similar set of features to device A (Fig. 4.6).

Overall, it is found that the low energy band structure does not appear modified by the 30° condition, and it is similar to other large twist angles.

5

Reunderstanding moiré through strain

If lattices were perfect, with no distortions other than twist, the moiré domains should be made up of equilateral triangles, with Burgers vector parallel to the domain walls (screw type dislocations) as discussed in Section 1.3. In TEM experiments, this is never exactly what we see. There is spatial variation in domain size, triangles can be stretched to shapes far from equilateral, and the orientation of the domain walls can stray from parallel to the Burgers vector. In Figure 5.1, these

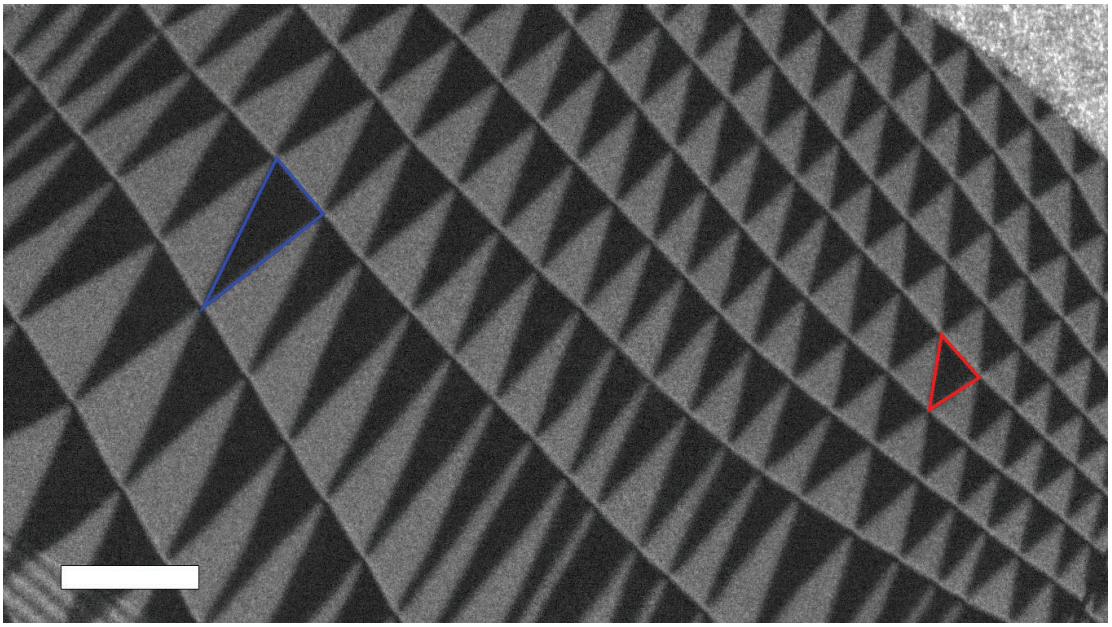

Figure 5.1: Example of changes to domain size, shape and orientation across a sample. Scale bar is 200 nm.

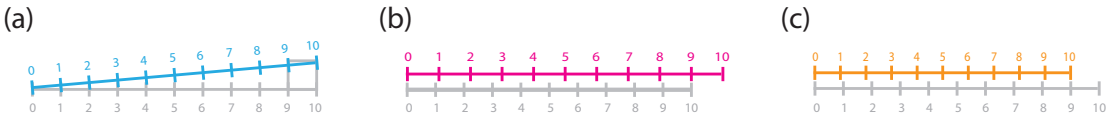

Figure 5.2: Distortions to a lattice axis that can produce moiré. (a) rotate, (b) stretch, (c) shrink.

differences can be seen between the red-outlined and blue-outlined triangles. Such variation is attributed to the relative strain between the stacked atomic layers.[65,66,67]

At the same time, the manner in which the domains and domain walls are connected at six-fold nodes seems invariant, as the structure can be distorted but domains' nodes and edges cannot go away except by being pushed off the edge of the sample. Thus we are inspired to investigate whether there is a topological nature to the network, and how it is affected by strain.

5.1 Strain mapping: simple algorithm

The moiré pattern and all its associated quantities such as moiré vectors, Burgers vectors, twist angle, and strain, can all be related to a vector field $\vec{u}$ that describes the local in-plane shift, or displacement, between the two lattices. By exploring the relationships between these quantities, we can determine the approximate strain field from TEM dark field images.

5.1.1 Meaning of strain

The strain matrix is derived from the displacement vector field, $\vec{u}$ which describes the shift in positions of a lattice ($\vec{x}_2$) compared to a reference lattice ($\vec{x}_1$): $\vec{x}_2 = \vec{x}_1 + \vec{u}$. Normally, the reference lattice is the intrinsic lattice of the material, where any changes in bond length or angle would cost energy and would be described as strain.

In this case, however, the reference lattice (with coordinates $\vec{x}_1$) is the bottom layer of the material, and the displaced lattice ($\vec{x}_2$) is the top layer. Thus, what is evident in a TEM image of a moiré pattern is really the relative strain between the two lattices (also called heterostrain), and not the absolute strain relative to the undistorted material. For example, if both lattices were expanded by 1%, there would be no moiré pattern and hence no heterostrain to measure.

Another important note is that the strain distribution we are considering is essentially the strain distribution prior to the lattices meeting together and relaxing into domains. We can use the positions of the dislocation lines to locate ourselves in the moiré pattern, and determine the $\vec{u}$ field that produced that pattern, but we are not measuring the post-relaxation strain distribution, in which the strain is concentrated into domain walls and AB and BA domains are largely unstrained. The strain in the domain walls can however be measured by 4D STEM (scanning TEM).[68]

The strain matrix is defined by taking derivatives of the $\vec{u}$ field. There are multiple conventions for defining the strain matrix, but generally it refers to the symmetrized matrix (Equation 5.1), in

which rotations are removed (intuitively: because rotating the lattice does not cost energy and thus should not be counted as strain).

$$\varepsilon = \begin{pmatrix} \frac{du_x}{dx} & \frac{1}{2}\left(\frac{du_x}{dy} + \frac{du_y}{dx}\right) \\ \frac{1}{2}\left(\frac{du_x}{dy} + \frac{du_y}{dx}\right) & \frac{du_y}{dy} \end{pmatrix}. \tag{5.1}$$

Without symmetrizing, the gradient of the $\vec{u}$ field is known as the displacement gradient matrix, $\overline{d}$ (Equation 5.2), and will be of much use to us.

$$\overline{d} = \nabla\vec{u} = \begin{pmatrix} \frac{du_x}{dx} & \frac{du_x}{dy} \\ \frac{du_y}{dx} & \frac{du_y}{dy} \end{pmatrix}. \tag{5.2}$$

The vector $\vec{u}$ can be recovered by integrating $\overline{d}$ over distance; assuming the relevant distance is small or the strain is spatially uniform, this becomes

$$\vec{u} = \overline{d}\vec{x}_1. \tag{5.3}$$

Thus, $\vec{x}_2 = \vec{x}_1 + \overline{d}\vec{x}_1$ or

$$\vec{x}_2 = (1 + \overline{d})\vec{x}_1 \tag{5.4}$$

5.1.2 Meaning of moiré length

The moiré length is the distance over which the lattice $\vec{x}_2$ has been shifted by a unit vector with respect to lattice $\vec{x}_1$, creating a local return to the starting configuration.

Consider the shift vector $\vec{u}$, defined as the in-plane vector difference between closest equivalent lattice sites in the top and bottom layer (e.g. the blue vector in Fig. 5.6a). If we twist our lattices about a point where two atoms are stacked on top of each other, the origin has $\vec{u} = 0$. But as we travel away from the origin in a direction $\vec{x}$, the displacement $\vec{u}$ becomes increasingly larger until

we reach the point where the lattices have diverged by a whole unit cell ($\vec{u} = \vec{a_\alpha}$ where $\vec{a_\alpha}$ is the α_{th} lattice vector) and thus are aligned ($\vec{u} = 0$) again, resulting in moiré periodicity. (See Figure 5.2a). (This assumes layer 1 is unstrained. If not it would take a strained version of $\vec{a}$ to obtain the coincident lattice condition.)

A similar story occurs if the lattice constant of one layer is slightly larger than the other. In this case the lattice vector that bridges the gap is collinear with $\vec{x}$. (Figure 5.2(b,c)).

A general interface of two lattices with $\vec{x}_2 = (1 + \overline{d})\vec{x}_1$ has two moiré vectors, and each can have $\pm\vec{a}_1$, or $\pm\vec{a}_2$, (where $\vec{a}_1$ and $\vec{a}_2$ are the two primitive vectors of the lattice) as the condition that brings coincident lattice.

Then the two moiré vectors are

$$\vec{M}_\alpha = \vec{x}_{2,\alpha} = \vec{x}_{1,\alpha} + \vec{a}_\alpha. \tag{5.5}$$

and

$$\vec{M}_\beta = \vec{x}_{2,\beta} = \vec{x}_{1,\beta} + \vec{a}_\beta. \tag{5.6}$$

where $\overline{d}\vec{x}_{1,\alpha} = \vec{a}_\alpha$ and $\overline{d}\vec{x}_{1,\beta} = \vec{a}_\beta$ by Equation 5.3, and $\vec{a}_\alpha$ and $\vec{a}_\beta$ can each be $\pm\vec{a}_1, \vec{a}_2$. If $\vec{a}_\alpha$ and $\vec{a}_\beta$ are collinear (without $\vec{M}_\alpha$ and $\vec{M}_\beta$ being collinear), then the matrix $\overline{d}$ has determinant zero and the moiré pattern is 1D rather than 2D. We will ignore this case for now, and assume that $\vec{a}_1$ and $\vec{a}_2$ are each used once.

Figure 5.3 shows the resulting basis of possible distortions. In Fig. 5.3 (a) and (c), we can see that the conventional types of moiré pattern, namely lattice constant mismatch and twist, are formed when both axes are treated the same (both stretch, both clockwise rotation), whereas Fig. 5.3 (b) and (d) are treated opposite (e.g. one stretch one shrink) and are new combinations.

We can relate the lattice constants $\vec{a}$, the matrix $\overline{d}$ and the moiré vectors, by $\vec{M}_\alpha = \vec{x}_{2,\alpha} = (1 +$

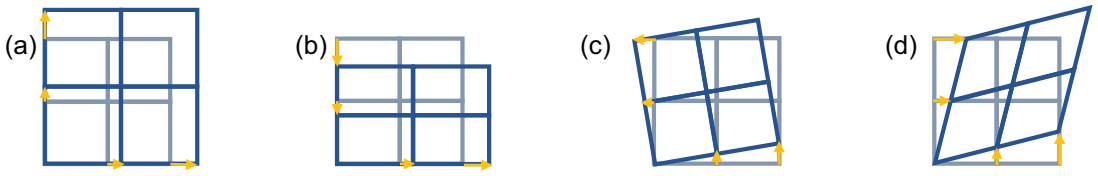

Figure 5.3: Distortions to 2D lattices that can produce moiré. (a) isotropic scaling, (b) uniaxial strain, (c) rotation, (d) shear strain.

$\overline{d})\vec{x}_{1,\alpha}$. Thus if $\overline{d}$ is invertible, $\vec{x}_{1,\alpha} = \overline{d}^{-1}\vec{a}_\alpha$ and

$$\vec{M}_\alpha = (1 + \overline{d}^{-1})\vec{a_\alpha}. \tag{5.7}$$

Putting Equation 5.7 together with the corresponding equation for the other moiré vector, $\vec{M}_\beta$, we get a matrix equation that can be solved for $\overline{d}$ if we have measured $\overline{M}$ and $\overline{A}$:

$$\overline{M}(1 + \overline{d}^{-1}) = \overline{A}, \tag{5.8}$$

where $\overline{M}$ and $\overline{A}$ are 2x2 matrices formed by horizontally concatenating the $\vec{M}$ and $\vec{a}$ column vectors, respectively. (Note that if the two $\vec{M}$'s aren't linearly independent, that is again the $\det[\overline{d}] = 0$ case.

5.1.3 Meaning of Burgers vector

Measuring moiré vectors from a TEM image, Equation 5.8 can be solved for the displacement gradient matrix. The only problem left is which lattice vector $\vec{a}$ goes with which moiré vector $\vec{M}$. We can determine this from the Burgers vector information from the TEM images. Burgers vector is defined as the vector between the endpoints of what would be a closed circuit in a defectless lattice. In a bilayer material with in-plane dislocations, this circuit would be constructed by traversing a certain number of unit cells in the top lattice, going down into the bottom lattice, traversing back the same

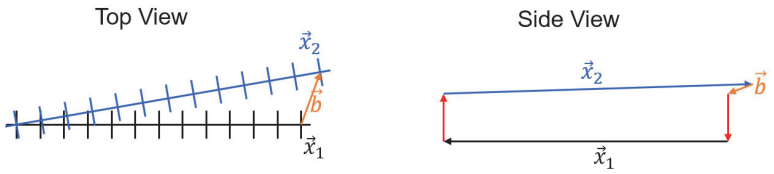

Figure 5.4: Burgers circuit with $\vec{u}_{start} = 0$, such that $\vec{u}_{end} = \vec{b}$

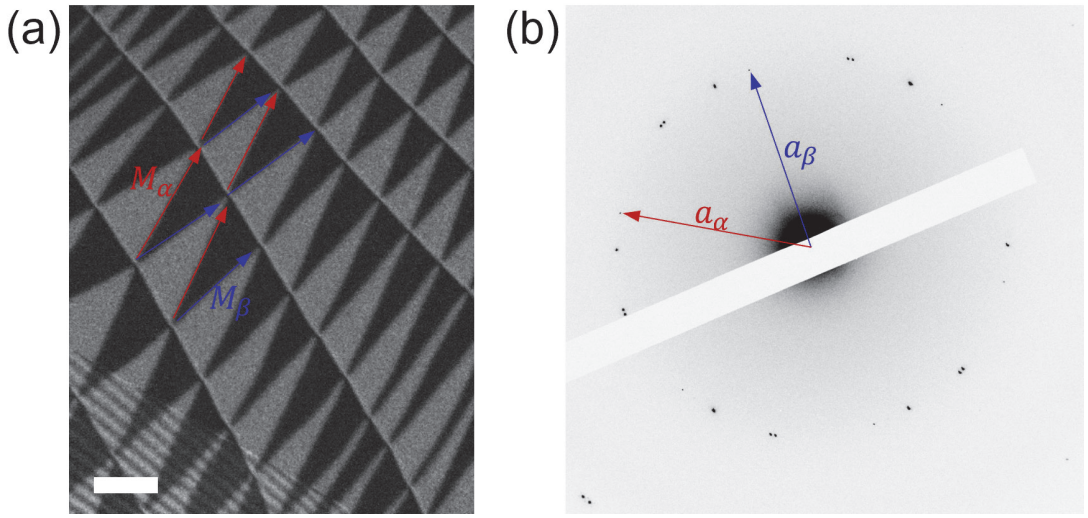

Figure 5.5: Example graphene data showing experimentally measurable quantities. (a) moiré vectors $\vec{M}$ are determined from dark field image (scale bar 100 nm), and (b) AA to AA displacement vectors $\vec{a}$ from diffraction.

number of unit cells, and then moving back up into the top layer. See Figure 5.4. The transition between top and bottom layer requires traveling by the local shift vector $\vec{u}$ and the vertical interlayer vector $\vec{c}$. Thus the Burgers vector for the circuit is $\vec{u}_{end} - \vec{u}_{start}$, or $\Delta\vec{u}$ between the two points.

To determine the $\vec{a}$ to input into the equation, we want to know the $\Delta\vec{u}$ from one AA site to the next. This loop does not circle a dislocation, but rather is perpendicular to a loop that circles the dislocation. As will be more evident when we develop the concept of the configuration space torus, the $\Delta\vec{u}$ between two AA sites is the $\vec{a}$ vector perpendicular to the Burgers vector of the dislocation that connects those two AA sites. The moiré vectors and Burgers vectors can be measured from experimental dark field and diffraction images, as seen in Figure 5.5, allowing one to solve for $\vec{d}$.

This process demonstrates that the combined information of moiré vector and Burgers vector for each moiré cell is sufficient to compute the average displacement gradient matrix of each moiré cell.

5.1.4 Separating Strain Types

The x and y components of the displacement gradient matrix are not so interesting, since our lattice isn't aligned to the x and y axes, let alone cartesian. However, we can decompose any displacement gradient matrix into a sum of four parts: isotropic, uniaxial, and shear strain, plus twist, giving us useful information on the types of strain and displacement.[69]

$$\text{isotropic} = \alpha \begin{pmatrix} 1 & 0 \\ 0 & 1 \end{pmatrix}, \tag{5.9}$$

$$\text{uniaxial} = \beta \begin{pmatrix} 1 & 0 \\ 0 & -1 \end{pmatrix}, \tag{5.10}$$

$$\text{shear} = \gamma \begin{pmatrix} 0 & 1 \\ 1 & 0 \end{pmatrix}, \tag{5.11}$$

and

$$\text{twist} = \theta \begin{pmatrix} 0 & -1 \\ 1 & 0 \end{pmatrix} \tag{5.12}$$

assuming θ is small.

Or, being fully exact, we can use

$$\text{twist} = \begin{pmatrix} \cos\theta - 1 & -\sin\theta \\ \sin\theta & \cos\theta - 1 \end{pmatrix} \tag{5.13}$$

We can compute $\alpha, \beta, \gamma, \theta$ as follows:

$$\beta = \frac{1}{2}\left(\overline{d}_{xx} - \overline{d}_{yy}\right) \tag{5.14}$$

$$\gamma = \frac{1}{2}\left(\overline{d}_{xy} + \overline{d}_{yx}\right) \tag{5.15}$$

$$\theta = \sin^{-1}\left(\frac{1}{2}(\overline{d}_{xy} - \overline{d}_{yx})\right) \tag{5.16}$$

$$\alpha = \frac{1}{2}\left(\overline{d}_{xx} + \overline{d}_{yy}\right) - \cos\theta + 1 \tag{5.17}$$

It is worth noting that uniaxial and shear strain are not independent and can be converted into one another by rotating the coordinate system. We can consider the combined quantity $\sqrt{\beta^2 + \gamma^2}$ which represents total anisotropic strain in the system.

5.2 Topology and antivortices

The nodes where dislocation lines meet in the relaxed moiré system (AA points) have been referred to as topological defects by Alden et al[20]. Turkel et al[70] refer to topological features of the moiré structure in multilayer systems, and emphasize their role in transport as tunable, local concentrations of twist angle. The relevant order parameter, the displacement vector $\vec{u}$, does seem to cycle around AA nodes, like a vortex in the xy model.[71] However, use of an $\mathbb{R}^2$ vector as order parameter, in analogy with an xy model, runs into inconsistencies due to the periodic nature of the lattice. As we have seen, the vector $\vec{u}$ cycles back to the origin when larger than a unit cell of the lattice. In other words, it is defined on a torus.

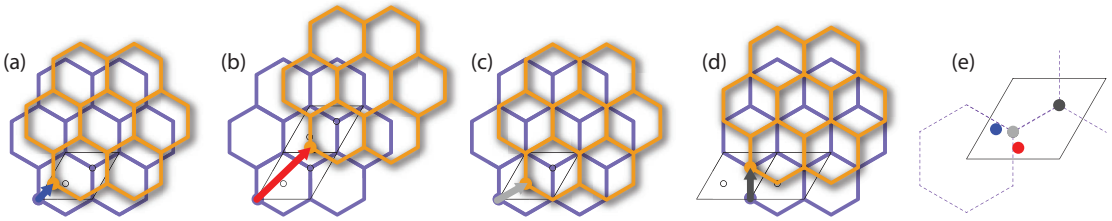

Figure 5.6: (a-d) Definition of shift vector: (a) small shift, (b) shift larger than a unit cell is mapped into the first unit cell, (c) BA shift, (d) AB shift. (e) Shifts from part (a) shown in configuration space. Dotted lines show alternate designation of configuration space unit cell.

5.2.1 The configuration space torus

The shift vector $\vec{u}$ describes the local configuration of the bilayer system. Topological characteristics of a system are determined by the topology of (specifically the homotopy groups of) the order parameter space i.e. configuration space.[72]

The shift vector of a bilayer of 2D lattices exists on a torus, due to the periodic boundary conditions. In Figure 5.6b, the red shift vector is longer than the lattice unit cell. The resulting lattice configuration is equivalent if we shift by the shorter vector obtained by folding into the first unit cell. To make the order parameter well defined, we disregard the $\mathbb{R}^2$ vector form, and represent the lattice configuration as a point in the unit cell with periodic boundary conditions (red dot in Fig. 5.6e).

The high symmetry stackings, BA and AB, are represented by the dark gray and light gray points in Fig. 5.6e, respectively. As the unit cell can be defined in various ways, we will sometimes use the parallelogram definition shown in Fig. 5.6, where AA is the corner, and other times the hexagonal unit cell shown in dotted lines, in which AB and BA are corners of the hexagon.

A torus has nontrivial topology, but the topology of the moiré domain network does not come from the topology of the torus. The topological defects associated with windings of the torus (in any crystal) are dislocations, where the Burgers vector provides winding number.[72]

To determine the sense in which the domain wall nodes are topological, we consider whether all

parts of the torus are equally accessible.

As mentioned, AA stacking (the corner of the parallelogram or center of the hexagonal zone scheme) is the highest energy and AB and BA are the lowest. When relaxation occurs, more area comes to be taken up by AB and BA configurations, and less by AA. Figure 5.7a shows an unrelaxed twisted bilayer of a honeycomb lattice. A coloring scheme of configuration space is chosen and used consistently throughout this work. Configurations centered around AA are colored white, and those centered around AB (BA) are light gray (dark gray). There are three different equidistant paths on the torus to get between AB and BA. The midpoint of each of these paths is colored red, blue, and green respectively. The coloring in real space in Fig. 5.7(a-c) is determined for each point, by interrogating the local shift vector, finding it as a point in configuration space, and adopting the color corresponding to that point.

Figures 5.7b and 5.7c depict a schematic of increasing relaxation strength. (Further details about the computation are found in Section C.1.) Light or dark gray regions, corresponding to nearly AB or BA stacking, take up increasing areas in real space, while AA regions shrink, and red, green, and blue regions evolve into lines. The three paths on the torus between AB and BA, colored red, green, and blue, are each a possible $\Delta\vec{u}$ between AB and BA. Recalling from Section 5.1.3 that $\Delta\vec{u}$ from one domain to another is equal to the Burgers vector, we determine that the red, green, or blue color along a dislocation in the real space map tells us the Burgers vector of that dislocation.

In Fig. 5.7(d-f), points are colored in configuration space only if they are found in the finite-size sample of real space. Thus, lack of point density reveals fewer points in real space correspond to AA stacking, while configurations on the red, green, and blue lines, and especially AB and BA sites, become denser. Therefore, the atomic lattice relaxation process in real space can be viewed as emptying out most of configuration space and populating only the AB and BA points and dislocation lines connecting them.

A similar emptying of AA and concentration at AB, BA, and the colored lines between AB and

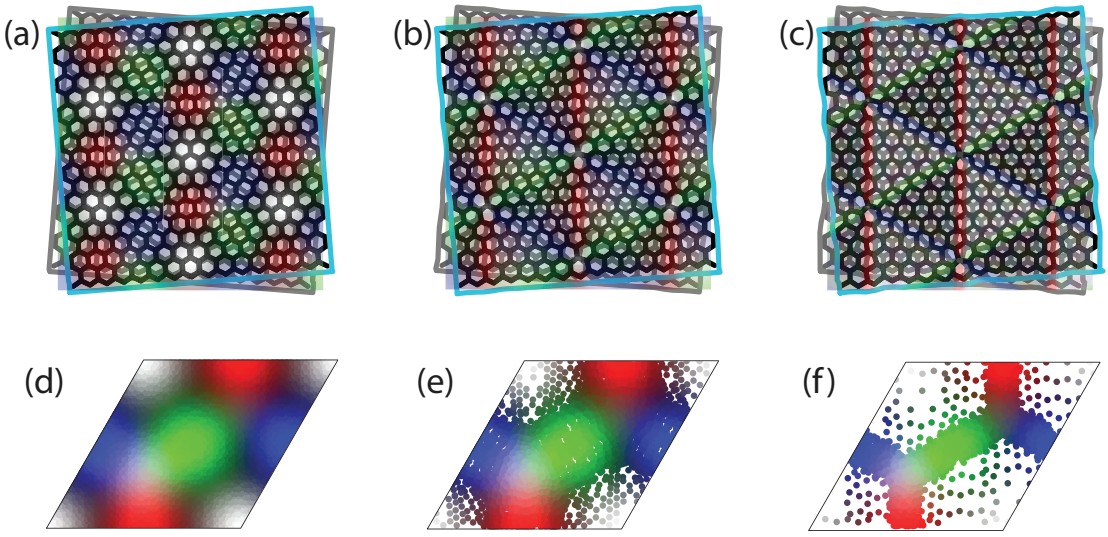

Figure 5.7: (a-c) schematic of real space arrangement for (a) unrelaxed moire structure, (b) partially relaxed moire structure, (c) fully relaxed moire structure. Colors denote region in configuration space corresponding to local stacking order. (d-f) distribution in configuration space of local stacking order sampled at each plaquette of the lattice for (d) unrelaxed moire structure, (e) partially relaxed moire structure, (f) fully relaxed moire structure.

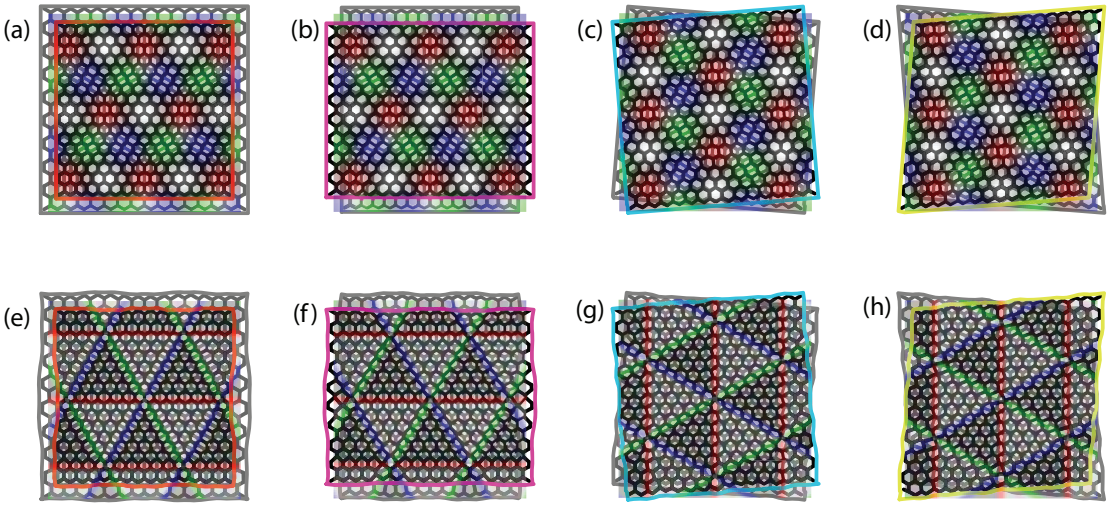

Figure 5.8: Schematics of real space structure for the three strain components. Moiré from (a) isotropic scaling, (b) uniaxial strain, (c) twist, (d) shear strain, and relaxed moiré from (e) isotropic scaling (f) uniaxial strain, (g) twist, (e) shear strain. Colors correspond to configurations, as defined in Fig. 5.7.

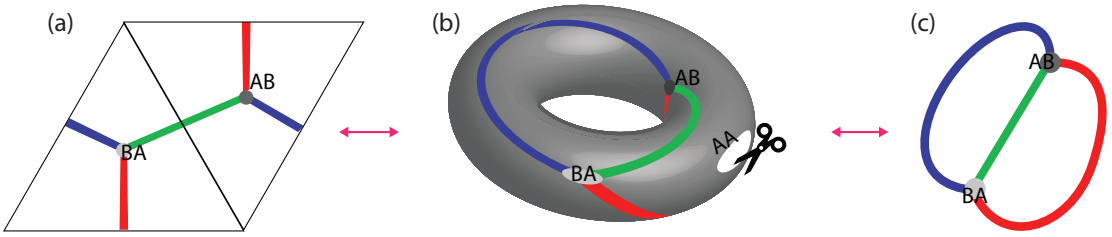

Figure 5.9: Energy troughs on the configuration space torus determine the topology of the network, which can be equivalently viewed (a) on the unit cell, (b) as a torus with a puncture (AA configuration is removed from space), or (c) as theta space

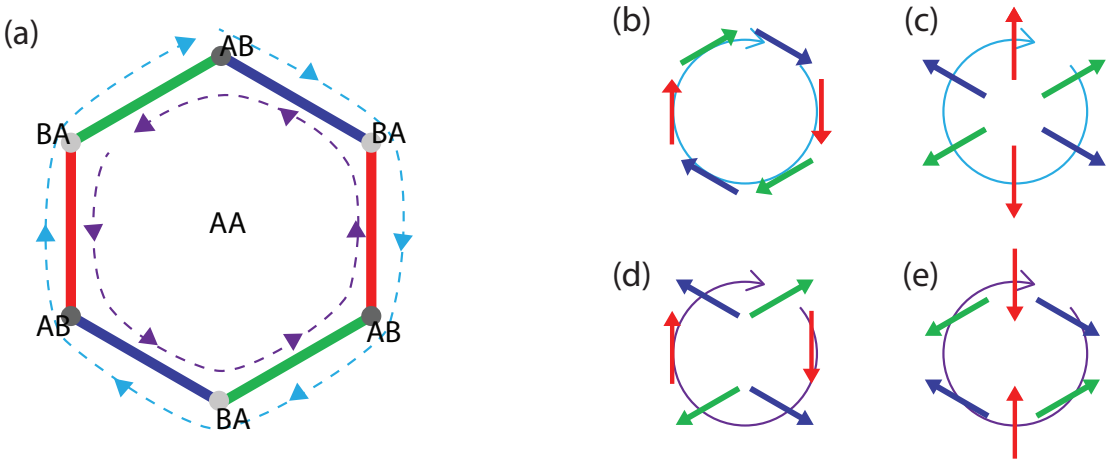

Figure 5.10: (a) Clockwise (counterclockwise) paths traveled in configuration space while making a clockwise loop in real space correspond to vortices (antivortices). (b-c) Burgers vector arrangements in real space corresponding to clockwise (b, c) and counterclockwise (d, e) paths in configuration space. (b) Isotropic, (c) twist, (d) uniaxial, (e) shear.

BA, occurs for the other three strain types. Fig. 5.8 shows the unrelaxed and relaxed configuration of all four components of the displacement gradient matrix. The distinction between each displacement type is the arrangement in which red, green, and blue lines occur around an AA site.

5.2.2 The punctured torus

The low density of points surrounding the AA spot in configuration space allows us to model the system's configuration space as a punctured torus (Fig. 5.9): a torus with the point corresponding to AA removed. Energetically, this can be viewed as an approximation that the stacking fault energy

for the AA configuration is too large to be attainable. Closed paths in real space that encircle a node of the dislocation network now correspond to nontrivial paths in configuration space, that circle the removed point.

Topological defects are characterized by the homotopy group of their configuration space. The punctured torus, Fig. 5.9b, is topologically equivalent to "theta space" (Fig. 5.9c), the space consisting of three paths that join two nodes.

Keeping track of the nonabelian series of traversals of the left lobe and right lobe in the theta space representation leads to an algebraic description of the path, which can be manipulated to extract the vortex winding number, equivalent to the number of vortices contained in a loop. (Details can be found in Appendix D.) More intuitively, a path around a single AA node in real space circles an AA spot in configuration space. The vortex winding number w is $+1$ or -1 if the configuration space loop cycles the same or opposite direction as the real space loop, respectively. If a clockwise path in real space follows configurations along the light blue path in Fig 5.10a, (such as Fig. 5.10 b or c), it is a vortex, whereas if it follows the purple path in Fig. 5.10a, (such as in d and e), it is an antivortex. Comparing the arrangement of Burgers vectors around the loop with the configurations in Fig. 5.8, it can be concluded that twist and isotropic strain produce vortex-type defects at their AA nodes, and uniaxial or shear strain produce antivortex-type defects at their AA nodes.

While moiré patterns and commensurated domain systems with vortex-type nodes have been studied extensively, those with antivortex-type nodes have not been demonstrated. We postulate this is due to the energy required to maintain sufficient strain, whereas twist and lattice constant mismatch can create vortex-type moiré without global strain. Nonetheless, we observe a line of antivortex nodes along a bubble boundary in a twisted bilayer graphene sample, shown in Figure 5.11.

The antivortices can be identified by the red-blue-green order in which the dislocations cross a clockwise loop, the opposite order as vortices. The antivortices, which form along the top edge of a closed-loop dislocation, are each capable of annihilating with a nearby vortex, keeping the net wind-

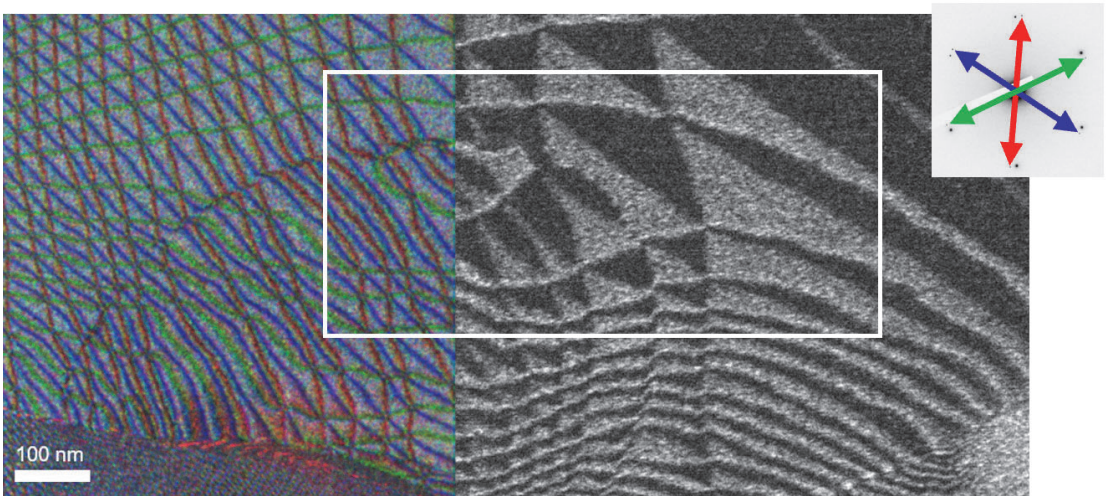

Figure 5.11: Dark field image of tblg containing antivortices along a bubble edge. Left region shows colored second order image, right region shows first order image. Inset: Burgers vector directions corresponding to dislocation colors, superimposed on diffraction pattern. [Image taken by Hyobin Yoo]

ing number w constant within a fixed-boundary region. In Fig. 5.12, loop A surrounds a vortex-antivortex pair, with $w = 0$. Loop D, which surrounds the entire closed-loop dislocation, also has net $w = 0$ as the entire feature could annihilate if the local strain were reduced, in which case it would become similar to loop E. When circling a single antivortex (B) or vortex (C), the winding number is nonzero.

5.3 Strain mapping: complicated algorithm

The method to calculate strain based on Equation 5.8 is limited in that it does not take in to account any curvature of the walls of a moiré cell, but rather assumes AA nodes to be connected by straight lines, and the strain field to be constant over the moiré cell.

The curvature of the domain walls captures some detail about the sub-moiré-scale order parameter field. For example, if a domain wall has a sharp kink in it, it is likely that more strain is concentrated near that kink, rather than evenly distributed along the line. However, full information on

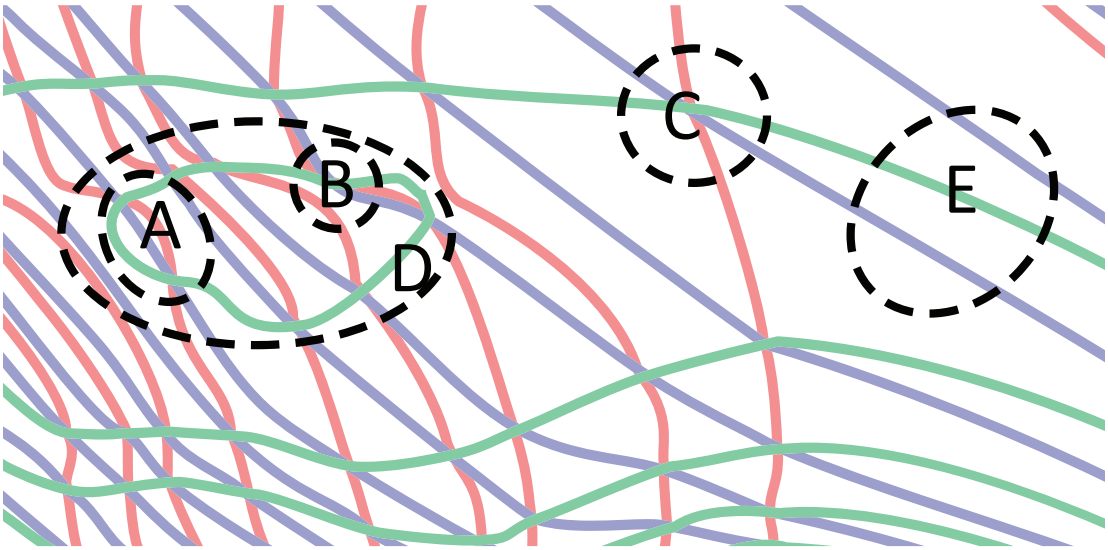

Figure 5.12: Zoom in on tracing of region of white box in Fig. 5.11. Loops are drawn and topological number of each loop is counted. A) Vortex-antivortex pair, w=0. B) Antivortex, w=-1. C) Vortex, w=+1. D) Closed-loop dislocation, w=0. E) Linear domains, w=0.

the order parameter anywhere other than an AA node is not present in the TEM dark field images, so any algorithm will have to make a semi-arbitrary choice of interpolation. As we haven't quantified how accurate this choice is, the algorithm presented in this section is not necessarily better than Equation 5.8 at capturing sub-moiré-scale features.

There is a way that following algorithm is much better, namely that it can handle a vortex-antivortex transition, while the simple algorithm can't process the non-parallelogram domains that necessarily occur next to it. Primarily for this reason, we develop the more detailed algorithm.

5.3.1 Idea of the algorithm

Our algorithm is based around constructing a continuous $\vec{u}$ field, and taking its gradient to obtain the displacement gradient matrix. As we travel along a (for instance) red segment from one AA node to another, $\vec{u}$ will increase by units of $\vec{a_r}$ where $\vec{a_r}$ is the lattice vector that points along the red path in configuration space. Meanwhile, along a given red line, the coefficient of $\vec{a_g}$ stays constant, at an

integer value. At AA nodes, the coefficients of $\vec{a_r}$, $\vec{a_g}$ and $\vec{a_b}$ are all integers (and sum to zero, since the third vector is not independent) .The algorithm consists of assigning values to the coefficients of $\vec{a_r}$, $\vec{a_g}$ and $\vec{a_b}$ where they are known exactly, and using an elastic model to interpolate in between, obtaining an estimate of the order parameter in the continuum.

The first step is to segment the image into red, green, and blue line segments and nodes. Ideally this could be done from the TEM image, but due to noise in the image we focus on analyzing an ideal, traced version of the lines (as in Figure 5.12). An interesting future goal could be to develop an artificial intelligence algorithm to extract this information from the raw image.

Next, line segments are fit by spline curves. Integers are assigned to nodes, and interpolation is performed. Then, derivatives can be taken of the $\vec{u}$ field to obtain the displacement gradient matrix (Equation 5.2) and split into strain components as in Section 5.1.4. More detail on the algorithm is provided in Section C.2.

5.3.2 Strain map results

We demonstrate the strain mapping technique on a heterostructure of WSe_2 and $MoSe_2$, aligned with small twist angle. A dark field image is shown in Figure 5.13. We note that the two domain types are asymmetric in size, which is explained by the fact that a different pair of atoms are stacked in each domain, each with different energies. We trace the lines connecting nodes, as shown by the example for each color in Fig. 5.13. The traced lines are used to create maps of the three strain types plus twist, as shown in Figure 5.14. The values computed in the maps are not meaningful outside the outermost nodes included in the computation (gray dotted boundary in Fig. 5.13), hence we color the external regions gray.

The strain maps in Figure 5.14 record information about the lattices. Firstly, we notice that twist is uniformly the largest component, as expected in a sample known to have a twist angle. We also observe that the region where domains are very elongated has large shear component ($\sim$ 1%) and

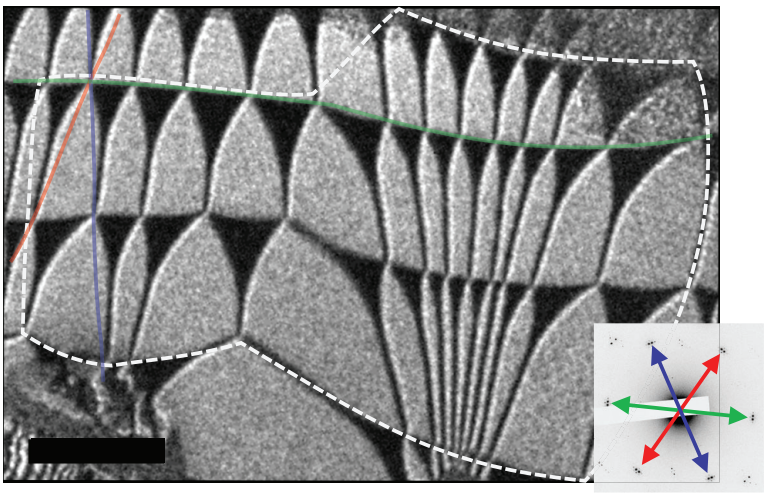

Figure 5.13: First order dark field image of a $WSe_2/MoSe_2$ heterostructure. An example tracing of red, green, and blue line are shown. Gray dotted line outlines the region used for strain map computations. Inset shows diffraction pattern and Burgers vector assignment. Scale bar is 100 nm.

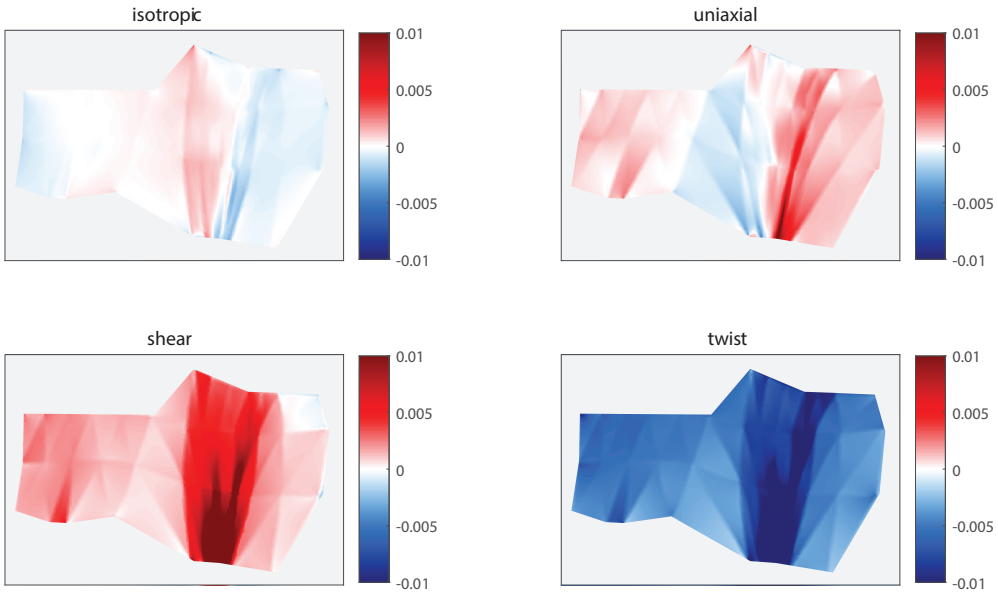

Figure 5.14: Strain maps of the $WSe_2/MoSe_2$ heterostructure shown in Figure 5.13 Units are the dimensionless units of the strain matrix (radians for twist).

some uniaxial strain as well, which is seen to change sign as the domains switch from being slanted to the left to slanted to the right. We also note that the isotropic component is quite small. In fact, it is measured to be less than the intrinsic lattice mismatch of the materials of 0.3%. As this strain mapping technique is simply measuring the discrepancy between the two lattices, intrinsic lattice mismatch should show up in the isotropic component, even if there is zero strain. The low values of isotropic component reveal that there is in fact strain allowing the lattices to globally match to some extent. This can also be concluded from the fact that domains are observed larger than 80 nm, the theoretical largest moiré length for this system assuming lattice mismatch is globally fixed to be 0.3% for WSe_2 and $MoSe_2$.

There are some limits to the level of quantification that can be done with these strain maps. As mentioned above, they only measure heterostrain, the difference in strain between layers 1 and 2. However, it likely suggests the correct order of magnitude of the absolute strain too, in the absense of some globally applied strain distribution that offsets the absolute strain everywhere. Furthermore, a single lattice orientation is used (to determine the Burgers vectors) for the entire strain map, neglecting changes in the individual lattice orientation or scale (stemming from absolute strain) over space.

We remark that the use of Burgers vectors can provide advantages over other strain mapping calculations[73] that can only use the distortions of the moiré cells to compute heterostrain, without knowledge of the underlying lattice orientation. In such cases, assumptions must be made such as picking the lattice orientation that implies the least isotropic strain. Additionally, it is assumed that anisotropic strain components are determined only by anisotropy of the moiré pattern. If both layers are symmetrically strained, pure isotropic or uniaxial strain can produce a rotationally symmetric moiré pattern (see Fig. 5.8). For these reasons, a method including knoweldge of Burgers vectors, such as the one presented here, is advantageous in cases where anisotropic strain may dominate the system, such as in the presence of antivortices.

5.4 Vortex density map

Another interesting map we can create from the shift vector field is the determinant of the displacement gradient matrix. This value is positive at locations of vortices, negative at locations of antivortices, and the magnitude is related to the density of defect nodes (vortices or antivortices).

Antivortices are distinguished from vortices by the chirality of the rotation in configuration space as you make a loop in real space. To quantify this, we can take a real space path from a point ($\vec{x_1}$) to ($\vec{x_1} + \Delta x$) to ($\vec{x_1} + \Delta x + \Delta y$) to ($\vec{x_1} + \Delta y$) back to the start. The corresponding configuration space points are given by Equation 5.3, and will be of the form ($\overline{d}\vec{x_1}$), ($\overline{d}\vec{x_1} + \overline{d}\Delta x$), etc. If the loop in configuration space rotates clockwise it is a vortex, and counterclockwise an antivortex. This is equivalent to asking the sign of the cross product $\overline{d}\vec{\Delta x} \times \overline{d}\vec{\Delta y}$.

Given that Δx and Δy are basis vectors and the matrix

$$\overline{d} = \begin{pmatrix} a & b \\ c & d \end{pmatrix} = \begin{pmatrix} \alpha + \beta & \gamma - \theta \\ \gamma + \theta & \alpha - \beta \end{pmatrix},$$

$\overline{d}\vec{\Delta x} \times \overline{d}\vec{\Delta y} = (ad - cb)\Delta x \Delta y$. Thus the condition for a vortex is $\det[\overline{d}] > 0$ and for antivortex is $\det[\overline{d}] < 0$.

Writing in terms of the strain components, the condition is

$$\operatorname{sgn}[(\alpha^2 + \theta^2) - (\beta^2 + \gamma^2)] = \begin{cases} 1 & \text{vortex} \\ -1 & \text{antivortex.} \end{cases} \tag{5.18}$$

We can think of this equation as a balance between the symmetric components, $(\alpha^2 + \theta^2)$, and the anisotropic components, $(\beta^2 + \gamma^2)$. If anisotropic components dominate, the nodes are antivortices. If they are equally balanced ($\det[\overline{d}] = 0$), we obtain linear, 1D domains.

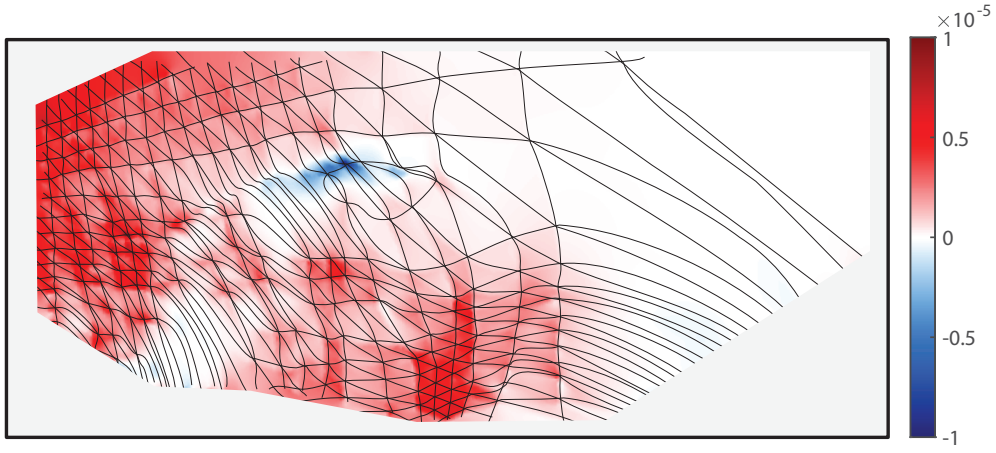

Figure 5.15: Spatial map of determinant of displacement gradient matrix for twisted bilayer graphene containing antivortices.

The magnitude of the determinant is approximately equal to the density of moiré cells, (unit cell area)/(moiré cell area) (see Section C.3), so we will refer to it as the vortex density map.

In Figure 5.15, of a vortex density map, we see negative values along the bubble edge where antivortices are found, and values near zero when domains are very elongated, nearly into 1D stripes. Positive values are found everywhere else, as is normal for a primarily twisted sample.

5.5 Conclusion

We have seen how moiré patterns originate from, and can be used to measure, small amounts of heterostrain, by using the periodicity of the lattice to promote a small scale feature onto a large scale. The moiré pattern that forms is constrained by some topological characteristics.

A topological description of a system cannot depend on the details of the energetics. However, the symmetry of the energy landscape does come into play in determining the shape of the ground state, and thus the topology of the order parameter. In graphene, or any honeycomb lattice with

sublattice symmetry, there is one high energy point (AA) which we remove, and two symmetric ground states with three equally favorable paths between them. This determines the triangle network pattern with six dislocations meeting at nodes. Another system, in which AA is the single, low energy configuration and AB and BA are both high energy, would have two punctures and three dislocations meeting at each node, creating hexagon shaped domains. The topological description of the order parameter space can tell us the type of domain pattern to expect and vice versa.

Furthermore, the topological description of the nodes as a vortex led us to the concept of the antivortex in this system. As antivortices are present in anisotropically strained samples, they can be a way to measure the presence of anisotropic strain, which creates pseudomagnetic field,[74,75] and could have interesting electronic or magnetic properties of their own.

6

Moiré domain ferroelectricity

The symmetries of the underlying lattice determine the possible forms of the moiré domains. Transition metal dichalcogenides (TMDs) have a honeycomb lattice without sublattice symmetry: one sublattice contains metal atoms (M) and the other chalcogens (X). This allows the tunability of certain properties that were fixed in the symmetric case. The two types of stacking, MX and XM, each have a dipole moment due to the different electronegativity of the two atoms. As a

result, MX and XM are not energetically equivalent if they are sitting in an external electric field: the one with dipole moment aligned to the field is favored, and the antialigned one is unfavored. The degeneracy between AB and BA domains in graphene has been replaced by a tunable energy difference between MX and XM domains in the TMD, as electric field is varied. Application of electric field can change the amount of area taken up by the two domains, varying the total polarization of the material.[76,77,78,79,80]

6.1 Observing moiré domain (anti)ferroelectricity

The twisted TMD system can be studied by in situ electrical gating in the TEM while performing dark field imaging (see Section A.3). We employ graphite top and bottom gates, which create the electric field and do not interfere with the dark field imaging as their diffraction spots are offset from the those of the twisted bilayer. We use WSe_2, with $10 - 20$ nm BN and < 10 nm graphite gates. Using first order dark field imaging, the dark (light) domains are seen to increase (decrease) in size with one sign of electric field, and obey the reverse behavior with the other, as in Figure 6.1.

6.2 Quantifying electric susceptibility

We performed a quantitative analysis of the structural change by choosing an order parameter that describes the normalized relative area of the MX and XM domains, $\widetilde{\Delta A} = \frac{A_{MX} - A_{XM}}{A_{MX} + A_{XM}}$. From the TEM data shown in Fig. 6.1, we plot $\widetilde{\Delta A}$ as a function of applied electric field for a few different sized domains (Fig. 6.2). We note that the MX and XM domains each exhibit an intrinsic vertical electric polarization equal in magnitude and opposite in direction, so that the net polarization is varied as the domain ratio $\widetilde{\Delta A}$ varies. Therefore, there is a component of electric susceptibility due to the domain size change, which is directly proportional to the slope of $\widetilde{\Delta A}$ with respect to the out-of-plane electric field ε_z. We use the term domain susceptibility to distinguish it from the mate-

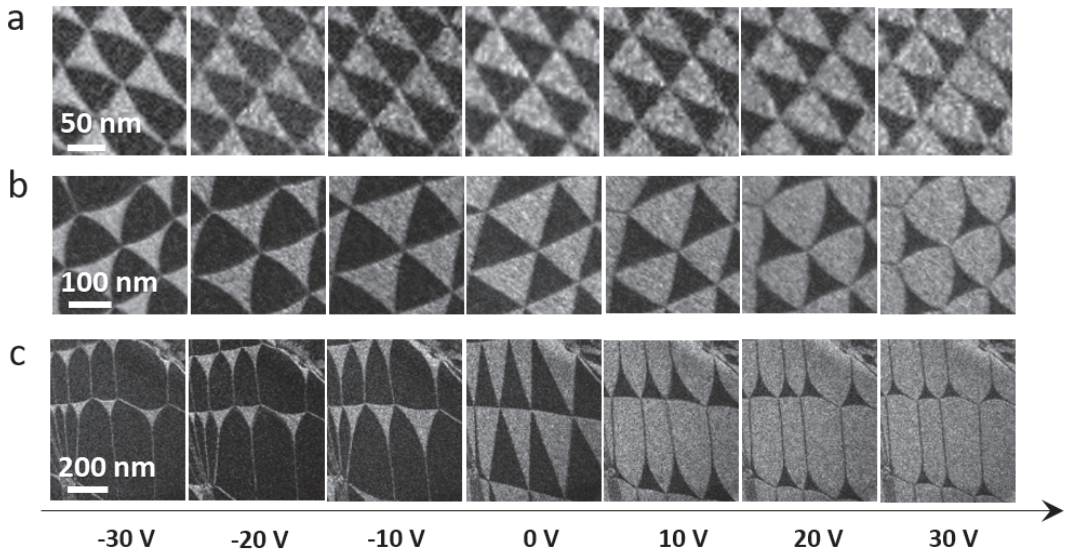

Figure 6.1: TEM dark field images of twisted bilayer TMD plotted as a function of vertical electric field ε_z for different moiré lengths. [Credit Hyobin Yoo]

rial's intrinsic electric susceptibility. Comparing the slopes of each plot obtained from samples with different twist angles (Fig. 6.2), we note that the domain susceptibility of the system is smoothly dependent on the twist angle θ.

We apply an effective model for the total energy of the system to investigate the twist-angle-dependent domain susceptibility of the twisted bilayer TMD. Here, we postulate that the total energy is determined by both the polarization-dependent stacking energy in the domains and the strain energy of the domain walls. As the domain wall changes shape, the increase (decrease) in area of the domain with the favored (unfavored) intrinsic dipole contributes an energy gain, while the increased length of the domain wall contributes an energy cost. The balance of these two effects determines the normalized domain ratio $\widetilde{\Delta A}$ at a given voltage. Under an applied electric field ε_z, the change in stacking energy due to the intrinsic dipole moment, ΔE_{dp} (see Fig. 6.1a as a visual guide),

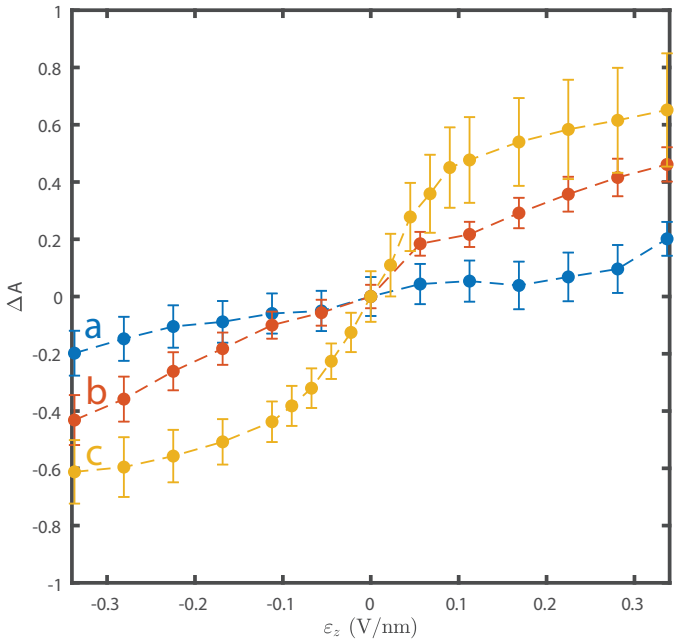

Figure 6.2: The normalized domain area difference ($\widetilde{\Delta A}$) plotted as a function of ε_z for the three different moiré lengths, a, b, and c, shown in Fig. 6.1.

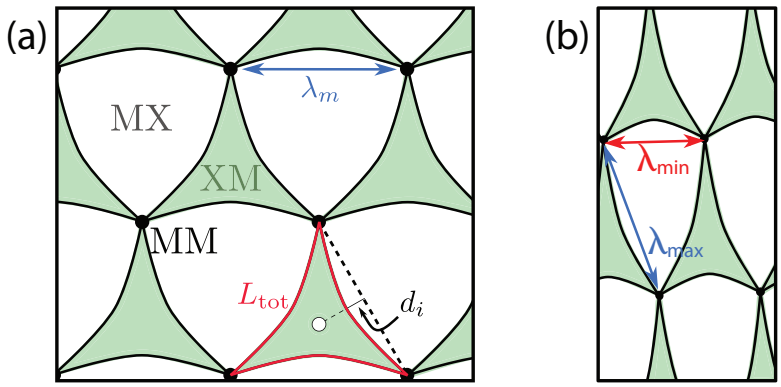

Figure 6.3: Schematics of moiré cell geometry under electric field. (a) When the relative displacement between the top and bottom layer only includes the twist component, the domain structure shows equilateral triangles. (b) When the relative displacement includes the twist as well as anisotropic strain components, the domain structure shows distorted triangular shapes.

is related to $\widetilde{\Delta A}$ by

$$\Delta E_{dp} = \frac{\sqrt{3}}{2\Omega}\lambda_m^2(\widetilde{\Delta A}p_0\varepsilon_z - \chi\varepsilon_z^2) \tag{6.1}$$

where Ω is the area of the atomic unit cell, λ_m is the moiré length (Fig. 6.3), χ is the intrinsic susceptibility, p_0 is the intrinsic dipole moment of MX stacking, and ε_z is the vertical electric field. Assuming the strain energy scales with the length of the domain wall, the change in total strain energy of the system is approximated by

$$\Delta E_{st} = (L_{tot} - L_0)\varepsilon_l \tag{6.2}$$

where L_{tot} is the total length of the domain wall in the moiré supercell (Fig. 6.3), L_0 is the total length of the domain wall at equilibrium ($\widetilde{\Delta A} = 0$), and ε_l is the strain energy per unit length of the domain wall. Optimizing the total energy with respect to $\widetilde{\Delta A}$ yields the approximate relation between the order parameter $\widetilde{\Delta A}$ and the applied electric field:

$$\widetilde{\Delta A} \approx \frac{\lambda_m}{\Omega}\frac{p_0}{\varepsilon_l}\varepsilon_z \tag{6.3}$$

From this equation, we see that the domain susceptibility, which is proportional to $\widetilde{\Delta A}$, scales linearly with the moiré length λ_m, which is consistent with the twist-angle-dependent electric susceptibility observed in Fig. 6.2. Here we note that although our model above implies that the domain susceptibility $p_0(d\widetilde{\Delta A}/d\varepsilon_z)$ is proportional to λ_m, experimental data from our TEM analysis (red marks in Fig. 6.4) do not exhibit a linear relation between $d\widetilde{\Delta A}/d\varepsilon_z$ and λ_m without consideration of the shape of moiré domains.

Further investigation on the corresponding TEM data indicates that the deviation from the linear relation is enhanced when the shape of domains at $\varepsilon_z = 0$ deviates from tha equilateral triangles. As discussed in Chapter 5, the fabricated moiré patterns and domain structures created by the tear-and-stack method [5,6] unintentionally contain anisotropic strain in addition to the displacement

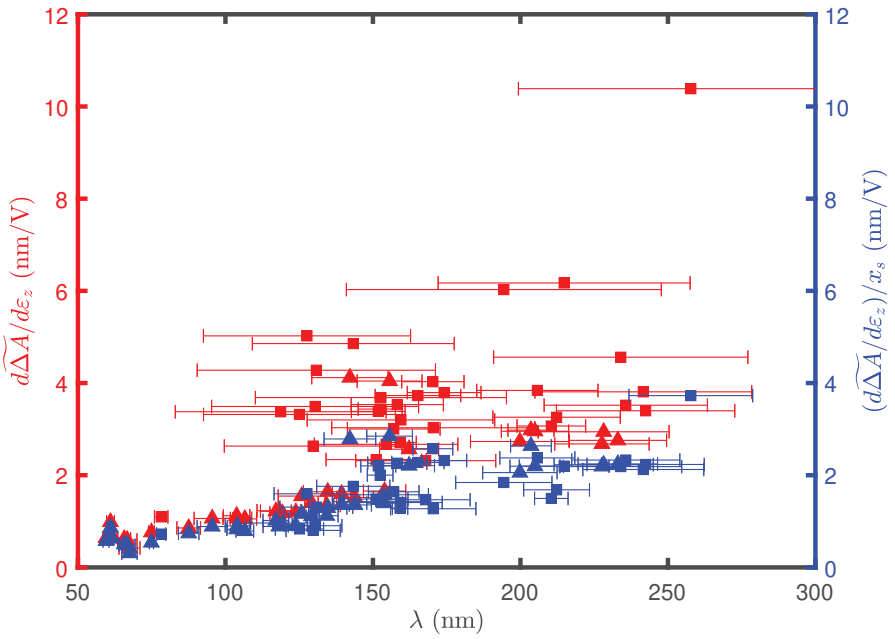

Figure 6.4: Electric susceptibility change with moiré domain size and shape. We plot $d(\widetilde{\Delta A/})d\varepsilon_z$ (red color symbols, left axis) and $x_s^{-1}d(\widetilde{\Delta A/})d\varepsilon_z$ (blue color symbols, right axis) obtained from individual moiré cells as a function of the moiré length λ. Triangle marks represent moiré cells with angles within 30% of the equilateral shape ($x_s \cong 1$). Square marks represent moiré cells that deviate further from the equilateral shape ($x_s \gg 1$). Horizontal error bars represent the spread in values among the four side lengths of each moiré cell.

introduced by the twist angle. Involvement of anisotropic strains induces deviation from the equilateral triangles and forms distorted triangular domain shapes (Fig. 6.3b). From geometrical considerations, we introduce the aspect ratio x_s of a distorted moiré cell, which is defined to be the the ratio of the longest sidelength λ_{max} of the triangle divided by the shortest sidelength λ_{min} (Fig. 6.3) averaged over the two triangular domains. In terms of this quantity, we obtain a revised equation relating $\widetilde{\Delta A}$ and ε_z (see Supplementary Section 3 for details):

$$\widetilde{\Delta A} = \frac{x_s^2}{x_s + 1} \frac{\lambda_m}{\Omega} \frac{p_0}{\varepsilon_l} \varepsilon_z \tag{6.4}$$

According to this equation, which takes into account deviations from the equilateral shape, $d\widetilde{\Delta A}/d\varepsilon_z$ is roughly proportional to the moiré superlattice's aspect ratio x_s. Indeed, linear fits of $\widetilde{\Delta A}$ vs the electric field that showed deviation from the linear relation (red square marks in Fig. 6.4) follow a universal trend with respect to λ_m when we divide $\widetilde{\Delta A}$ by x_s (blue marks in Fig. 6.4). We find values of x_s up to 4, demonstrating that the domain anisotropy is another key factor that determines the domain susceptibility.

The color plot in Fig. 6.5a shows $d\widetilde{\Delta A}/d\varepsilon_z$ as a function of ε_z and $\lambda_m \cdot x_s$. The domain susceptibility increases with $\lambda_m \cdot x_s$ as expected from the revised equation. For both large positive and negative applied electric fields, $d\widetilde{\Delta A}/d\varepsilon_z$ decreases when $\widetilde{\Delta A}$ becomes close to 1, corresponding to the saturation point of the domain susceptibility. In this regime, our simple model no longer applies because the energy of the domain walls can not be accurately described by a simple line-energy as we assumed in the above analysis. The domain walls with different displacements interact with each other resulting in an increase in strain energy when the two adjacent domain walls meet together according to the Frank energy criteria.[81,82] Simulations of the relaxation process using a fully elastic model result in a dependence of $d\widetilde{\Delta A}/d\varepsilon_z$ on $\lambda_m \cdot x_s$ similar to experimental measurements, as shown in Figure 6.5b. The simulations used a dipole-moment of $p_0 = -5.34 \times 10^3 e\text{Å}$ at MX

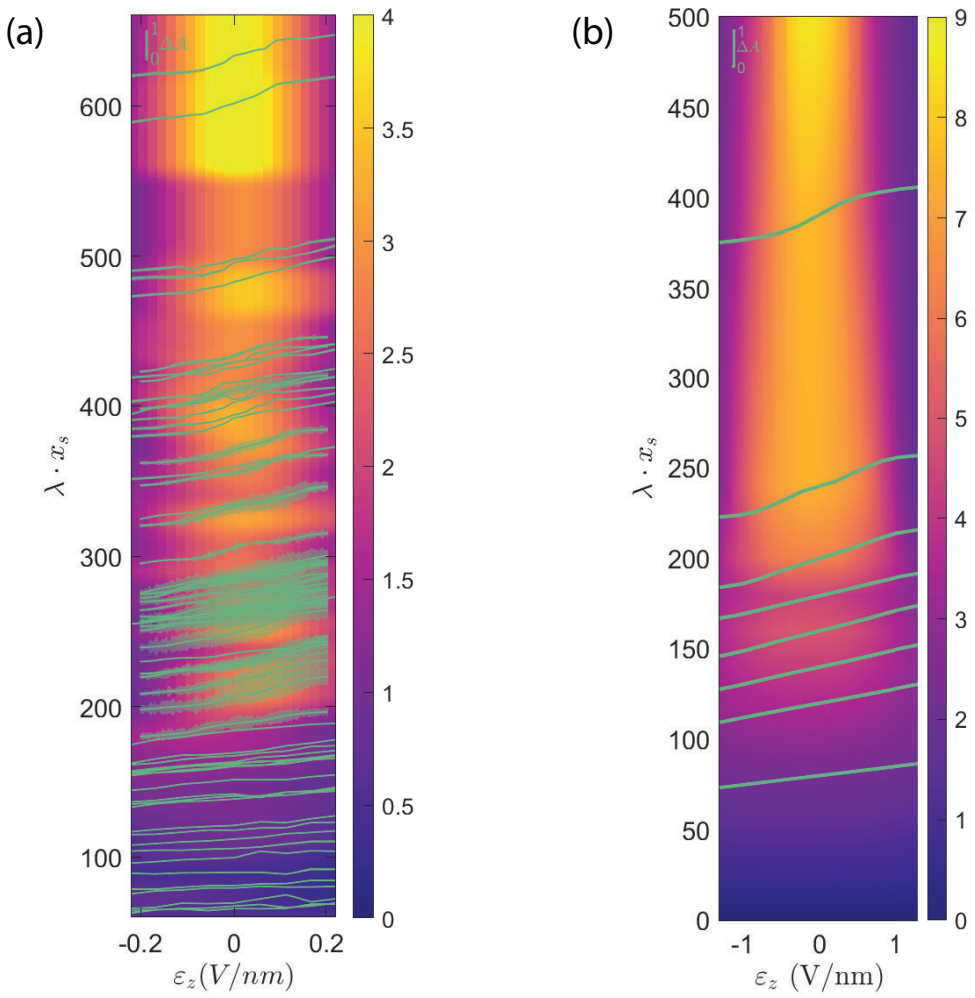

Figure 6.5: (a) Color plot of $d\widetilde{\Delta A}/d\varepsilon_z$ as a function of ε_z and x_s. Green lines are the values of $\widetilde{\Delta A}$ plotted as a function of the vertical electric field ε_z centered at the corresponding value of λx_s. (b) Simulated color plot of $d\widetilde{\Delta A}/d\varepsilon_z$ and lines of $\widetilde{\Delta A}$ vs ε_z at various values of λx_s.

stacking, and a stacking-independent electric susceptibility of $4.18e\text{Å}^2/\text{V}$, obtained from DFT slab calculations. Converting these values to more conventional units requires the area or volume of the bilayer WSe_2 unit cell, yielding $p_0 = -4.3 \times 10^{11} e/cm^2 = -0.895\ \mu\text{C/cm}^2$, and $\chi = 7.1$. We note that although our theoretical model and simulations give excellent qualitative agreement with experimental measurements, the observed domain restructuring is 3 times stronger than predicted. This disagreement is likely caused by inaccuracies in the predicted ε_z values in experiment and the effective p_0 values from the DFT calculations. Both of these terms are very sensitive to the exact electrostatic screening that occurs due to the BN layers and proximity of the metallic gates which is not included in our simple modeling.

6.3 Relation to antiferrolectricity

The structural change in response to the applied electric field observed in our systems shares some similarity with antiferroelectic systems (AFE) in that both systems show no remnant net polarization at zero applied electric fields. Accordingly, we call our experimental observation in the moiré TMD interface a domain antiferroelectric (DAF). However, we note that the constituent up and down polarizations are distributed in different length scales: the polarizations alternate in the atomic length scale[83] for the AFE system while they alternate in the moiré length scale for the DAF system. Upon applying electric fields, furthermore, the DAF behaves in a distinctly different manner compared with the conventional AFE system. In the AFE, a large electric field eventually aligns the electric dipole to the field, turning the system to FE. This electric field induced AFE to FE transition is responsible for the double hysteresis loop that appears in the polarization-electric field relation in an AFE system.[84] In our DAF system realized in a moiré lattice, however, AFE-FE transition was not observed in the sample area populated with multiple moiré domains similar to the sample regions shown in Fig. 6.1.

The absence of a DAF to FE transition in the TMD moiré superlattice can be explained by the topological protection of the domain wall network in DAF. As described in Chapter 5, the domain walls are dislocations that are constrained by the topology of configuration space to meet at MM nodes. Due to the high energy of MM stacking, the nodes as well as the domain walls connecting them cannot be removed from the system with continuous deformation. Due to this topological protection, an applied electric field can deform the domain wall network but cannot convert the DAF into a single FE domain unless domain wall nodes are pushed out of the samples.

6.4 Susceptibility numbers

A single dipole in an electric field will increase its dipole moment with field. Polarizability, α, is the proportionality between a dipole moment p and the electric field E that produced it.

$$p = \alpha E \tag{6.5}$$

When referring not to a single dipole but to a macroscopic piece of material, it is common to consider the dipole moment per unit volume, a.k.a. polarization density P, which is related to electric field by:

$$P = \varepsilon_0 \chi E. \tag{6.6}$$

χ, the electric susceptibility, is related to the dielectric constant ε_r by $\chi = \varepsilon_r - 1$.

In the domain antiferroelectric, the total susceptibility includes a component coming from the polarizability of individual dipoles; we call this the intrinsic susceptibility χ. It also includes a component coming from the domain ratio changing, proportional to $\widetilde{\Delta A}$; we call this the domain susceptibility, χ_d. We can compute χ_d for a given material, and compare to χ to see whether domain susceptibility is an efficient way of tuning measurable properties in that material.

The total dipole moment due to domain ratio in a region of area A is

$$p = p_0 \frac{A_{MX}}{\Omega} - p_0 \frac{A_{XM}}{\Omega} = p_0 (\widetilde{\Delta A}) \frac{A}{\Omega} \tag{6.7}$$

where Ω is the area of a unit cell and $p_0 = -5.34 \times 10^3 e\text{Å}$ is the dipole moment of a single MX-stacked pair of atoms (there is one per unit cell). To convert this to a domain polarization density, P_d, we divide by the volume of the material, Al, where l is the thickness of the bilayer. Thus,

$$P_d = \frac{p_0}{v} \widetilde{\Delta A} \tag{6.8}$$

where $v = \Omega l$ is the volume of a unit cell. By Equation 6.4, $\widetilde{\Delta A}$ is proportional to electric field, allowing us to calculate an effective susceptibility of the domain effect.

$$\widetilde{\Delta A} = x_s \lambda_m \alpha_d E \tag{6.9}$$

where in this system α_d is empirically about $0.01\ \text{V}^{-1}$ from the slope of Figure 6.4. So,

$$\chi_d = P_d/(\varepsilon_0 E) = (0.895 \mu\text{C/cm}^2) x_s \lambda_m 0.01 V^{-1}/\varepsilon_0 = 0.01 x_s \cdot \lambda \tag{6.10}$$

where λ is the moiré length in nanometers. In this experiment we observed $x_s \cdot \lambda$ approximately in the range of $50 - 650$, corresponding to $0.5 < \chi_d < 6.5$. As the intrinsic susceptibility of WSe_2 is 7.1, the domain susceptibility, especially for large domains (small twist angle), is measurable relative to the background of ordinary polarization, with for instance, a capacitance measurement.

In addition to tuning the susceptibility, twist angle can bring us to different types of electric response. In Chapter 2, we noted that there is an important structural cross-over at the crossover angle, θ_c. A twisted bilayer system with twist angle larger than θ_c exhibits moiré structures with a

negligible amount of structural reconstruction. In this regime, the system would exhibit normal dielectric properties in the macro scale, and we do not observe significant structural change upon applying electric field. On the other hand, moiré domain antiferroelectricity is developed in $\theta < \theta_c$ as alternating domains with opposite polarizations are formed. Furthermore, as we decrease the twist angle, we reach another important transition angle, θ_t, that appears where the resulting moiré length scale (domain size) becomes larger than the sample size. In this regime, the topological domain wall networks disappear, and we observe switchable polar domain dynamics, like a ferroelectric material, indicating the possibility of polarity engineering via twist angle control.

7

Twisted multilayers

Adding a third twisted layer into the stack creates a situation where two moiré patterns coexist with each other, one from each interface. Twisted multilayers can have interesting transport properties, such as magic angles at higher twist angles. They also introduce many new possible structures. An N-layer twisted stack must be defined by $N - 1$ twist angles or shift vectors. If θ_1 is the angle between the first and second layer and θ_2 the angle between the second and third layer, systems

where θ_1 and θ_2 have the same or opposite sign, or similar or different magnitudes, are qualitatively different.

7.1 Trilayer continuous twist

When three graphene layers are twisted relative to each other, the moiré patterns at the two interfaces now have a moiré pattern forming between them, known as the moiré-of-moiré (MoM).[85] This is clearest when θ_1 and θ_2 have the same sign. Each moiré length scale is approximately given by $L_M = a/\theta$, (where a is the lattice constant), so if $\theta_1 = \theta_2 = \theta$, the MoM length is $L_{MoM} = a/\theta^2$. The moiré of moiré system can be used to obtain flat bands and superconductivity.[86]

While the angles used in transport experiments were in the range around $2^\circ - 3^\circ$, we study the structures in TEM of twisted trilayer with smaller angles, in the range of $0.5^\circ - 1^\circ$, in which domain formation occurs.

7.1.1 Big and small triangles

One type of feature we observe is small triangles within larger triangles. This dark field TEM image does not demonstrate moiré of moiré, as the large triangles are most likely coming from a smaller twist angle in one of the interfaces, rather than the interference of the two moiré patterns. We observe these features at a series of tilt angles (Figure 7.1), in order to obtain information about the three layer stacking order.

In naturally forming bulk graphite, the stacking order is ABAB..., known as the hexagonally close packed structure. The rhombohedral structure, ABCABC..., is slightly higher in energy.[87] Similarly, in trilayer, ABA stacking is slightly favored over ABC.[88] With two overlapping moiré patterns in a twisted trilayer, the structure would have to go through other stackings as well such as AAB-type of stacking. Each of these types of stacking symmetry should respond differently in dark field to tilt. In

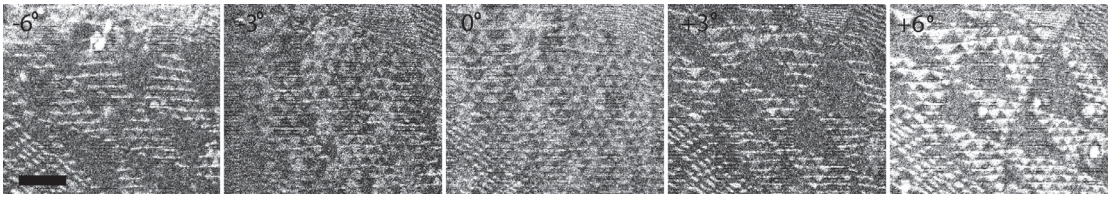

Figure 7.1: First order dark field of a region of twisted trilayer at different tilts: -6°, -3°, 0°, 3°, 6° from left to right. Varying contrast small triangles within large triangles are visible. Scale bar is 200 nm.

Figure 7.1, we see that the four types of domains (two types of small triangles in each of two types of large triangles) follow various trends in intensity over tilt.

Brown et al[25] calculate the intensity as a function of twist for AB, BA, ABC, and ABA type stackings. Here, we do similar calculations but extend them to include AAB-type stacking as well as general tilt. In TEM, the primary tilt axis of the holder is known as α tilt. Double tilt holders can also tilt in the complementary axis, known as β tilt. For this computation, we vary α tilt, while including a parameter to introduce a fixed β tilt, to mimic experiments where only α tilt is varied, but a fixed β tilt $\lesssim 2°$ could be present due to the sample not being perfectly flat. Further, we include a parameter θ_p to vary the relative orientation of the diffraction pattern relative to the α tilt axis, to be able to match experiments where the α tilt axis is fixed in the microscope, but the orientation of diffraction peaks depends on the sample. Figure 7.2 shows a schematic of these parameters. Additional detail about multilayer, tilted structure factor calculations is included in Section C.4.

In Figure 7.3 we present structure factor calculations for three stacking types vs α tilt for the diffraction peaks labeled as b_1 and b_2 in Figure 7.2. Diffraction peak b_2 is the one used to create the dark field images in Figure 7.1. An angle θ_p of 25° is used, to match to the experimental conditions in Figure 7.1. Measurement of the intensity in each small domain at a range of different tilts could allow the stacking type to be identified, by observing whether the intensity is at a local maximum, minimum, or neither at 0° tilt. We also simulate the effect of a nonzero tilt in the β tilt axis. In Figure 7.4, we see that a fixed β tilt can cause the intensity curves to shift, reaching their peak or

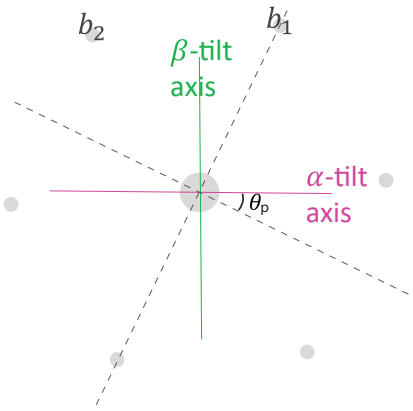

Figure 7.2: Schematic diffraction pattern of graphene showing first order diffraction spots. Spots 1 and 2 are labeled. An angle θ_p is defined between the α tilt axis and the orientation of the diffraction pattern.

minimum at nonzero α tilt. Under the parameters in this example, the effect is negligible for b_2.

7.1.2 Flowers

In other regions, the triangle domains in the two interfaces are much closer to the same length scale. Sometimes, the resulting patterns look like that shown in Figure 7.5, in which domains like six petals of a flower emanate from a central domain. By tracing the domain walls from second order dark field, two sets of lines appear in each color, at two different angle orientations. This is consistent with two domain patterns coming from two different interfaces, with a relative twist angle between the two moiré patterns. In Figure 7.6, we overlap triangle domain patterns, one blue and one orange, with a relative twist between them. Similar structures to the flowers appear whenever AA nodes in both the orange pattern and the blue pattern coincide. It would be interesting to investigate whether there are energetic factors that drive the AA nodes to match up with each other.

The pattern in Figure 7.6 is an incommensurate overlap of two domain patterns, with a moiré periodicity of its own. A domain pattern is by nature produced by a moiré pattern, so the flower

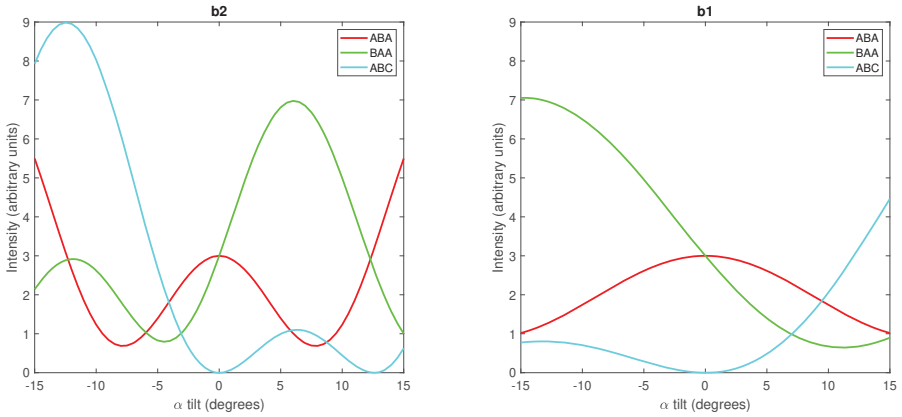

Figure 7.3: Structure factors are computed as a function of α tilt for three different stackings, with the α tilt axis oriented at $\theta_p = 25°$ relative to the diffraction pattern, and β tilt of 0°. The diffraction positions b_1 and b_2 are as defined in Figure 7.2.

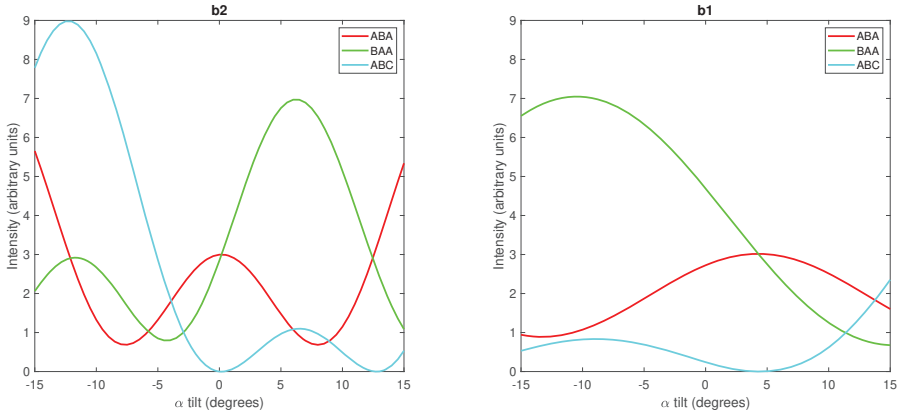

Figure 7.4: Structure factors are computed as a function of α tilt for three different stackings, with the α tilt axis oriented at $\theta_p = 25°$, and β tilt of 2°. For diffraction spot b_1, the curves are significantly shifted relative to those in Figure 7.3.

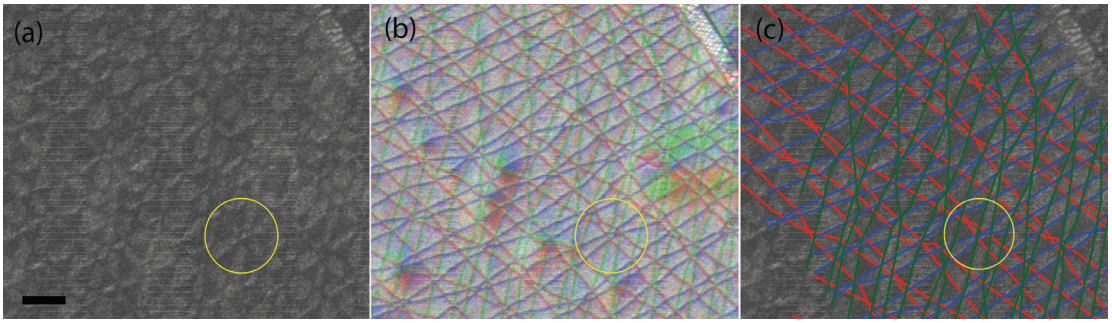

Figure 7.5: "Flower" pattern in twisted trilayer; one flower is circled in yellow in each image. (a) first order dark field, showing sixfold radial flower-like arrangements of domains. (b) second order dark field, showing overlapping domain networks from both interfaces. (c) tracing of domain walls overlaid onto first order image, showing contrast switches at domain walls. Flowers consist of places where AA nodes in the two networks coincide. Scale bar is 100 nm.

pattern in a graphene sample can likely be considered moiré of moiré.

7.2 Trilayer alternating twist

Rather than twisting subsequent layers further in the same direction, an alternative is to twist the third layer back into alignment with the first layer. This results in a structure that can be thought of as a superposition of a magic angle bilayer (with magic angle increased to 1.53°) and a monolayer.[89] The flat band condition has been used to achieve superconductivity.[90,91]

As we know from TEM of twisted bilayers, it is unlikely that the first and third layer are exactly aligned, and thus, we expect them to produce a large scale moiré pattern. A composite image from second order dark field is shown in Figure 7.7. Domains on a length scale around $100 - 200$ nm are seen, implying a twist angle around 0.2°. The domains are shaped like hexagons (one is outlined in pink in Fig. 7.7), though they are rather asymmetric. The hexagon shape, as well as the dark field conditions in which domain wall contrast appears or disappears, indicate that the transition between adjacent domains are perfect dislocations, i.e. the Burgers vector is a full unit cell vector of the lattice. This is in contrast to AB-BA domains in twisted bilayer, in which the Burgers vector is a fraction of a unit cell vector. Because perfect dislocations imply the same stacking order in every do-

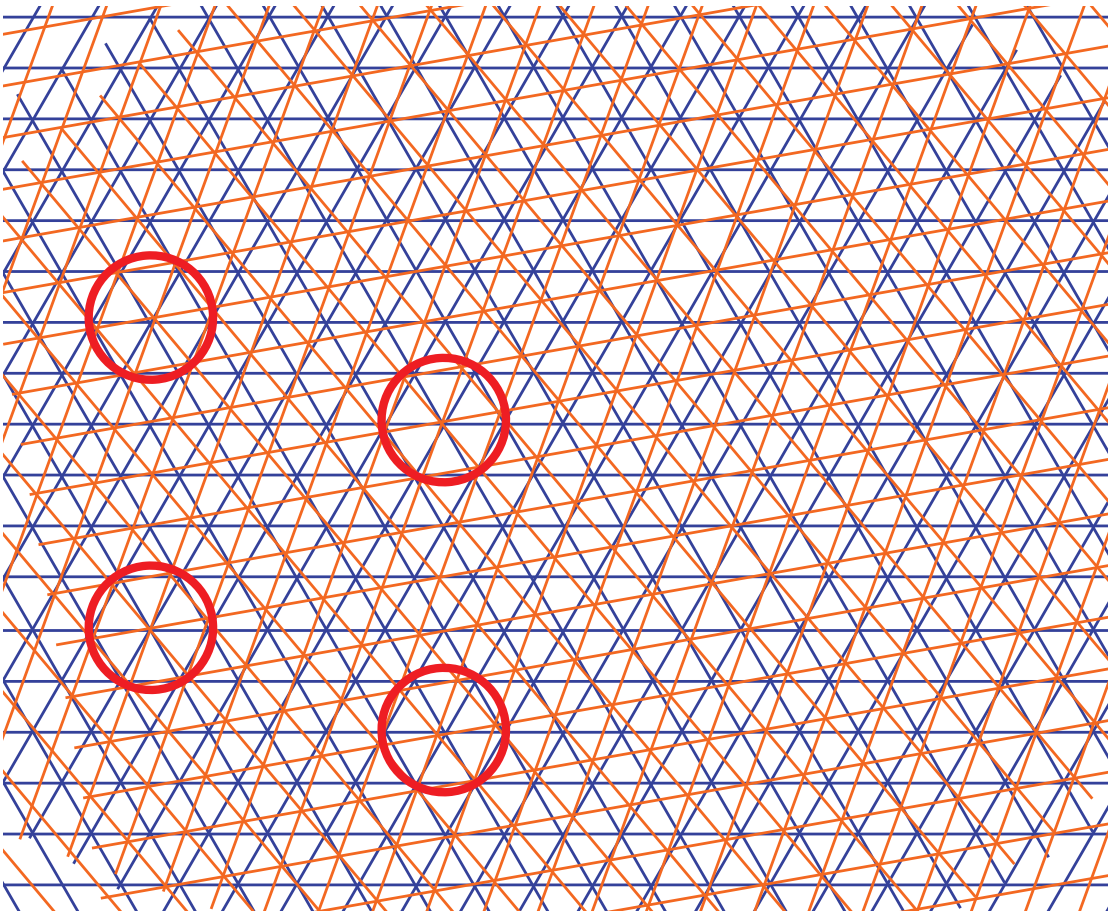

Figure 7.6: Overlap of two sixfold networks with a relative twist angle produces a moiré of moiré pattern. Features similar to those in Fig. 7.5 are visible. A few "flowers" are circled in red.

main, and AA is unique whereas AB and BA are degenerate, the stacking order between the top and bottom layers is most likely AA. Since there is a middle layer in between it is known as "A-twist-A" or AtA.

The middle layer is evident in small moiré fringes with a period around 10 nm that are visible in the interior of the large domains. The period implies a twist angle around 1.5° relative to the top and bottom layers.

In devices, the twist angle in the trilayer region is observed to be approximately the average of the twist angle between top and middle and middle and bottom, measured separately outside the trilayer region. The TEM images of domains thus support strong lattice relaxation in this system. Rather than somehow globally locking into a single average angle, the structure relaxes into domains that at their interior contain the average angle. This is consistent with the STM observations of Turkel et al,[70] in which a large-scale moiré length is visible in addition to the small moiré length from the middle layer. However, the boundaries of hexagon-shaped cells are not visible in the STM.

7.3 Quadrilayer alternating twist

The alternating twist concept can be generalized to any number of layers. For instance, with four layers a magic angle condition is attained when the second and fourth layer are at 1.75° relative to the first and third layer.[92] In this case there are two pairs of closely aligned layers, that can each have domains forming.

Dark field imaging of the quadrilayer shows three moiré length scales. The largest length scale, 100 nm, implies a twist angle of $0.1 - 0.2°$, and forms visible hexagon-shaped domains. These domain walls are perfect dislocations, as evident from the fact that the invisible contrast condition is found at first order, implying their Burgers vectors are full lattice vectors. Additionally, the fact that they are hexagonal implies that there is only one domain type, consistent with perfect dislocations.

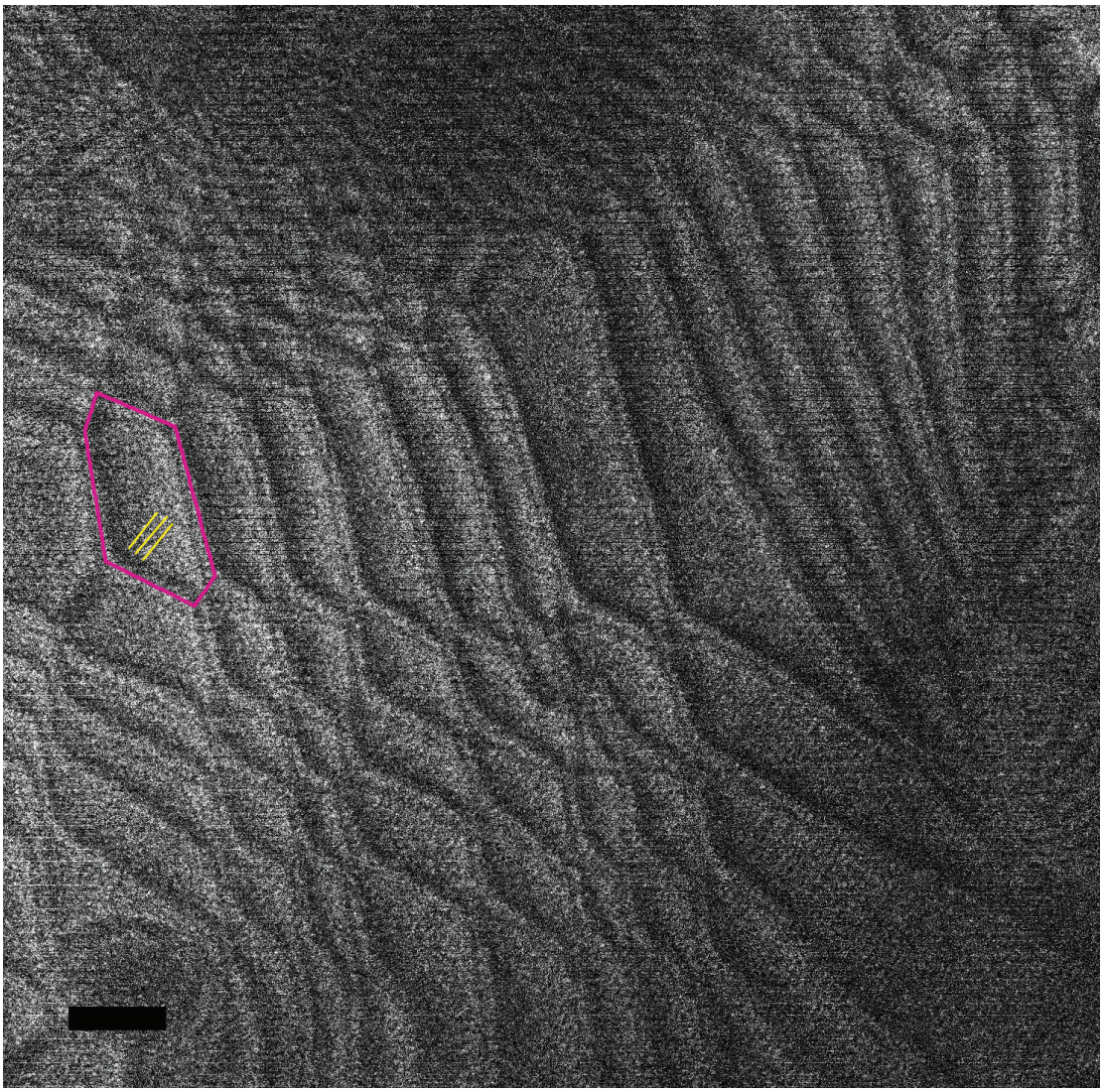

Figure 7.7: Hexagon domains visible in alternating twist trilayer, implying AtA stacking. Small fringes on the 10 nm scale (highlighted in yellow) come from the middle twisted layer. One hexagon is outlined in pink. Scale bar is 100 nm.

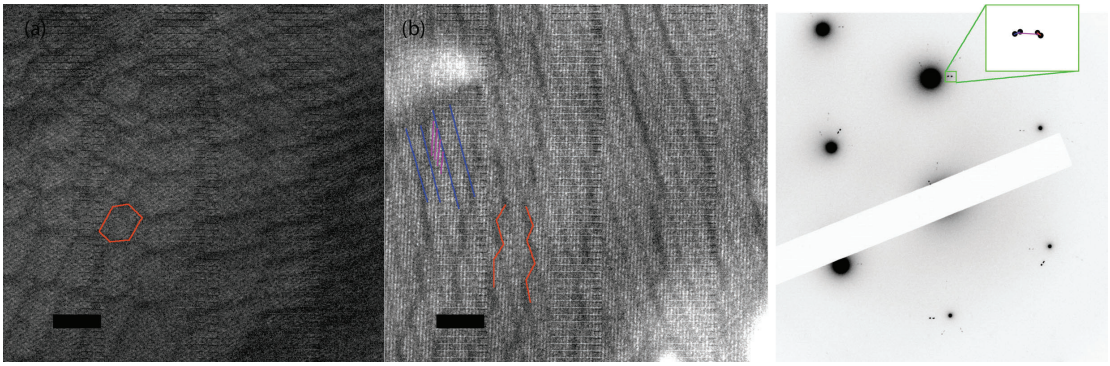

Figure 7.8: Three moiré lengths visible in alternating twist quadrilayer. Scale bar is 100 nm. (a) composite of three first-order dark field images, showing ∼100 nm hexagon domains (e.g. outlined in orange). (b) a single first order dark field image from the same region, showing three sizes of moiré lengths. Large (∼ 100 nm, orange), medium (∼ 30 nm, blue), and small (∼ 7 nm, purple). Green box in diffraction pattern highlights spot used for image in (b). A schematic of the arrangement of peaks is inset. Small (purple) fringes must come from the separation between the two closely spaced peaks, and orange and blue each from a pair of close-spaced peaks.

Like in trilayer, this implies AtA stacking. In Figure 7.8a, a composite of three first order images demonstrates the hexagonal shape of the domains. Figure 7.8b is a single first order image, in which three moiré scales are visible. The largest, highlighted in orange, are the domains visible in the composite image. The medium length scale, $\sim$ 30 nm, implies a twist angle of 0.4°, and is presumably the twist between the other pair of closely aligned layers. The smallest length scale $\sim 7 - 8$ nm, implies a twist angle of about $1.7 - 1.9°$, and must come from the twist angle imposed between alternate layers. Likely the medium length scale also consists of hexagonal domains, but it is less clear to see them with so many things going on in the image. We can also observe that the domain walls of the large moiré length and those of the medium moiré length often overlap, implying that the domain patterns of both interfaces tend to align with each other.

7.4 Outlook

Twisted multilayer graphene offers a productive new source of magic angle systems, that are potentially more robust to twist angle disorder. TEM studies of these systems are, however, more

complicated than of bilayers, as the structure at each interface is overlapped into a single image. Nonetheless, dark field methods can be successfully extended to multilayers. In order to determine the trilayer stacking order, intensity can be tracked versus tilt and compared to simulations. Imaging of dislocations still reveals domain boundaries but it is not always clear which interface the dislocations are coming from.

In the alternating twist system, the formation of domains between the closely aligned layers explains how only a single angle is present to influence transport, as the interior of the domains contains a commensurate stacking of the two layers. It also reveals the presence of dislocation lines in the top and bottom layer, whose influence on transport and superconductivity is currently unknown. We have also observed that AtA is likely the dominant structure. These observations can inform theory and experimental directions in the system.

In the continuing twist trilayer, moiré of moiré domains are yet to be identified. While neither clear domain contrast nor domain walls on the scale of the moiré of moiré length have been observed, the relaxation seems to observably occur on the scale of the individual moiré patterns. However, domain patterns such as "flower" arrangements were observed that involve the interference and alignment of the two moiré patterns. these flower-shaped patterns suggest there may be a favorability for AA nodes of each interface to overlap with each other. As AA nodes in the bilayer have high density of states, such features in the trilayer could create an electronic landscape that influences the transport in the system.

The investigation of moiré structures in multilayers is just beginning, and there is much to explore in both TEM and transport.

8

Conclusion

There are so many possibilities in the interfaces of nearly aligned van der Waals heterostructures. In a 2013 review article,[93] Geim and Grigorieva wrote about the "dreamscape" of van der Waals heterostructures, wherein stacking different 2D materials on each other in thoughtful combinations could produce all sorts of material properties, from high temperature superconductivity and superfluidity to optical properties and continuation of Moore's Law. Only one paragraph in

the article covers the importance of "crystallographic alignment" and moiré patterns at the interface. Since then, the relevance and number of different systems that utilize moiré interfaces has snowballed, creating a dreamscape of possibilities of its own.

In this thesis, I have explored some of the many parameters that influence the structure and properties of the moiré pattern.

Firstly, there's the type of mismatch itself. In addition to twist, changing the shape of the lattice cells either through strain or intrinsic lattice mismatch, produces its own kind of moiré patterns. Strain engineering, via substrate or applied strain, can allow us to create domain patterns of different topological classification.

The symmetries of the materials used are also crucial. Graphene, with carbon on every site, is stuck with certain symmetries that can be removed by working with other materials. Any material with different A- and B-site atoms (e.g. BN or the TMDs), can break the symmetry between AB and BA domains, such as in the domain antiferroelectricity experiments. We could further increase the array of moiré systems by using materials with different lattice structure. Square lattices, anisotropic lattices such as in black phosphorus, or even putting together two materials with different lattice symmetries, would produce new types of moiré patterns with different connectivities of the domain network.

We can also alter the domain pattern by including additional layers. In graphene, the presence of a third layer can alter the energetics of which domains are favored. Inserting a monolayer of BN between a moiré interface can also adjust the energetics while still allowing domain formation between top and bottom layer.

The shape and periodicity of the moiré pattern affects the electronic structure by introduction of a periodic superlattice. But the formation of domains further affects material properties. We have seen that the domain structure is relevant to the 1D network of topological states in small-angle twisted bilayer graphene, as well as influencing the electronic structure at the magic angle. As new

magic angle systems are realized, such as alternating twist trilayers and multilayers, understanding domain structure between the small-angle interfaces also becomes important.

We have made use of tools that allowed us to elucidate material properties in a range of systems, and that can be applied to future varieties of moiré systems. Topological analysis of configuration space can form the backbone for understanding a given moiré structure. Image processing of the dark field images can give quantitative information such as strain maps, domain areas, and dark field image intensities, which can reveal structural order parameters of the system.

Moiré patterns are realizing materials design in a new way, and twist is only the tip of the iceberg.

A

TEM techniques

This appendix contains experimental procedures for TEM imaging and sample preparation techniques used throughout the work.

A.1 Dark field imaging

Dark Field images in this work were collected on a JEOL 2010F TEM with Gatan OneView camera. After performing standard alignment, sample is brought to a magnification in the approximate

range of 8kx-20kx. The process of setting up the dark field imaging is most conveniently done directly on the microscope's phosphor screen, not on the computer. A selected area aperture (SAA) is inserted on the region of interest, and microscope is put into diffraction mode, with camera length around 50 – 60cm. Diffraction pattern is focused, and the smallest objective aperture is inserted and centered around the central (transmitted) beam. On the 2010F microscope, the smallest objective aperture is 5 μm. Then, the microscope is returned to real space imaging (MAG1 on the JEOL microscope), and SAA removed, in order to set an appropriate brightness (i.e. beam spread).

Back to real space, there is probably only a very faint illuminated region on the screen. Adjust the brightness, and a bright dot should start to grow. This is the image of the transmitted beam. Keep the bright circle in the illuminated region by adjusting the position of the objective aperture. There is an optimal brightness value such that the bright spot from the transmitted beam takes up the entirety of the illuminated region. This is the brightness value that will be used for dark field imaging. If possible, do not change the brightness throughout imaging, or else this step will need to be repeated. Now that the brightness has been changed, the diffraction pattern is no longer in focus. Return to diffraction imaging and adjust diffraction focus. This can be done with or without removing the objective aperture.

Once the brightness and diffraction focus have been set, it is possible to form filtered images. By leaving the objective aperture around the transmitted beam, one can perform bright field imaging. Centering the aperture on a diffracted beam will create dark field images. There are two ways to do so: (1) physically moving the objective aperture, or (2) adjusting the "dark tilt" to tilt the diffracted spot into the center. The 2010F conveniently has the ability to save five dark tilt settings, such that one can easily switch between several dark field imaging conditions without readjusting any apertures or tuning any knobs.

When the desired diffraction spot is centered in the aperture and the microscope has been returned to real space mode, a dark field image is now on the screen. However, it is likely too dim to

resolve any detail on the phosphor screen. Bring the image up on the computer screen and adjust exposure time to see if image contrast is visible. If a dark field image is visible but does not fill the illuminated area, it is probably necessary to adjust the centering of the objective aperture, by adjusting the aperture position or (preferably) tuning the dark tilt knobs, while watching the image on-screen to reach the optimal condition. If using the preset dark tilt settings, different dark field images can be taken at the same spot right in row without changing any other settings, simply by selecting the relevant dark tilt setting and then capturing an image.

A.2 Sample preparation: TEM grids

Interfacing 2D materials with TEM means adapting fabrication methods for 2D materials to TEM-compatible substrates. Here I will record the methods I have learned and consolidated, for posterity.

For substrates, we use SiN membrane windows. Our most standard choice is 50 nm-thick membranes, on 200 μm-thick silicon frames. For graphene dark field imaging, this is too thick to get enough contrast to get decent images, so we etch the backside of the membrane to reach 30 nm membranes. (I typically do this after putting down the stack but before removing PC, so the PC acts as a protective layer over the top of the membrane.) We can also put graphene on 20 nm or 10 nm membranes, or suspend it over a hole in a membrane to get better image contrast. To be TEM compatible, square chips should have sidelength about 2.1 mm. Circular chips should be 3 mm diameter.

The most convenient option is to use membrane frame arrays, in which multiple SiN membrane chips (about 4x4) are attached in a grid, with cleave lines etched in the silicon frame so they can be cleaved apart. These can be made from a SiN-coated wafer via photolithography and etching, or purchased. The larger size of the arrays, compared to a single TEM grid, is useful for fabrication steps that require attaching to a vacuum chuck, as well as improving ease of handling.

If one cannot use a membrane array, it is possible to glue a chip to a regular silicon chip using PMMA. Then the larger silicon chip can be attached to vacuum chucks. To do this, spincoat a chip with PMMA 495 for about 3 seconds at about 2000 rpm, then immediately place the TEM chip onto the wet surface of the silicon chip. The goal is to get a PMMA layer thin enough that it doesn't flow onto the top surface of the TEM chip, but thick enough that it adheres to the sides of the chip. Then, heat at 180°C for about 30 seconds (as short as possible while still allowing it to fully dry, to avoid deactivating the O_2 plasma) to dry the film.

A.2.1 Putting stacks on membranes

Stacks of van der Waals materials made in a normal dry-transfer process (I use poly bisphenol-A carbonate (PC) for most purposes) can be put down on SiN membranes. However, there are a few extra considerations in order not to break the membrane.

- Do not tilt the transfer slide so as not to place extra pressure on the membrane from downward force. (It is fine to do previous steps with tilt).
- Limit the amount of downward motion of the transfer slide once they come in contact. Do most of the contact with heating.
- Do an Oxygen Plasma process on the membrane immediately before transfer. This increases the adhesion to the membrane by making it more hydrophilic.[94] A typical recipe is 5 minutes at 150 W with 40 sccm of O_2, about 470 mTorr. Note that the effects will wear away in about 30 minutes, and heating undoes the effect as well. However, it is most important that the membrane is not hydrophobic, even if it isn't as hydrophilic.
- The biggest indication of whether the stack will or won't stick to the membrane is whether it curves up or down. If the PC advances ahead on the membrane compared to where it is on

the rest of the chip, that is a sign of good adhesion. If the PC hangs back on the membrane while advancing on the rest of the chip, because it is too hydophobic, or the membrane is pulled down (e.g. by the vacuum chuck), it is likely the stack will wash off in solvent.

A.2.2 Removing a stack from a membrane

One may want to characterize a van der Waals stack (twist angle, domain pattern) using TEM, and then transfer the stack to different substrate for use in a device. To do this, one must first secure the TEM-sized chip to the transfer stage. I use the PMMA gluing method, described above. Then, I use poly-bisphenol-A carbonate (PC) film on PDMS as a transfer stamp. After bringing the PC into contact with the stack, I heat to 120°C, which is higher than standard pick up temperature, but below the melting temperature of PC. It is best to keep the PC from advancing to cover the entire membrane, to minimize the chance of tearing the membrane up with the stack. I then pick up the PC at 120°, and the stack should come with it.

There are some limitations of this process. One concern is the possibility of the structure changing during the transfer. To get a sense of this, I transferred a stack off a membrane after TEM, then onto another membrane and imaged again. Bubbles in the stack appear in the same positions after the transfer (Fig. A.1), indicating that the structure did not change significantly. Angle measurements via SAED in approximately equivalent locations resulted in the values in Table A.1. These measurements indicate that the twist angle is not changing substantially when a stack is transferred to a different substrate by this method.

Table A.1: Angle measurements before and after transferring stack to a new substrate.

Location	Position 1	Position 2
Before	29.6°	29.2°
After	29.4°	29.2°

The other concern is TEM-induced damage[95]. One type of TEM damage is knock on damage, in

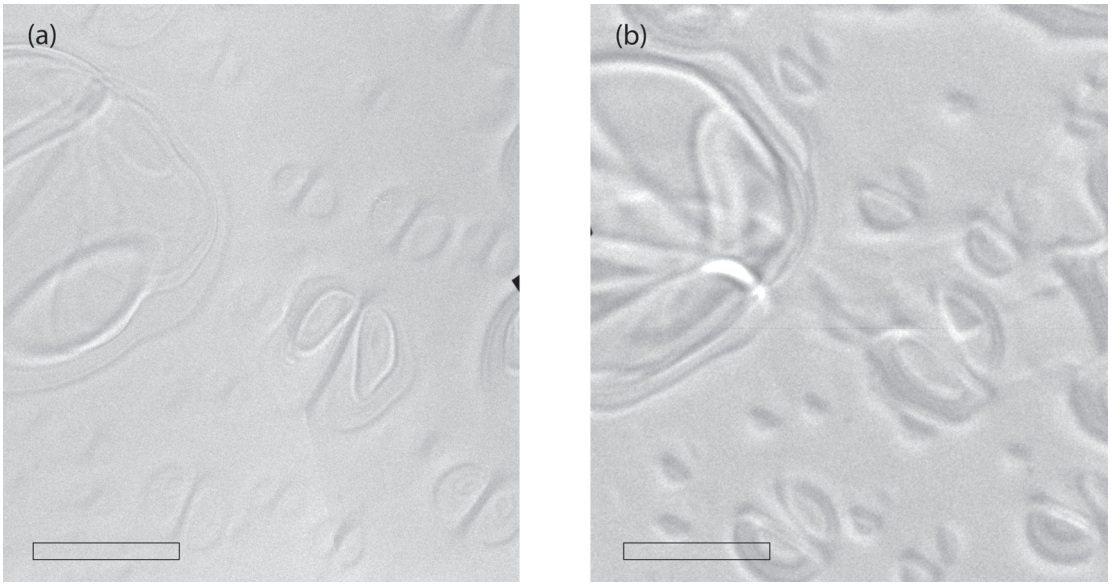

Figure A.1: TEM bright field of 30° stack (a) before and (b) after transferring to a new substrate. Bubbles can be seen to occupy the same positions before and after. Scale bar is 1 μm.

which the kinetic energy of the electrons can knock an atom of a given mass out of the lattice. Most of our imaging is done at 80 kV, which is below the threshold of knock-on damage for carbon, of 84 kV, so this is not likely an issue. Another type of beam induced damage is heating effects, from inelastic scattering of the electrons.

In our experience, optical signal such as Photoluminescence and possibly Raman spectroscopy, appeared attenuated after TEM imaging had been performed. This may be due to inelastic damage, deposition of carbon contamination during the TEM, or something else. As a result, we prefer to do optical studies prior to TEM studies, if possible.

It is unclear exactly how beam induced damage effects transport. Devices measured in transport after TEM had decent quality. While not the best quality possible, it is hard to know if TEM or other factors determined that.

A.3 In-situ imaging

In-situ imaging was performed using a Gatan helium double tilt holder (HCHDT3010), with 5 electrical feedthroughs. Custom bond pads were added to the holder tip, close enough to the sample to enable wirebonding. During insertion of the holder into the TEM, the electrical ground was connected to the microscope column, so that a possible touch of the wires to the inside of the TEM would by detected, by activating the microscope's stage limit alarm. DC voltage up to 30 V was applied using a Keithley 2400 source meter, to create electric field in the sample during imaging and video recording.

B

Supplementary data

This appendix contains additional supporting data to the chapters.

B.1 Supplementary data to chapter 2

Figure B.1 contains fractional intensity data for six types of satellite peaks, including the three types shown in Figure 2.5 as well as three others. Similar exponential decay rate is observed for all of them.

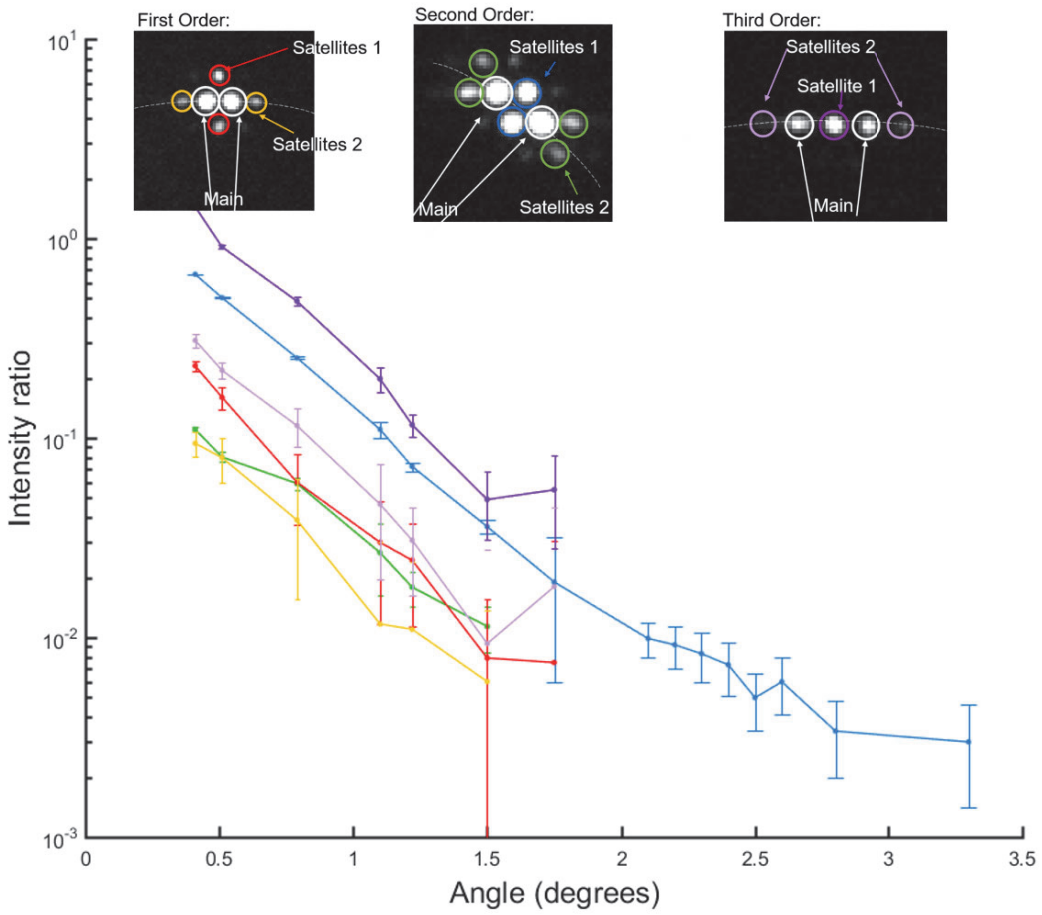

Figure B.1: Satellite peak intensity as a fraction of Bragg peak intensity for six types of satellite peaks. Insets show types of satellite peaks, circled by color corresponding to traces on the plot.

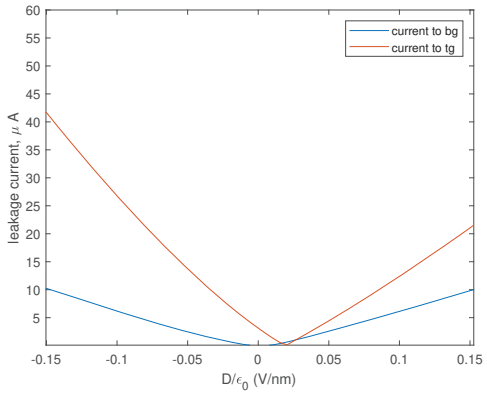

Figure B.2: Current from device to gates as a function of D field. Source-drain current is 100 nA.

B.2 Supplementary data to chapter 3

The device measured in chapter 3 proved to have very high leakage current (fig. B.2). Furthermore, resonance-like features appeared that varied with magnetic field and both gates (fig B.3), and do not respect Onsager reciprocity.[96] Fig. B.4 demonstrates some 4-terminal measurements that should be Onsager pairs. Floating both gates recovers the Onsager relations, implying that the gate leakage is responsible for the device behavior (Figure B.5).

Quantum Hall effect measurements are shown in Figure B.6. The device quality is poor and no quantum hall features are sufficiently discernible.

B.3 Supplementary data to chapter 4

30° device A is investigated at very high magnetic field. Spin and valley degeneracy are observed to break. (Figure B.7). Dirac peak resistance is plotted as a function of displacement fields for magnetic fields ranging from 0T to 36T (Figure B.8).

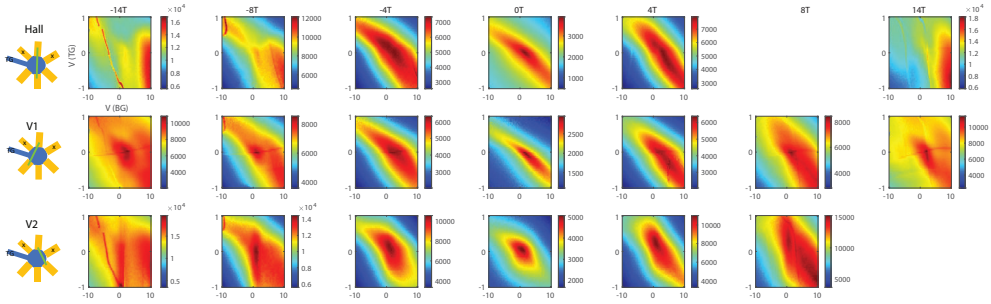

Figure B.3: Dual gate sweeps at various magnetic fields for three different contact configurations (Hall, V1, and V2; green line on diagram connects source and drain contacts). Sharp, resonance-like features are visible that vary with both gates and magnetic field, and are not symmetric with positive and negative magnetic field.

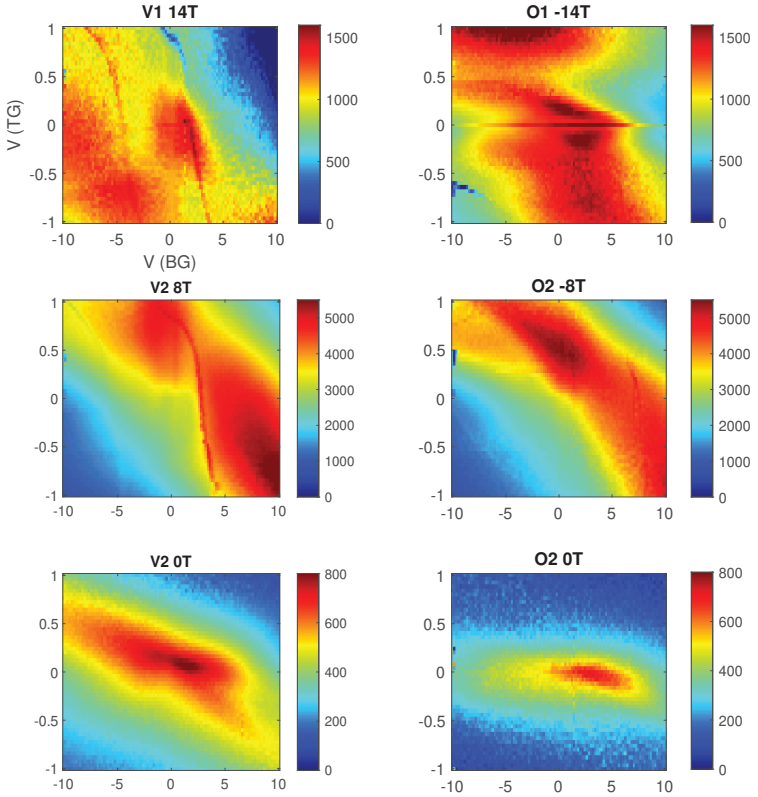

Figure B.4: Dual gate sweeps for pairs of conditions that should be equivalent due to Onsager reciprocity.

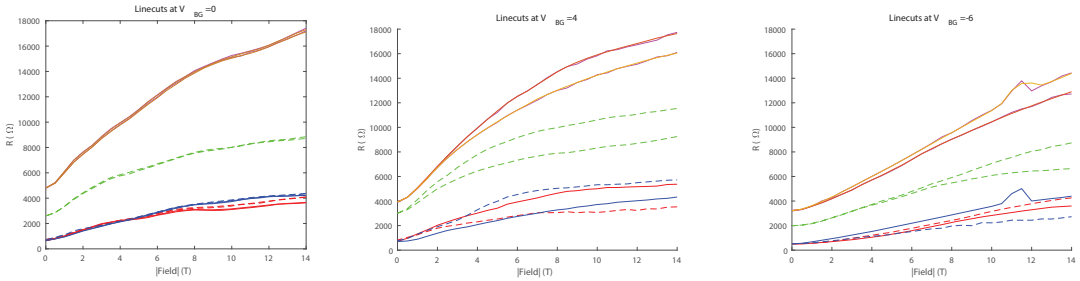

Figure B.5: Rxx vs B-field with topgate floated and backgate either floated or zero (both in first panel), and with backgates at nonzero values (second and third panel). Same-color lines are pairs that should be equal by Onsager reciprocity. Only at zero or no gate do they match up.

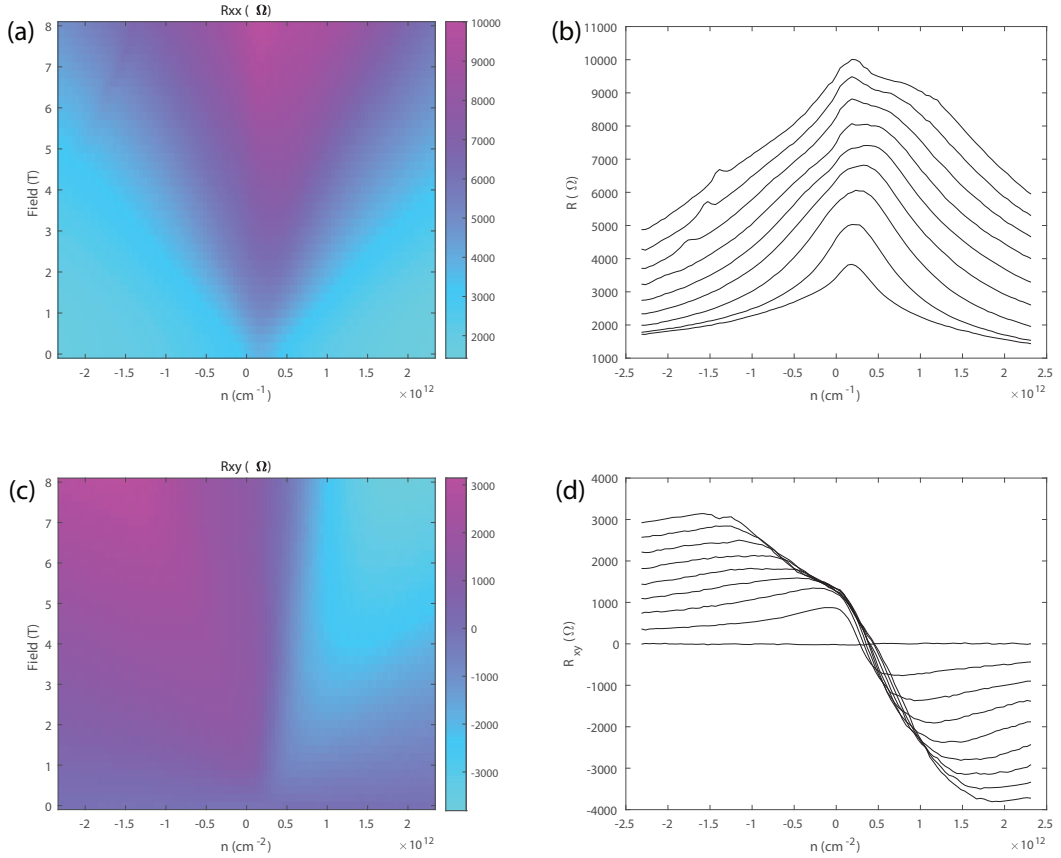

Figure B.6: Quantum hall effect data. (a) Rxx as a function of n and B. (b) Line cuts of Rxx at various B values. No hall oscillations are visible. Dirac peak at B=0 is very broad. (c) Rxy as a function of n and B. (d) Line cuts of Rxy at various B values. No hall plateaus are visible and resistance does not reach the resistance quantum.

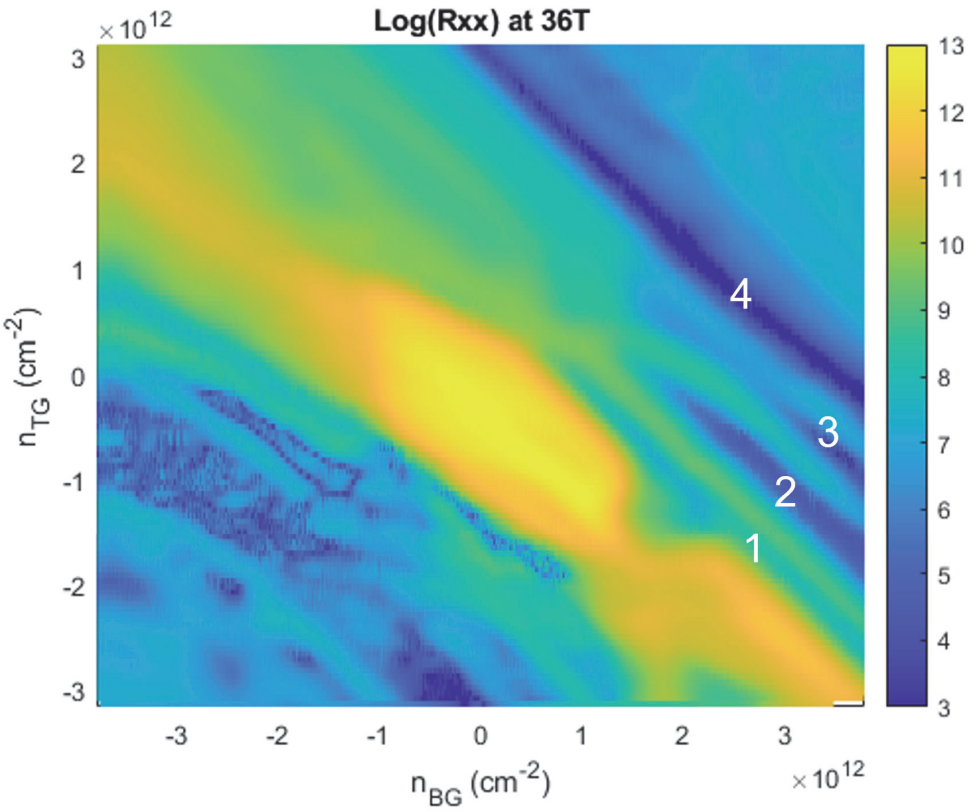

Figure B.7: Longitudinal resistance in the dual gate sweep of 30deg device A at B-field of 36.2 T. Color scale is logarithmic. Some filling factors are labeled, showing the lifted degeneracy due to high magnetic field. At D=0, the layer degeneracy of 2 remains.

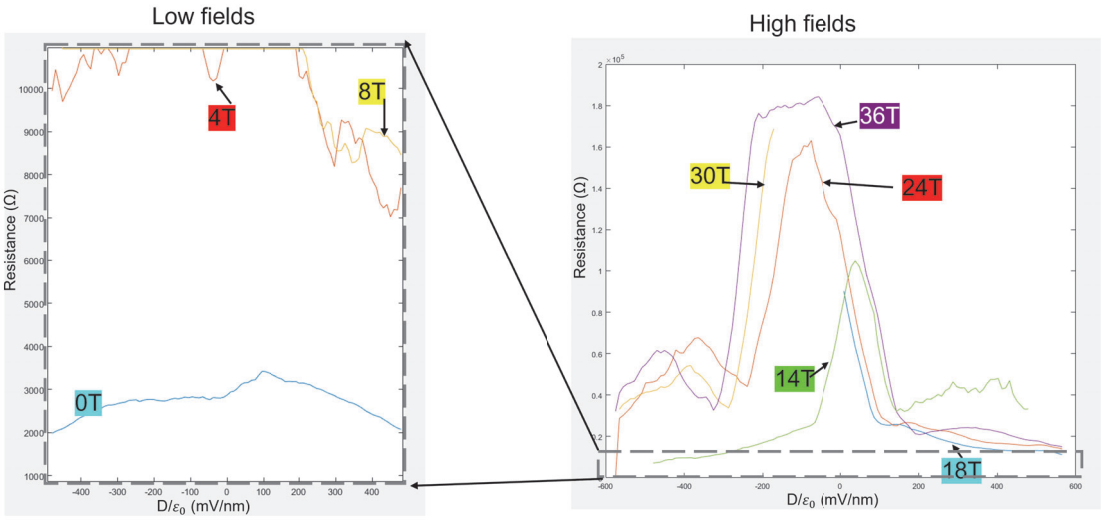

Figure B.8: Dirac peak resistance as a function of displacement field for various magnetic fields in the graphene 30deg device A.

C

Computations

This appendix details computations or calculations that were mentioned in lesser detail in the main text.

C.1 Schematic computation of graphene relaxation

To generate schematics of relaxed graphene (as in Chapter 5) with any of the four basis distortions (twist and isotropic, uniaxial, and shear strain), we create a periodic lattice distortion (PLD)[27] func-

tion in Matlab of the form

$$\Delta\vec{u}(R) = \eta \sum_{j=1}^{3} \vec{A}_j M(\vec{q}_j \cdot \vec{R}), \tag{C.1}$$

where $M(\vec{q}_j \cdot \vec{R})$ is a modulation function that can be written as a Fourier series. We can further compute the local shift vector and turn it into a color in configuration space. Note that this computation is not intended to be a quantitative description of the actual atomic positions in the system, but merely a schematic that produces the correct geometry, symmetry, and topology of the relaxed structure.

First we must generate the two lattices, with their distortion, prior to relaxation. In general, both lattices may be distorted relative to the ideal intrinsic lattice, which is the set of points $\vec{x}_0 = n\vec{a}_1 + m\vec{a}_2$ for integer n, m and lattice primitive vectors $\vec{a}$. In this example, we apply equal and opposite distortion to both lattices, to create a symmetric situation. Another instructive case is to set one lattice's transformation matrix to the identity, and only strain the second lattice. In general, the coordinates of each layer $\vec{x}_i = t_i\vec{x}_0$ where t_i is the transformation matrix to generate that layer from $\vec{x}_0$ and is related to the displacement gradient matrix by $t_i = 1 + \overline{d}_i$.

Accordingly, a displacement gradient matrix, disp and disp2, of opposite direction for lattice 1 and 2, are defined in Listing 1 for each distortion type. These $\overline{d}$ matrices are defined to have a fixed moiré length, determined by the parameter d.

Reciprocal lattices can be calculated for each lattice and used to determine the direction in which to apply the PLD, as in Listing 2. Reciprocal lattice points b_i of layer i are determined by the definition of reciprocal lattice:

$$\vec{b}_{i,\alpha} = 2\pi \frac{\vec{a}_{i,\beta} \times \vec{a}_{i,\gamma}}{\vec{a}_{i\alpha} \cdot (\vec{a}_{i,\beta} \times \vec{a}_{i,\gamma})} \tag{C.2}$$

where α, β and γ index the primitive vectors of the lattice (unit vector in the z-direction can be used as the third one), and the transformed lattice vectors are given by $\vec{a}_{i,\alpha} = t_i\vec{a_\alpha}$ in terms of the original lattice vectors.

```
for type = [”iso”, ”twist”, ”uni”, ”shear”]
d=0.08; %0.15; %0.065;

switch type
    case 'iso'
        disp = [-d/(1+d) 0; 0 -d/(1+d)];
        disp2 = [d/(1-d) 0; 0 d/(1-d)];
        %factor of 1/(1-d) to account for the fact
        %that Moire cell is bigger when burgers is parallel to t
    case 'twist'
        disp = [0 -d; d 0];
        disp2 = -disp;
    case 'uni'
        disp = [d/(1-d) 0; 0 -d/(1-d) ];
        disp2 = [-d/(1+d) 0; 0 d/(1+d) ];
    case 'shear'
        disp = [0 d; d 0];
        disp2 = -disp;
end

%transformation matrix, applied to lattice 2
trans = [1 0; 0 1]+disp;
%opposite transformation matrix, applied to lattice 1
trans_opp = [1 0; 0 1]+disp2;

a_0=0.246; %lattice constant (nm)
%Unit cell vectors (column vectors) with 60degree angle between
a = a_0*[1 1/2; 0 sqrt(3)/2];

t1 = inv(trans-trans_opp)*a(:,1);  %Moire cell vectors
t2 = inv(trans-trans_opp)*a(:,2);
```

Listing 1: Excerpt of Matlab code, defining transformation matrix to get a fixed Moire length

```
%Reciprocal lattice of transformed lattice
b1p=2*pi*cross([(trans*a1')',0],[0,0,1])/(det(trans)*vol);
b2p=2*pi*cross([(trans*a2')',0],[0,0,1])/(det(trans)*vol);
b3p=-b1p-b2p;

%Moire wavevector
q1=b1(1:2)-b1p(1:2);
q2=b2(1:2)-b2p(1:2);
q3=-q2-q1;

%Unit vector in PLD direction: average of the two reciprocal lattice points
A1=(b1(1:2)+b1p(1:2))/norm(b1(1:2)+b1p(1:2));
A2=(b2(1:2)+b2p(1:2))/norm(b2(1:2)+b2p(1:2));
A3=(b3(1:2)+b3p(1:2))/norm(b3(1:2)+b3p(1:2));
```

Listing 2: Excerpt of Matlab code, defining reciprocal lattice and PLD vector

The wavevectors of the modulation, q_1, q_2, and q_3, are the difference of the reciprocal lattices of layer 1 and layer 2: $\vec{q}_\alpha = \vec{b}_{1,\alpha} - \vec{b}_{2,\alpha}$. The direction vectors $\vec{A}$ in which the PLD is applied, point toward the average of the reciprocal lattice points of the two layers: $\vec{A}_\alpha \propto \vec{b}_{1,\alpha} + \vec{b}_{2,\alpha}$.

After applying the transformation matrix to generate the moiré lattice (Listing 3), the modulation function (as described in Equation C.1 and computationally defined in Listing 4) is applied to each point, with an amplitude eta that can be varied to vary the strength of relaxation. Hence the final points of lattice i are $x_i = t_i\vec{x}_0 + \Delta\vec{u}(R)$. In our example the modulation is a sawtooth wave, with 3 Fourier components.

We can then subtract each pair of modulated points, to get a local shift vector. This vector can be converted into a color based on a coloring scheme of configuration space (Listing 5), allowing us to create maps of real space colored by their configuration space values. A function "distance on torus" (not printed here) is defined to fold the difference between two vectors into the first unit cell,

```
    eta=0.08*a_0;  %Reconstruction strength: 0.08 is full reconstruction,
    %0 is pure moire

    pos=i*d1'+j*d2'; %Generate positions of untransformed lattice

    %Transformed lattice
    pos1=(trans_opp*pos')';
    pos2=(trans*pos')';

    %Apply PLD to both layers
    pos1_mod=pos1-eta*(A1*Modulation(q1,pos,phi1)
    +A2*Modulation(q2,pos,phi2)+A3*Modulation(q3,pos,phi3));
    pos2_mod=pos2+eta*(A1*Modulation(q1,pos,phi1)
    +A2*Modulation(q2,pos,phi2)+A3*Modulation(q3,pos,phi3));

    shift=pos2-pos1; %Shift vector unrelaxed

    param=pos2_mod-pos1_mod; %Order parameter: shift vector after relaxation

    color_h=Color_scheme(param,a1,a2,a_0,d1,d2);
    color_array(index,:)=color_h;
```

Listing 3: Excerpt of Matlab code, generating the positions of the transformed lattices and computing shift vector

```
function[M] = Modulation(q,r,phi)
    M=0;
    for n=1:3 %Choose as many fourier components as you like
       M = M + 1/n*sin(dot(q*n,r)+phi); %Sawtooth wave
    end
end
```

Listing 4: Excerpt of Matlab code, defining the modulation function

converting them from distances in $\mathbb{R}^2$ to distances on the torus.

C.2 Strain mapping "complicated algorithm"

To create strain maps in Section 5.3, we performed image processing in Python to segment the image into lines and nodes to prepare to interpolate shift vector values. Ideally an algorithm could be created to extract the lines straight from TEM images but we skip that step for now, and manually trace the red, green, and blue lines to create an "ideal" (i.e. noiseless), but still raster, image. First, nodes are found by searching for places where red, green, and blue coincide. Pixels that belong to red, green, and blue lines are put into lists using connectedComponents in Python's OpenCV library. Then, a dictionary is created for each line that includes the information on what color the line is and what nodes are part of it. Next, a radius around each node is removed from the image, effectively breaking the lines into line segments. Again, the connected components are found and a dictionary is created for each line segment. The parent line of each segment is identified, as well as the nodes that are its endpoints.

Next, each node must be assigned three integer values corresponding to the coefficients of $\vec{a_r}, \vec{a_g}$ and $\vec{a_b}$. An origin node is picked arbitrarily and assigned the coefficients $(u_r, u_g, u_b) = (0, 0, 0)$. Then, a red segment adjacent to the starting node is chosen to reach a second node, which is assigned $(u_r, u_g, u_b) = (0, 1, -1)$. Now that a second node is assigned, the choices are not arbitrary. A direction of increase for each vector has been determined. It is also the case that $u_r + u_g + u_b = 0$ at every node, because $\vec{a_r} + \vec{a_g} + \vec{a_b} = 0$. We also know that u_r is constant on red lines, u_g on green lines, etc. From each node, we move to its neighbors, and use these properties to fill in the rest of the coefficients. A nice property of this manner of assigning coefficients is it does not need to be told whether a given point is a vortex or an antivortex. Last, we fit B-splines to each line segment, and save the segments, lines, and knots of the splines into a Gmsh file.

```
function[color_h]= Color_scheme(vec,a1,a2,a_0,d1,d2)
    %Gaussian regions around key points get colors

    [~,AB_dist]=distance_on_torus(vec,d1,[a1',a2']);
    [~,BA_dist]=distance_on_torus(vec,d2,[a1',a2']);
    [~,AA_dist]=distance_on_torus(vec,[0;0],[a1',a2']);
    [~,burg1_dist]=distance_on_torus(vec,3*d1/2,[a1',a2']);
    [~,burg2_dist]=distance_on_torus(vec,(d1+d2)/2,[a1',a2']);
    [~,burg3_dist]=distance_on_torus(vec,d1-d2/2,[a1',a2']);

    %0.2 determines area of the color spot; can change
    burg1_val = exp(-(norm(burg1_dist)^2)/(0.2*a_0)^2);
    burg2_val = exp(-(norm(burg2_dist)^2)/(0.2*a_0)^2);
    burg3_val = exp(-(norm(burg3_dist)^2)/(0.2*a_0)^2);
    AB_val = exp(-(norm(AB_dist)^2)/(0.2*a_0)^2);
    BA_val = exp(-(norm(BA_dist)^2)/(0.2*a_0)^2);
    AA_val = exp(-(norm(AA_dist)^2)/(0.2*a_0)^2);

      color_h = ([0 1 0]*burg1_val + [1 0 0]*burg2_val
      + [0 0 1]*burg3_val  + 0.6*[1,1,1]*AB_val + 0.2*[1,1,1]*BA_val)
      + AA_val*[1,1,1];

end
```

Listing 5: Excerpt of Matlab code, coloring points based on their local configuration

The next part of the computation is done in Julia. The vector values of $\vec{a_r}$ and $\vec{a_g}$ (measured from a diffraction pattern) must be input ($\vec{a_b}$ can be found from the other two). Coefficients are attributed to points on lines and interpolated via an elastic model. The elastic model applies a cost to a large derivative in the u-field, as well as a cost to deviating from the known values on the lines. The resulting u-field is differentiated to get strain components. The values are defined on a mesh that is small compared to the moiré length. For plotting, the mesh values are interpolated onto a grid in Matlab.

C.3 Vortex density map

In Section 5.4 we claim that the determinant of the displacement gradient matrix is related to the local spatial density of vortices or antivortices. To show that, we relate the moiré cell area to $\overline{d}$.

Area of the unit cell is given by the cross product of the two unit cell vectors: $\vec{a_\alpha} \times \vec{a_\beta}$. Area of a moiré cell is given by the cross product of the moiré vectors: $\vec{M_\alpha} \times \vec{M_\beta}$. The moiré vectors are given by Equation 5.5 and 5.6, giving $\vec{M_\alpha} = (1 + \overline{d})\vec{x_1}$ where $\overline{d}\vec{x_1} = \vec{a_\alpha}$.

The lattice unit cell area, area_l, can be written $\vec{a_\alpha} \times \vec{a_\beta} = \overline{d}\vec{x_1} \times \overline{d}\vec{y_1} = \det[\overline{d}]\vec{x_1} \times \vec{y_1}$. Thus,

$$\vec{x_1} \times \vec{y_1} = \text{area}_l / \det[\overline{d}]. \tag{C.3}$$

The moiré cell area can be written:

$$\text{area}_M = (1 + \overline{d})\vec{x_1} \times (1 + \overline{d})\vec{y_1} = \det[1 + \overline{d}](\vec{x_1} \times \vec{y_1}) = \frac{\det[1 + \overline{d}]}{\det[\overline{d}]}\text{area}_l. \tag{C.4}$$

Since the components of $\overline{d}$ are small (<5%), $\det[1 + \overline{d}] \approx 1$ and we can say

$$\det[\overline{d}] \approx \text{area}_l / \text{area}_M. \tag{C.5}$$

This shows that $\det[\bar{d}]$ is related inversely to the moiré cell area, thus it is proportional to the density of moiré cells, or equivalently, the density of vortices.

C.4 Structure factor tilt calculations

To compute the structure factor of a tilted multilayer stack, as in Chapter 7, we first define the atomic positions in 3D space, with a height 0 for the first layer, h for the second layer, 2h for the third layer, etc. Then, we apply a general tilt to the system, which is parameterized by three angles, theta, phi, and beta (see Listing 6). Then, the coordinates are projected into the 2D plane, by simply truncating the third coordinate, since the z-component will not play a role in the final answer and thus is not useful to keep. Thus, the effect of tilt is to shift the atoms' relative positions in the plane. We then compute the structure factor of the projected coordinates, by Equation 1.3. Part of the computation is shown in Listing 7.

Taking the projection into the 2D plane (i.e. ignoring the z-component), does not discard any information when computing the structure factors for the $k_z = 0$ plane of k-space (where our detector is), since the z-component of the dot product in the exponential would be zero anyway.

```
function[v_t] = tilt_function(v, phi, beta, theta)
%v_t: 1x2 vector, projected coordinates of atom after tilting
%v: 1x3 vector, coordinates of atom before tilting
%phi,beta,theta: scalar, angles in radians

    R_theta = [cos(theta) -sin(theta) 0; sin(theta) cos(theta) 0; 0 0 1];
    R_phi = [cos(phi) 0 -sin(phi); 0 1 0; sin(phi) 0 cos(phi)];
    R_beta = [1 0 0; 0 cos(beta) -sin(beta); 0 sin(beta) -cos(beta)];

    vprime = R_theta*v'; %Rotate v into new coordinate system;
    vprime_t = R_beta*R_phi*vprime; %tilt along phi and beta axes
    v_t = R_theta\vprime_t;
    v_t = v_t(1:2); %remove third dimension, i.e. project into 2D plane
end
```

Listing 6: Excerpt of Matlab code, computing the projected coordinates of a basis atom after tilting the material with β tilt = beta and α tilt = phi where the α tilt axis is theta degrees from the x-axis of the coordinate system

```
%A, B, and C orientation:
%Defines the basis vectors in the unit cell for each possible layer shift
dA = [0 0 ; a1/3+a2/3];
dB = [0,0; 2*a1/3+2*a2/3];
dC = [a1/3+a2/3; 2*a1/3+2*a2/3];

%layer orientation: select whatever combo you want
%(e.g. Layer1 = dA; Layer2=dB; Layer3=dA for ABA stacking)
Layer1 = dA;
Layer2 = dB;
Layer3 = dC;

%Basis
d1=@(phi) tilt_function([Layer1(1,:),0], phi, beta, theta);
d2=@(phi) tilt_function([Layer1(2,:),0], phi, beta, theta);

d3=@(phi) tilt_function([Layer2(1,:),h], phi, beta, theta);
d4=@(phi) tilt_function([Layer2(2,:),h], phi, beta, theta);

d5=@(phi) tilt_function([Layer3(1,:),2*h], phi, beta, theta);
d6=@(phi) tilt_function([Layer3(2,:),2*h], phi, beta, theta);

%Structure factor
Struc = @(k,phi) exp(1i*dot(k,d1(phi)))+exp(1i*dot(k,d2(phi)))
+exp(1i*dot(k,d3(phi)))+exp(1i*dot(k,d4(phi)))
+exp(1i*dot(k,d5(phi)))+exp(1i*dot(k,d6(phi)));
```

Listing 7: Excerpt of Matlab code, setting the basis atom positions in 3D space and computing the structure factor of their tilted positions

D

Mathematical details

This appendix contains mathematical constructions that support results in the main text.

D.1 Algebraic description of punctured torus

This section was written in large part by Professors Mingyong Kim and Jung Hoon Han based on our discussion.

The conventional definition of vortex applies when the configuration space is a circle and the

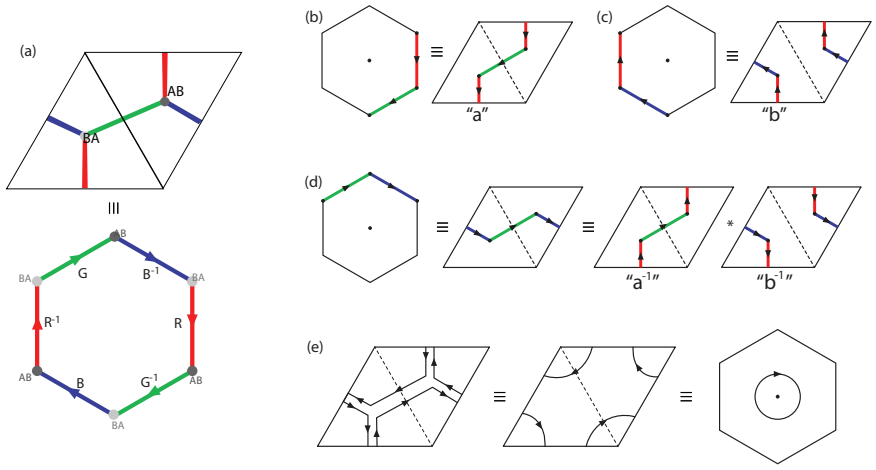

Figure D.1: (a) Defining paths on the torus as R, G, and B and their inverses. (b) The RG^{-1} move in the hexagonal zone scheme of the configuration space is translated into a non-contractible loop in the rhombic zone scheme. It is called the a-move. (c) The BR^{-1} move in the hexagonal zone scheme of the configuration space is translated into a different non-contractible loop in the rhombic zone scheme. It is called the b-move. (d) The GB^{-1} move in the hexagonal zone scheme of the configuration space is translated into a third non-contractible loop that can be decomposed as a product of the previous two moves as the $a^{-1}b^{-1}$-move. (e) The $aba^{-1}b^{-1}$-loop is equivalent to a circle round the $\vec{u} = 0$. It is a non-contractible loop due to the high-energy barrier for $\vec{u} = 0$ configuration.

relevant homotopy group is $\pi_1(S^1) = \mathbb{Z}$. With the theta space taking over the circle as the configuration space, a new mathematical definition of a vortex is called for. This is despite the fact that a heuristic picture of the Burgers vector winding either clockwise or counterclockwise as the real-space trajectory is traversed around the AA node seems to work well, at least intuitively. A most profound departure from the U(1), abelian vortex picture is that a *non-abelian* description of vorticity in the moiré superlattice system is called for.

To set the stage, we transcribe the BA $\rightarrow$ AB $\rightarrow$ BA move through the R and G^{-1} lines in Fig. D.1(a) in the parallelogram scheme as shown in Fig. D.1(b), where it appears as a non-contractible loop. The other BA $\rightarrow$ AB $\rightarrow$ BA move through the B and R^{-1} lines in the hexagon scheme becomes a second non-contractible loop in the parallelogram unit cell. We call the first and the second moves as a and b, the two generators of the free group[97,98]. The third BA $\rightarrow$ AB $\rightarrow$ BA move through G and B^{-1} lines of the hexagon can be decomposed, as shown in Fig. D.1(d), as the in-

verse of a move followed by the inverse of b, or $a^{-1}b^{-1}$. A complete loop around the edges of the hexagonal unit cell is equivalent to the algebraic operation $aba^{-1}b^{-1} \equiv [a,b]$. (Our convention is to perform the operation appearing on the left side of the product first.) The commutator $[a,b]$ in the language of free group with two generators a,b represents a "vortex" centered about the AA defect when the relevant configuration space is a punctured torus. The vorticity $[a,b]$ is non-trivial in the sense that it is not contractible to an identity, as illustrated in Fig. D.1(e). After cancelling out the paths that are traversed both ways, the overall path for $[a,b]$ becomes equivalent to four partial loops around the four corners of the parallelogram, equal to a full loop round $\vec{u} = 0$. On a torus such a loop can be contracted to zero and become trivial, but not for a punctured torus which applies to the moiré superlattice. The anti-vortex has the algebraic representation $[b,a] = bab^{-1}a^{-1} = [a,b]^{-1}$. Geometrically, this amounts to starting from the same BA point on the upper left corner of the hexagon and making a complete counter-clockwise loop round it.

The fundamental group of the punctured torus is $F = F_2$, the free group on two generators a,b[97,98]. The a and b generators correspond to the two independent ways in which one can encircle the torus. In an ordinary torus the two operations a and b do commute (abelian), and the only elements of the fundamental group on torus are $a^m b^n$, which count the number of loops in both directions. For a punctured torus such commutativity is lost, and consequently the group structure becomes non-abelian.

Elements of the free group F_2 consist of every conceivable sequence of "letters" such as $abaabbbaa\cdots$ called "words". Keep in mind that both letters a and b have specific geometric moves associated with them. At this point it is helpful to go over well-established theorems in free groups to guide our thinking.

We now use F to denote the original free group F_2. Given two elements $x,y \in F$, the commutator is denoted $[x,y] \equiv xyx^{-1}y^{-1}$. The "lower central series" of the free group can be defined as follows. One begins with $F^1 = F$ which is the original free group, then $F^2 = [F,F]$ is the subgroup of F

consisting of all commutators $[x, y]$ and their products, i.e., all elements of the form

$$[x_1, y_1][x_2, y_2] \cdots [x_n, y_n], \quad (x_i, y_i \in F).$$

The subgroup F^2 is also a normal subgroup, meaning that the quotient space F^1/F^2 is a group.

Now one can proceed inductively and define

$$F^n = [F, F^{n-1}],$$

the subgroup generated by all elements of the form $[x, y]$ where $x \in F$ and $y \in F^{n-1}$. It is easy to check from the definition that

$$F^1 \supset F^2 \supset F^3 \supset F^4 \cdots$$

Such "filtration" gives a nice way to study a free group structure 'one layer at a time'.

Some facts that are worth noting about the lower central series are summarized:

1. Any element f_1 of $F^1 = F$ can be uniquely written $a^{m_1} b^{n_1} f_2$ with $n_1, m_1 \in \mathbb{Z}$ and $f_2 \in F^2$.
2. Any element f_2 of F^2 can be uniquely written $[a, b]^{m_2} f_3$ where $m_2 \in \mathbb{Z}$ and $f_3 \in F^3$.
3. Any element f_3 of F^3 can be uniquely written $[a, [a, b]]^{m_3} [b, [a, b]]^{n_3} f_4$ with $m_3, n_3 \in \mathbb{Z}$ and $f_4 \in F^4$.
4. Any element f_4 of F^4 can be uniquely written $([a, [a, [a, b]])^{m_4} ([a, [b, [a, b]]])^{n_4} ([b, [b, [a, b]]])^{p_4} f_5$ with $m_4, n_4, p_4 \in \mathbb{Z}$ and $f_5 \in F^5$.

By putting all of the above statements together, one sees that any element f in the free group can be

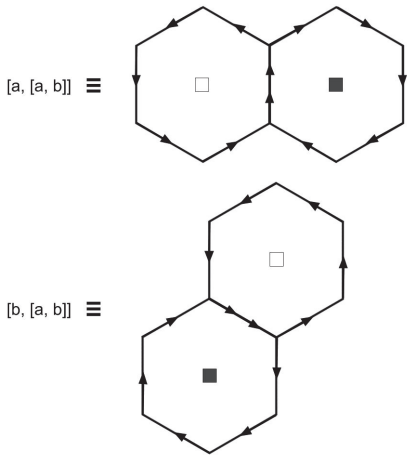

Figure D.2: Graphical representation of the double commutators $[a,[a,b]],[b,[a,b]]$. They give vortex dipoles oriented along the two directions of the triangular lattice. Filled (empty) square is a vortex (anti-vortex).

uniquely written as

$$f = a^{m_1} b^{n_1} [a,b]^{m_2} [a,[a,b]]^{m_3} [b,[a,b]]^{n_3} ([a,[a,[a,b]]])^{m_4} ([a,[b,[a,b]]])^{n_4} ([b,[b,[a,b]]])^{p_4} f_5 \tag{D.1}$$

and so on. In general, each F^k is a normal subgroup, and $F^k/F^{k+1} \simeq \mathbb{Z}^{r_k}$, meaning the quotient group is isomorphic to a product of r_k integer groups $\mathbb{Z} \times \cdots \times \mathbb{Z}$. The number of generators is r_k for a given quotient group F^k/F^{k+1}. Although the free group itself is non-abelian, the quotient group F^k/F^{k+1} is abelian, characterized by a set of r_k integers. These integers then go on to play the role of topological quantum numbers in physical contexts.

Elements of the free group (D.1) for which $m_1 = n_1 = 0$ refer to closed loops in real-space graphical representation. It is clear that these are the only elements of F that we are interested in. Elements for which $f_5 = e$ (an identity) and $m_3 = n_3 = m_4 = n_4 = p_4 = 0$ are $f = [a,b]^{m_2}$ with nonzero m_2. These are the elements of the quotient group F^2/F^3 and represent the vortices $(m_2 > 0)$ and antivortices $(m_2 < 0)$ in physical contexts.

To consider higher-order topological defects, consider elements for which $f_5 = e$ and all integers in Equation (D.1) equal to zero except (m_3, n_3):

$$f = [a, [a, b]]^{m_3} [b, [a, b]]^{n_3}. \tag{D.2}$$

Pictorial representations for the double commutators $[a, [a, b]]$, $[b, [a, b]]$ are easily obtained by tracing out paths according to definitions of a and b given in Fig. D.1. We encourage readers to perform such exercises themselves and arrive at their graphical representations shown in Fig. D.2. They are precisely the graphical representation of vortex-antivortex pairs (vortex dipoles) lying along the two crystallographic directions of the triangular lattice.

Next in line is the description of vortex quadrupole structure as triple commutators. According to Equation (D.1), there are only three generators of the quotient group $F^4/F^5 \simeq \mathbb{Z} \times \mathbb{Z} \times \mathbb{Z}$. How does one know there are only three generators at this level of filtration?

There is a theorem that gives the number of generators (r_k) at each level k through the formula

$$g^k = \sum_{d|k} d \cdot r_d. \tag{D.3}$$

In this formula the sum runs over all divisors d of the given integer k. For a free group with only two generators we have $g = 2$ on the left side of the equation. To see how the formula works with $g = 2$, first set $k = 1$ to find $2 = r_1$. It means that the quotient group F^1/F^2 has two generators, namely a and b. At $k = 2$ we have $2^2 = r_1 + 2r_2 = 2 + 2r_2$ or $r_2 = 1$, hence there is only one generator of F^2/F^3 which is the commutator $[a, b]$. At $k = 3$ we have $2^3 = r_1 + 3r_3 = 2 + 3r_3$, and $r_3 = 2$ is the number of generators for F^3/F^4, namely $[a, [a, b]]$ and $[b, [a, b]]$. Finally, at $k = 4$ we get $2^4 = r_1 + 2r_2 + 4r_4 = 2 + 2 + 4r_4$, and $r_4 = 3$ is the number of generators of F^4/F^5 given by $[a, [a, [a, b]]]$, $[a, [b, [a, b]]]$, $[b, [b, [a, b]]]$. It is an arduous, but fun exercise to draw the

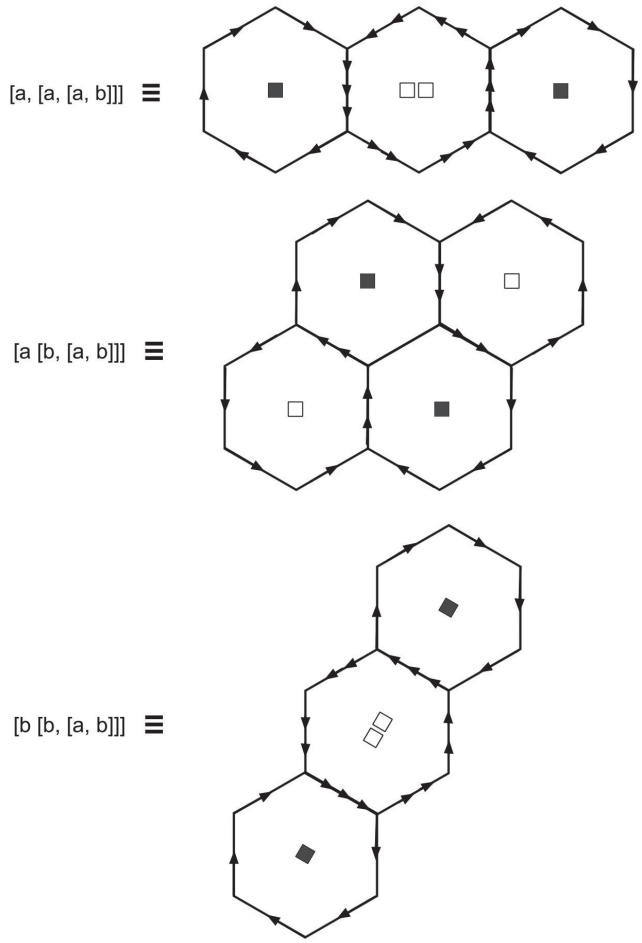

Figure D.3: Graphical representation of the three triple commutators $[a,[a,[a,b]]]$, $[a,[b,[a,b]]]$, $[b,[b,[a,b]]]$ correspond to three different kinds of vortex quadrupoles in real space.

real-space paths corresponding to each of the triple commutator. The results are the three distinct vortex quadrupole configurations in real space shown in Figure D.3.

D.1.1 RGB formulation of vorticity

TEM dark field imaging allows the domain walls converging on the AA defect to be color-coded as R, G, B and its inverses R^{-1}, G^{-1}, and B^{-1} as shown in Figure D.1(a). Inverses mean the directions of the transition vectors have been reversed. The free group language of the previous subsection gives a mathematically complete account of the vortex and antivortex structures in the moiré superlattice, but it is helpful to translate the somewhat abstract notion of generators a, b to a tangible, experimental quantities R, G, B and their inverses. The relevant mapping from a, b to the R, G, B scheme can be read off from Figure D.1 as

$$a \leftrightarrow RG^{-1}, \;\; b \leftrightarrow BR^{-1} \;\; ba \leftrightarrow BG^{-1}. \tag{D.4}$$

By direct substitution we obtain the commutator (vortex)

$$[a, b] = RG^{-1}BR^{-1}GB^{-1}, \tag{D.5}$$

which is a product of transition vectors over the six domain walls in succession. In the same scheme we have the antivortex commutator

$$[b, a] = BG^{-1}RB^{-1}GR^{-1}. \tag{D.6}$$

Any cyclic permutation of the six letters gives rise to the equivalent vortex or antivortex. The RGB scheme permits a direct identification of the vorticity in terms of the experimentally identified colors of the domain walls converging on a given AA defect. If the six domain walls emanating from a AA

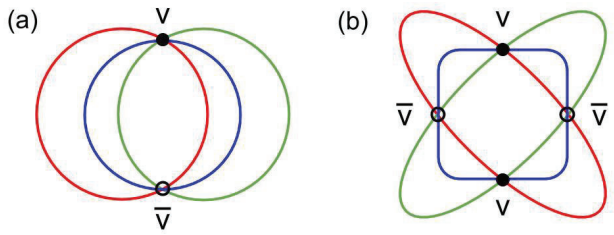

Figure D.4: a) RGB graphical representation of a vortex dipole with v(vortex, filled circle) and $\bar{v}$(anti-vortex, empty circle) sites. (b) Quadrupole configuration with alternating $v\bar{v}v\bar{v}$ cores.

defect appear, for instance, in the order of $RGBRGB$ as one goes counter-clockwise around it (the color itself cannot be distinguished from its inverse color), it is to be interpreted as $RG^{-1}BR^{-1}GB^{-1}$ given in Equation (D.5) and classified as a vortex. If the colors appear as $RBGRBG$, it is an anti-vortex according to Equation (D.6). The only mathematical rule to keep in mind is that in transcribing the observed color patterns to the sequence of letters, one must have one of the letters R, G, B followed one of their inverse colors R^{-1}, G^{-1}, B^{-1} and vice versa. Generalizations of the RGB scheme to vortex-antivortex dipole and/or vortex quadrupole structure can be performed.

Figure D.4 shows the vortex dipole and quadrupole configurations in terms of intersecting RGB loops. A small circle drawn around each intersection can determine the vorticity of that point. For instance the filled (empty) circle round the top (bottom) intersection in Fig. D.4(a) reads the product of letters $RG^{-1}BR^{-1}GB^{-1}$ ($BG^{-1}RB^{-1}GR^{-1}$) going counter-clockwise, corresponding to a vortex (an antivortex). Vortex quadrupole construction is done by having the three RGB loops intersect at four different points, as shown in Fig. D.4(b). In both cases, a large circle drawn far away from the loops fails to cross any of the RGB lines.

It is possible to construct examples of vortex dipole configurations with loops extending out to infinity (hence crossing an arbitrary large circle) as in Fig. D.5(a) and (b). The group elements assigned to each configuration can be calculated straightforwardly, leading to $[a,[b,a]]$ and $[ab,[b,a]]$ for the left and right configurations, respectively.

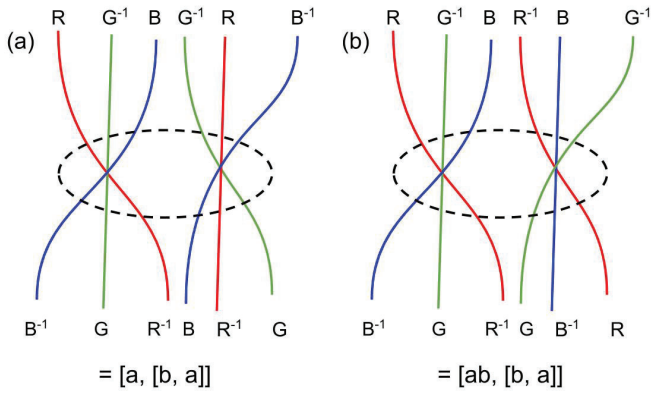

Figure D.5: (a) Extended vortex dipole configuration characterized by the letter sequence $RG^{-1}BG^{-1}RB^{-1}GR^{-1}BR^{-1}GB^{-1}$. After simple calculation, this becomes equivalent to $[a, [b, a]]$. (b) Another extended vortex dipole configuration, expressible as the double commutator $[ab, [b, a]]$.

This kind of scheme is applicable to experimental situations. Draw a large loop enclosing a given TEM image in the manner shown in Fig. D.6, (as done e.g. in Fig. 5.12) then start counting the dislocation lines according to the *RGB* scheme. The RGB-based words can be converted to the *ab*-letter scheme with the help of the dictionary given in Equation (D.4). The *ab*-based word can subsequently be converted to various commutators and higher-order commutators until it is cast in the general form given in Equation (D.1), from which the total vorticity, dipole numbers, quadrupole numbers and so on can be read off.

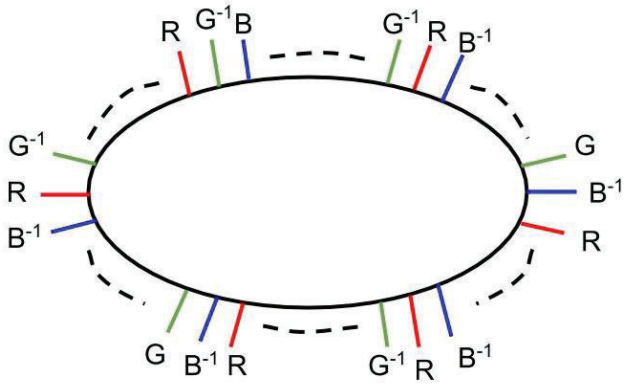

Figure D.6: General configuration of RGB lines extending from an arbitrary circle drawn on an experimentally TEM image. By writing out the RGB letters along the circumference of the circle, one can read off the total vorticity, number of dipoles, etc. contained in the circle.

References

[1] L. Brus, "Size, dimensionality, and strong electron correlation in nanoscience," *Accounts of Chemical Research*, vol. 47, no. 10, p. 2951–2959, 2014.

[2] A. H. C. Neto, F. Guinea, N. M. R. Peres, K. S. Novoselov, and A. K. Geim, "The electronic properties of graphene," *Review of Modern Physics*, vol. 81, 2009.

[3] T. Wehling, A. Black-Schaffer, and A. Balatsky, "Dirac materials," *Advances in Physics*, vol. 63, no. 1, pp. 1–76, 2014.

[4] E. McCann and M. Koshino, "The electronic properties of bilayer graphene," *Reports on Progress in Physics*, vol. 76, no. 5, 2013.

[5] K. Kim, M. Yankowitz, B. Fallahazad, S. Kang, H. C. P. Movva, S. Huang, S. Larentis, C. M. Corbet, T. Taniguchi, K. Watanabe, S. K. Banerjee, B. J. LeRoy, and E. Tutuc, "van der waals heterostructures with high accuracy rotational alignment," *Nano Letters*, vol. 16, no. 3, p. 1989–1995, 2016.

[6] Y. Cao, J. Y. Luo, V. Fatemi, S. Fang, J. D. Sanchez-Yamagishi, K. Watanabe, T. Taniguchi, E. Kaxiras, and P. Jarillo-Herrero, "Superlattice-induced insulating states and valley-protected orbits in twisted bilayer graphene," *Physical Review Letters*, vol. 117, pp. 1–5, 2016.

[7] C. R. Dean, L. Wang, P. Maher, C. Forsythe, F. Ghahari, Y.Gao, J. Katoch, M. Ishigami, P. Moon, M. Koshino, T. Taniguchi, K. Watanabe, K. L. Shepard, J.Hone, and P. Kim, "Hofstadter's butterfly and the fractal quantum hall effect in moire superlattices," *Nature*, vol. 49 7, no. 7451, pp. 598–602, 2013.

[8] B. Hunt, J. D. Sanchez-Yamagishi, A. F. Young, M. Yankowitz, B. J. LeRoy, K. Watanabe, T. Taniguchi, P. Moon, M. Koshino, P. Jarillo-Herrero, and R. C. Ashoori, "Massive dirac fermions and hofstadter butterfly in a van der waals heterostructure," *Science*, vol. 340, no. 6139, p. 1427–1430, 2013.

[9] J. M. B. Lopes dos Santos, N. M. R. Peres, and A. H. C. Neto, "Graphene bilayer with a twist: Electronic structure," *Physical Review Letters*, vol. 99, no. 25, 2007.

[10] S. Shallcross, S. Sharma, E. Kandelaki, and O. A. Pankratov, "Electronic structure of turbostratic graphene," *Physical Review B*, vol. 81, no. 23, 2010.

[11] P. Moon and M. Koshino, "Energy spectrum and quantum hall effect in twisted bilayer graphene," *Physical Review B*, vol. 85, no. 19, 2012.

[12] R. Bistritzer and A. H. MacDonald, "Moire bands in twisted double-layer graphene," *Proceedings of the National Academy of the Sciences of the USA*, vol. 108, no. 30, p. 12233–12237, 2011.

[13] M. M. van Wijk, A. Schuring, M. I. Katsnelson, and A. Fasolino, "Relaxation of moiré patterns for slightly misaligned identical lattices: graphene on graphite," 2*D Materials*, vol. 2, no. 3, 2015.

[14] E. Cancès, P. Cazeaux, and M. Luskin, "Generalized kubo formulas for the transport properties of incommensurate 2D atomic heterostructures," *Journal of Mathematical Physics*, vol. 58, no. 06, 2017.

[15] S. Carr, D. Massatt, S. B. Torrisi, P. Cazeaux, M. Luskin, and E. Kaxiras, "Relaxation and domain formation in incommensurate two-dimensional heterostructures," *Physical Review B*, vol. 98, no. 22, 2018.

[16] Y. Cao, V. Fatemi, A. Demir, S. Fang, S. L. Tomarken, J. Y. Luo, J. D. Sanchez-Yamagishi, K. Watanabe, T. Taniguchi, E. Kaxiras, R. C. Ashoori, and P. Jarillo-Herrero, "Correlated insulator behaviour at half-filling in magic-angle graphene superlattices," *Nature*, vol. 556, no. 7699, pp. 80–84, 2018.

[17] Y. Cao, V. Fatemi, S. Fang, K. Watanabe, T. Taniguchi, E. Kaxiras, and P. Jarillo-Herrero, "Unconventional superconductivity in magic-angle graphene superlattices," *Nature*, vol. 556, no. 7699, pp. 43–50, 2018.

[18] O. M. Braun and Y. S. Kivshar, "Nonlinear dynamics of the Frenkel—Kontorova model," *Physics Reports*, vol. 306, no. 1, pp. 1–108, 1998.

[19] R. W. Balluffi, Y. Komem, and T. Schober, "Electron microscope studies of grain boundary dislocation behavior," *Surface Science*, vol. 31, pp. 68–103, 1972.

[20] J. S. Alden, A. W. Tsen, P. Y. Huang, R. Hovden, L. Brown, J. Park, D. A. Muller, and P. L. McEuen, "Strain solitons and topological defects in bilayer graphene," *Proceedings of the National Academy of Sciences of the USA*, vol. 110, no. 28, pp. 11256–11260, 2013.

[21] C. R. Woods, L. Britnell, A. Eckmann, R. S. Ma, J. C. Lu, H. M. Guo, X. Lin, G. L. Yu, Y. Cao, R. V. Gorbachev, A. V. Kretinin, J. Park, L. A. Ponomarenko, M. I. Katsnelson, Y. N. Gornostyrev, K. Watanabe, T. Taniguchi, C. Casiraghi, H.-J. Gao, A. K. Geim, and K. S. Novoselov, "Commensurate–incommensurate transition in graphene on hexagonal boron nitride," *Nature Physics*, vol. 10, p. 451–456, 2014.

[22] N. W. Ashcroft and N. D. Mermin, *Solid State Physics*. Fort Worth: Saunders College Publishing, 1976.

[23] J. Lin, W. Fang, W. Zhou, A. R. Lupin, J. C. Idrobo, J. Kong, S. J. Pennycook, , and S. T. Pantelide, "Ac/ab stacking boundaries in bilayer graphene," *Nano Letters*, vol. 13, no. 7, p. 3262–3268, 2013.

[24] B. Butz, C. Dolle, F. Niekiel, K. Weber, D. Waldmann, H. B. Weber, B. Meyer, and E. Spiecker, "Dislocations in bilayer graphene," *Nature*, vol. 505, p. 533–537, 2014.

[25] L. Brown, R. Hovden, P. Huang, M. Wojcik, D. A. Muller, and J. Park, "Twinning and twisting of tri- and bilayer graphene," *Nano Letters*, vol. 12, no. 3, p. 1609–1615, 2012.

[26] Z. Chen, M. Odstrcil, Y. Jiang, Y. Han, M.-H. Chiu, L.-J. Li, and D. A. Muller, "Mixed-state electron ptychography enables sub-angstrom resolution imaging with picometer precision at low dose," *Nature Communications*, vol. 11, no. 2994, 2020.

[27] S. H. Sung, Y. M. Goh, H. Yoo, R. Engelke, H. Xie, Z. Li, A. Ye, P. B. Deotare, A. J. Mannix, J. Park, L. Zhao, P. Kim, and R. Hovden, "Torsional periodic lattice distortions and diffraction of twisted 2D materials," *preprint*, 2022.

[28] R. H. Friend and D. Jerome, "Periodic lattice distortions and charge density waves in one- and two-dimensional metals," *Journal of Physics C: Solid State Physics*, vol. 12, no. 8, pp. 1441–1447, 1979.

[29] M. Conrad, F. Wang, M. Nevius, K. Jinkins, A. Celis, M. Nair, A. Taleb-Ibrahim, A. Tejeda, Y. Garreau, A. Vlad, A. Coati, P. Miceli, and E. Conrad, "Wide bandgap semiconductor from a hidden 2D incommensurate graphene phase," *Nano Letters*, vol. 17, no. 1, pp. 341–347, 2016.

[30] D. B. Williams and C. B. Carter, *Transmission Electron Microscopy, Part 2: Diffraction*. New York: Springer, 1996.

[31] B. Shevitski, M. Mecklenburg, W. A. Hubbard, E. R. White, B. Dawson, M. S. Lodge, M. Ishigami, and B. C. Regan, "Dark-field transmission electron microscopy and the debye-waller factor of graphene," *Physical Review B*, vol. 87, no. 04, 2013.

[32] D. Mitchell, "Dave Mitchell's DigitalMicrograph™ scripting website." http://www.dmscripting.com/index.html, 2022. 20-2-18.

[33] K. Zhang and E. B. Tadmor, "Structural and electron diffraction scaling of twisted graphene bilayers," *Journal of the Mechanics and Physics of Solids*, vol. 112, pp. 225–238, 2017.

[34] H. Yoo, R. Engelke, S. Carr, S. Fang, K. Zhang, P. Cazeaux, S. H. Sung, R. Hovden, A. W. Tsen, T. Taniguchi, K. Watanabe, G.-C. Yi, M. Kim, M. Luskin, E. B. Tadmor, E. Kaxiras,

and P. Kim, "Atomic and electronic reconstruction at the van der waals interface in twisted bilayer graphene," *Nature Materials*, vol. 18, p. 448–453, 2019.

[35] F. Zhang, A. H. MacDonald, and E. J. Mele, "Valley chern numbers and boundary modes in gapped bilayer graphene," *Proceedings of the National Academy of the Sciences of the USA*, vol. 110, no. 26, p. 10546–10551, 2013.

[36] F. V. Tikhonenko, D. W. Horsell, R. V. Gorbachev, , and A. K. Savchenko, "Weak localization in graphene flakes," *Physical Review Letters*, vol. 100, no. 5, pp. 8–11, 2008.

[37] J. D. Sanchez-Yamagishi, T. Taychatanapat, K. Watanabe, T. Taniguchi, A. Yacoby, , and P. Jarillo-Herrero, "Quantum hall effect, screening, and layer-polarized insulating states in twisted bilayer graphene," *Physical Review Letters*, vol. 108, no. 7, 2012.

[38] P. San-Jose and E. Prada, "Helical networks in twisted bilayer graphene under interlayer bias," *Physical Review B*, vol. 88, no. 12, 2013.

[39] P. Rickhaus, J. Wallbank, S. Slizovskiy, R. Pisoni, H. Overweg, Y. Lee, M. Eich, M.-H. Liu, K. Watanabe, T. Taniguchi, T. Ihn, and K. Ensslin, "Transport through a network of topological channels in twisted bilayer graphene," *Nano Letters*, vol. 18, no. 11, p. 6725–6730, 2018.

[40] C. D. Beule, F. Dominguez, and P. Recher, "Aharonov-bohm oscillations in minimally twisted bilayer graphene," *Physical Review Letters*, vol. 125, no. 9, 2020.

[41] J. Li, R.-X. Zhang, Z. Yin, J. Zhang, K. Watanabe, T. Taniguchi, C. Liu, and J. Zhu, "A valley valve and electron beam splitter," *Science*, vol. 362, no. 6419, p. 1149–1152, 2018.

[42] S. S. Sunku, G.X.Ni, B. Y. Jiang, H. Yoo, A. Sternbach, A. S. McLeod, T. Stauber, L. Xiong, T. Taniguchi, K. Watanabe, P. Kim, M. M. Fogler, and D. N. Basov, "Photonic crystals for nano-lightin moiré graphene superlattices," *Science*, vol. 362, no. 6419, pp. 1153–1156, 2018.

[43] S. S. Sunku, D. Halbertal, R. Engelke, H. Yoo, N. R. Finney, N. Curreli, G. Ni, C. Tan, A. S. McLeod, C. F. B. Lo, C. R. Dean, J. C. Hone, P. Kim, and D. N. Basov, "Dual-gated graphene devices for near-field nano-imaging," *Nano Letters*, vol. 21, no. 4, pp. 1688–1693, 2021.

[44] Y. Luo, R. Engelke, M. Mattheakis, M. Tamagnone, S. Carr, K. Watanabe, T. Taniguchi, E. Kaxiras, P. Kim, and W. L. Wilson, "In situ nanoscale imaging of moiré superlattices in twisted van der waals heterostructures," *Nature Communications*, vol. 11, no. 4209, 2020.

[45] D. Wang, G. Chen, C. Li, M. Cheng, W. Yang, S. Wu, G. Xie, J. Zhang, J. Zhao, X. Lu, P. Chen, G. Wang, J. Meng, J. Tang, R. Yang, C. He, D. Liu, D. Shi, K. Watanabe, T. Taniguchi, J. Feng, Y. Zhang, , and G. Zhang, "Thermally induced graphene rotation on hexagonal boron nitride," *Physical Review Letters*, vol. 116, no. 12, 2016.

[46] B. Tsim, N. N. T. Nam, and M. Koshino, "Perfect one-dimensional chiral states in biased twisted bilayer graphene," *Physical Review B*, vol. 101, no. 12, 2020.

[47] S. Theil, M. Fleischmann, R. Gupta, F. Rost, F. Wullschläger, S. Sharma, B. Meyer, , and S. Shallcross, "General relation between stacking order and chern index: A topological map of minimally twisted bilayer graphene," *Physical Review B*, vol. 104, no. 12, 2021.

[48] E. J. G. Santos and E. Kaxiras, "Electric-field dependence of the effective dielectric constant in graphene," *Nano Letters*, vol. 13, no. 3, p. 898–902, 2013.

[49] Y. Zhang, T.-T. Tang, C. Girit, Z. Hao, M. C. Martin, A. Zettl, M. F. Crommie, Y. R. Shen, and F. Wang, "Direct observation of a widely tunable bandgap in bilayer graphene," *Nature*, vol. 459, p. 820–823, 2009.

[50] K. Kanayama and K. Nagashio, "Gap state analysis in electric-field-induced band gap for bilayer graphene," *Scientific Reports*, vol. 5, no. 15789, 2015.

[51] J. Li, K. Wang, K. J. McFaul, Z. Zern, Y. Ren, K. Watanabe, T. Taniguchi, Z. Qiao, , and J. Zhu, "Gate-controlled topological conducting channels in bilayer graphene," *Nature Nanotechnology*, vol. 11, p. 1060–1065, 2016.

[52] S. G. Xu, A. I. Berdyugin, P. Kumaravadivel, F. Guinea, R. K. Kumar, D. A. Bandurin, S. V. Morozov, W. Kuang, B. Tsim, S. Liu, J. H. Edgar, I. V. Grigorieva, V. I. Fal'ko, M. Kim, and A. K. Geim, "Giant oscillations in a triangular network of one-dimensional states in marginally twisted graphene," *Nature Communications*, vol. 10, no. 4008, 2019.

[53] C. D. Beule, F. Dominguez, and P. Recher, "Network model and four-terminal transport in minimally twisted bilayer graphene," *Physical Review B*, vol. 104, no. 19, 2021.

[54] A. Ramires and J. L. Lado, "Electrically tunable gauge fields in tiny-angle twisted bilayer graphene," *Physical Review Letters*, vol. 121, no. 14, 2018.

[55] S. Roche, G. T. de Laissardiere, and D. Mayou, "Electronic transport properties of quasicrystals," *Journal of Mathematical Physics*, vol. 38, no. 4, pp. 1794–1822, 1997.

[56] E. Koren and U. Duerig, "Superlubricity in quasicrystalline twisted bilayer graphene," *Physical Review B*, vol. 93, no. 20, 2016.

[57] S. J. Ahn, P. Moon, T.-H. Kim, H.-W. Kim, H.-C. Shin, E. H. Kim, H. W. Cha, S.-J. Kahng, P. Kim, M. Koshino, Y.-W. Son, C.-W. Yang, and J. R. Ahn, "Dirac electrons in a dodecagonal graphene quasicrystal," *Science*, vol. 361, no. 6404, p. 782–786, 2018.

[58] P. Moon, M. Koshino, and Y.-W. Son, "Quasicrystalline electronic states in 30° rotated twisted bilayer graphene," *Physical Review B*, vol. 99, no. 16, 2019.

[59] G. Yu, Z. Wu, Z. Zhan, M. I. Katsnelson, and S. Yuan, "Dodecagonal bilayer graphene quasicrystal and its approximants," *npj Computational Materials*, vol. 5, no. 122, 2019.

[60] A. I. Goldman and R. F. Kelton, "Quasicrystals and crystalline approximants," *Reviews of Modern Physics*, vol. 65, no. 1, pp. 213–230, 1993.

[61] S. Pezzini, V. Miseikis, G. Piccinini, S. Forti, S. Pace, R. Engelke, F. Rossella, K. Watanabe, T. Taniguchi, P. Kim, and C. Coletti, "30°-twisted bilayer graphene quasicrystals from chemical vapor deposition," *Nano Letters*, vol. 20, no. 5, p. 3313–3319, 2020.

[62] L. Banszerus, M. Schmitz, S. Engels, J. Dauber, M. Oellers, F. Haupt, K. Watanabe, T. Taniguchi, B. Beschoten, and C. Stampfer, "Ultrahigh-mobility graphene devices from chemical vapor deposition on reusable copper," *Science Advances*, vol. 1, no. 6, 2015.

[63] Y. Zhang, Y.-W. Tan, H. L. Stormer, and P. Kim, "Experimental observation of the quantum hall effect and berry's phase in graphene," *Nature*, vol. 438, p. 201–204, 2005.

[64] Y. Zhang, Z. Jiang, J. P. Small, M. S. Purewal, Y.-W. Tan, M. Fazlollahi, J. D. Chudow, J. A. Jaszczak, H. L. Stormer, and P. Kim, "Landau-level splitting in graphene in high magnetic fields," *Physical Review Letters*, vol. 96, no. 13, 2006.

[65] L. Huder, A. Artaud, T. L. Quang, G. T. de Laissardiere, A. G. M. Jansen, G. Lapertot, C. Chapelier, , and V. T. Renard, "Electronic spectrum of twisted graphene layers under heterostrain," *Physical Review Letters*, vol. 120, no. 15, 2018.

[66] A. Uri, S. Grover, Y. Cao, J. A. Crosse, K. Bagani, D. Rodan-Legrain, Y. Myasoedov, K. Watanabe, T. Taniguchi, P. Moon, M. Koshino, P. Jarillo-Herrero, and E. Zeldov, "Mapping the twist-angle disorder and landau levels in magic-angle graphene," *Nature*, vol. 581, no. 7806, pp. 47–52, 2020.

[67] C. N. Lau, M. W. Bockrath, K. F. Mak, and F. Zhang, "Reproducibility in the fabrication and physics of moiré materials," *Nature*, vol. 602, p. 41–50, 2022.

[68] N. P. Kazmierczak, M. V. Winkle, C. Ophus, K. C. Bustillo, S. Carr, H. G. Brown, J. Ciston, T. Taniguchi, K. Watanabe, and D. K. Bediako, "Strain fields in twisted bilayer graphene," *Nature Materials*, vol. 20, p. 956–963, 2021.

[69] S. Carr, *Moire patterns in 2D materials*. PhD thesis, Harvard University, 2020.

[70] S. Turkel, J. Swann, Z. Zhu, M. Christos, K. Watanabe, T. Taniguchi, S. Sachdev, M. S. Scheurer, E. Kaxiras, C. R. Dean, and A. N. Pasupathy, "Orderly disorder in magic-angle twisted trilayer graphene," *Science*, vol. 376, no. 6589, p. 193–199, 2022.

[71] P. M. Chaikin and T. C. Lubensky, *Principles of condensed matter physics*. Cambridge: Cambridge University Press, 1995.

[72] N. D. Mermin, "The topological theory of defects in ordered media," *Reviews of Modern Physics*, vol. 51, no. 3, pp. 591–648, 1979.

[73] D. Halbertal, S. Shabani, A. N. Passupathy, , and D. N. Basov, "Extracting the strain matrix and twist angle from the moiré superlattice in van der waals heterostructures," *ACS Nano*, vol. 16, no. 1, p. 1471–1476, 2022.

[74] F. Guinea, M. I. Katsnelson, and A. K. Geim, "Energy gaps and a zero-field quantum hall effect in graphene by strain engineering," *Nature Physics*, vol. 6, p. 30–33, 2010.

[75] Y. Zhang, Y. Kim, M. J. Gilbert, and N. Mason, "Magnetotransport in a strain superlattice of graphene," *Applied Physics Letters*, vol. 115, no. 143508, 2019.

[76] K. Yasuda, X. Wang, K. Watanabe, T. Taniguchi, and P. Jarillo-Herrero, "Stacking-engineered ferroelectricity in bilayer boron nitride," *Science*, vol. 372, no. 6549, pp. 1458–1462, 2021.

[77] C. R. Woods, P. Ares, H. Nevison-Andrews, M. J. Holwill, R. Fabregas, F. Guinea, A. K. Geim, K. S. Novoselov, N. R. Walet, and L. Fumagalli, "Charge-polarized interfacial superlattices in marginally twisted hexagonal boron nitride," *Nature Communications*, vol. 12, no. 347, 2021.

[78] X. Wang, K. Yasuda, Y. Zhang, S. Liu, K. Watanabe, T. Taniguchi, J. H. ad Liang Fu, and P. Jarillo-Herrero, "Interfacial ferroelectricity in rhombohedral stacked bilayer transition metal dichalcogenides," *Nature Nanotechnology*, vol. 17, 2022.

[79] M. V. Stern, Y. Waschitz, W. Cao, I.Nevo, K. Watanabe, T. Taniguchi, E. Sela, M. Urbakh, O. Hod, and M. B. Shalom, "Interfacial ferroelectricity by van der waals sliding," *Science*, vol. 372, no. 6549, pp. 1462–1466, 2021.

[80] A. Weston, E. G. Castanon, V. Enaldiev, F. Ferreira, S. Bhattacharjee, S. Xu, H. Corte-León, Z. Wu, N. Clark, A. Summerfield, T. Hashimoto, Y. Gao, W. Wang, M. Hamer, H. Read, L. Fumagalli, A. V. Kretinin, S. J. Haigh, O. Kazakova, A. K. Geim, V. I. Fal'ko, and R. Gorbachev, "Interfacial ferroelectricity in marginally twisted 2D semiconductors," *Nature Nanotechnology*, 2022.

[81] V. V. Bulatov, L. L. Hsiung, M. Tang, A. Arsenlis, M. C. Bartelt, W. Cai, J. N. Florando, M. Hiratani, M. Rhee, G. Hommes, T. G. Pierce, and T. D. de la Rubia, "Dislocation multijunctions and strain hardening," *Nature*, vol. 440, p. 1174–1178, 2006.

[82] J. P. Hirth and J. Lothe, *Theory of dislocations*. New York: Wiley, 1982.

[83] C. Kittel, "Theory of antiferroelectric crystals," *Physical Review*, vol. 82, no. 5, pp. 729–732, 1951.

[84] C. A. Randall, Z. Fan, I. Reaney, L.-Q. Chen, and S. Trolier-McKinstry, "Antiferroelectrics: History, fundamentals, crystal chemistry, crystal structures, size effects, and applications," *Journal of the American Ceramic Society*, vol. 104, no. 8, p. 3775–3810, 2021.

[85] Z. Zhu, P. Cazeaux, M. Luskin, and E. Kaxiras, "Modeling mechanical relaxation in incommensurate trilayer van der waals heterostructures," *Physical Review B*, vol. 101, no. 22, 2020.

[86] X. Zhang, K.-T. Tsai, Z. Zhu, W. Ren, Y. Luo, S. Carr, M. Luskin, E. Kaxiras, and K. Wang, "Correlated insulating states and transport signature of superconductivity in twisted trilayer graphene superlattices," *Physical Review Letters*, vol. 127, no. 16, 2021.

[87] G. E. Bacon, "A note on the rhombohedral modification of graphite," *Acta Crystallographica*, vol. 3, no. 320, p. 320, 1950.

[88] C. H. Lui, Z. Li, Z. Chen, P. V. Klimov, L. E. Brus, and T. F. Heinz, "Imaging stacking order in few-layer graphene," *Nano Letters*, vol. 11, no. 1, p. 164–169, 2011.

[89] E. Khalaf, A. J. Kruchkov, G. Tarnopolsky, and A. Vishwanath, "Magic angle hierarchy in twisted graphene multilayers," *Rhysical Review B*, vol. 100, no. 8, 2019.

[90] Z. Hao, A. M. Zimmerman, P. Ledwith, E. Khalaf, D. H. Najafabadi, K. Watanabe, T. Taniguchi, A. Vishwanath, and P. Kim, "Electric field–tunable superconductivity in alternating-twist magic-angle trilayer graphene," *Science*, vol. 371, no. 6534, pp. 1133–1138, 2021.

[91] J. M. Park, Y. Cao, K. Watanabe, T. Taniguchi, and P. Jarillo-Herrero, "Tunable strongly coupled superconductivity in magic-angle twisted trilayer graphene," *Nature*, vol. 590, p. 249–255, 2021.

[92] J. M. Park, Y. Cao, L. Xia, S. Sun, K. Watanabe, T. Taniguchi, and P. Jarillo-Herrero, "Magic-angle multilayer graphene: A robust family of moiré superconductors," *preprint*, 2021.

[93] A. K. Geim and I. V. Grigorieva, "Van der waals heterostructures," *Nature*, vol. 499, p. 419–425, 2013.

[94] A. U. Alam, M. M. R. Howlader, and M. J. Deen, "The effects of oxygen plasma and humidity on surface roughness, water contact angle and hardness of silicon, silicon dioxide and glass," *Journal of Micromechical Microengineering*, vol. 24, 2014.

[95] "Radiation damage in the TEM and SEM," *Micron*, vol. 35, no. 6, pp. 399–409, 2004.

[96] P. Mazur and S. R. de Groot, "On onsager's relations in a magnetic field," *Physica*, vol. 19, pp. 961–970, 1953.

[97] D. E. Cohen, *Combinatorial Group Theory: A Topological Approach (London Mathematical Society Student Texts, Series Number 14).* Cambridge University Press, 1989.

[98] O. Kharlampovich and A. Myasnikov, "Elementary theory of free non-abelian groups," *Journal of Algebra*, vol. 302, no. 2, pp. 451–552, 2006.

This thesis was typeset using LaTeX, originally developed by Leslie Lamport and based on Donald Knuth's TeX. The body text is set in 11 point Egenolff-Berner Garamond, a revival of Claude Garamont's humanist typeface. A template that can be used to format a PhD thesis with this look and feel has been released under the permissive MIT (X11) license, and can be found online at github.com/suchow/Dissertate or from its author, Jordan Suchow, at suchow@post.harvard.edu.